An Efficient Model for Predicting the Effect of Crack Coalescence on Dynamic Brittle Failure of Armor Ceramics

by

Farah Huq

A dissertation submitted to The Johns Hopkins University in conformity with the requirements for the degree of Doctor of Philosophy.

Baltimore, Maryland

March, 2017

Abstract

The failure of brittle ceramics under an impact event is a highly complex phenomenon. The catastrophic failure of the material under dynamic loading is attributed to its inherent microstructural features which initiate different failure mechanisms. To improve the ballistic performance of the armor ceramic, it is necessary to predict the behavior of the material under complex dynamic loading conditions. A physics-based constitutive description of the material that incorporates sub-scale information such as the key failure mechanisms, their interaction and their role in the failure process is required to predict the overall dynamic behavior of the armor ceramic. This dissertation work aims at developing some essential components of a mechanism-based constitutive modeling framework, specifically optimal selection of the representative flaw statistics that serve as input to the relevant simulations, a micromechanics model for crack coalescence, and the interaction of crack coalescence with other sub-scale mechanisms initiating at different stages of loading.

The processing induced microstructural flaws in the ceramic armor serve as the secondary microcrack initiation sites in the material. The mechanical response of

ABSTRACT

the material is highly dependent on the size and orientation of the preexisting flaws or defects. It is very important to define the initial flaw population to capture the realistic point-to-point variability in the material domain. To predict the dynamic behavior, computational simulations of the boundary-value problems are performed where the constitutive response is characterized by the sub-grid-scale flaw population. Each individual finite element or similar subdomain defined in the simulation encloses individual flaw population to represent the inherent heterogeneity in the material. The flaw population within each element has thousands of flaws. The secondary microcracks appear from the tip of those flaws. Tracking the growth and evolution of the microcracks at each load step is computationally very expensive. A novel numerical binning scheme has been developed to reduce this computational burden. The technique aims at dividing the large flaw population into smaller number of groups or bins with a representative flaw characteristic(s) for each bin. The initial flaw data (e.g. size and orientation for a two-dimensional (2D) problem is mapped on the nodes of a reference grid in the probability space. The nodal value containing lumped initial flaw data is used to calculate the fraction of flaws associated with each Gauss point located on the grid of the probability space. The location of the Gauss points serves as the representative flaw characteristic(s) for the bin. Different grid morphologies can be adopted to capture a particular range of variables significant for the simulation. The irregular or zoomed grid morphology is obtained by developing a zooming function based on the criterion (for brittle damage models) that each bin

on an average contributes equally to the global damage due to the secondary crack formation. To check the efficiency and accuracy of the scheme it is initially applied in the context of a simple 2D micromechanics model. The stress-strain response predicted by the binned solution matches the exact solution (evaluating constitutive response for each individual flaw) with an error level of less than 1% when zoomed grid morphology is adopted. The increases the computational efficiency by two orders of magnitude. The binning technique is further incorporated in a three-dimensional (3D) constitutive model (Tonge-Ramesh Model). The binned solution for the constitutive response shows an error level less than 1% with an order of magnitude increase in computational efficiency.

Initiation, propagation and coalescence of secondary microcracks (wing-cracks) from the preexisting defects is identified as the key mechanism for fracture of the specimen under dynamic compression. Significant coalescence of cracks occurs after the material reaches its peak strength. The dynamically propagating wing-cracks emanated from the tip of the preexisting defects merge with each other creating a number of coalesced cracks in the medium. A micromechanics-based model has been developed to capture the effect of explicit crack coalescence on the dynamic strength of the material. This model incorporates different geometry of coalesced cracks into the medium. The coalesced and non-coalesced crack families are treated as inclusions in a medium with effective properties. The growth of every crack is influenced by the presence of other cracks through this effective medium approach. The fraction

of cracks that merge with each other is estimated by calculating the probability of failure using Poisson process statistics. The crack population is updated at each load step. The explicit coalescence model predicts a significantly lower peak strength than the original model without coalescence.

The micromechanics-based damage model to capture the propagation and coalescence of microcracks is integrated into a physics-based constitutive model (Tonge-Ramesh model) for armor ceramic which includes thermodynamic response through an equation of state, damage kinetics via interaction and growth of microcracks and a granular plasticity model for a highly damaged material. The implementation of explicit crack coalescence in the 3D constitutive model for large deformation for a single material point shows significant reduction in peak stress when subjected to dynamic uniaxial compression. In addition, the transition to granular flow state from microcracking happens faster due to higher damage evolution for crack coalescence mechanism. The mechanism based model serves as the constitutive model for a macro-scale large deformation problem, in the context of the Uintah material point method. In order to capture the realistic point-to-point variability in micromorphology, a distinct flaw population is assigned to each material point. The key goal of the work is to identify under which loading condition crack coalescence mechanism play a major role in reducing the peak strength of the real ceramic armor plate.

Primary Reader: Lori Graham-Brady

Secondary Reader: James Guest, Andrew Tonge

ABSTRACT

Acknowledgments

I would like to extend my sincere thanks and gratitude to my advisor Professor Lori Graham-Brady who gave me an opportunity to pursue my interest and continue my education. I have learnt critical thinking and developed problem solving ability under her patient guidance throughout the course of my Ph.D. research work in the Department of Civil Engineering at Johns Hopkins University. She taught me to think about a complex problem from a mathematical perspective to provide an alternative easy solution which is not always achievable following the traditional approach. This will help me to think about a wide range problem in a different way and provide a useful solution for them.

My Ph.D. research focus was modeling dynamic brittle fracture for armor ceramic materials which is a very broad topic with lots of different modeling issues to handle. I have attempted to address couple of modeling issues related to dynamic brittle fracture problem which involved significant mathematical and physics-based modeling. In addition, the nature of the problems demanded good computational skill. The different challenging aspects of the problems were very interesting and useful for

developing a unique problem solving ability. I would like to thank Hopkins Extreme Materials Institute and U.S. Army Research Laboratory for giving me an opportunity to work on the modeling tasks of the Ceramic CMRG. Their regular feedback on the modeling tasks and also the educational activities were very valuable.

I would like to thank Professor K. T. Ramesh and his group for their continual support in my work. I have learnt a lot from the discussions in the Ceramic CMRG group meetings and the presentations that were done on a regular basis. I would like to thank them for sharing the computational resources and codes with me which made my work lot much easier.

I would like to thank Professor Rebecca Brannon from University of Utah for her involvement in my Ph.D. work. She was at Hopkins for a short period of time during Spring 2014. I really enjoyed working with her. I have developed a novel numerical technique to sample optimal random input with her and my advisor which I published in International Journal of Numerical Methods in Engineering. I highly appreciate the guidance and teaching I received from her.

The last part of my Ph.D. work was integrating the models that I have developed into a mechanism-based constitutive model to capture different mechanisms occurring during an impact event. The novel modeling framework was originally developed by Dr. Andrew L. Tonge, a former Ph.D. student at Professor Ramesh's group currently working with Army Research Laboratory. The model was complex with activation and interaction of different mechanisms at different length and time scales with an

additional computational difficulty. Without the guidance and regular involvement from Dr. Andrew Tonge, this integration work would not be possible within a time limit. I would like to thank him deeply for his time and contribution in the work.

I would like to thank my all of my group mates for their support and regular feedback on my work. I will surely miss our weekly group meetings. I would specially thank my past group mate Junwei Liu for his support during my Ph.D. work and later on. I would like to thank all of my friends in the Department of Civil Engineering with whom I shared my journey here and who made my stay at Hopkins really enjoyable. The Hopkins Extreme Materials Institute staff members and our department staff members have always been incredibly helpful to me. I would like to thank them all.

I would like to thank Professor Lori Graham-Brady, Professor James Guest and Dr. Andrew L. Tonge for taking the time to read this document and provide the feedback on that.

This work would be impossible without the funding support I received from different funding agencies over the years. My first year funding was provided by the Department of Civil Engineering. In addition, I received a fellowship provided by Mr. Carl E. Heath which covered my stipend. I would like to express my heartfelt thanks and gratitude to Mr. Heath for supporting my education when I was in very much need. His enthusiasm for supporting Women's education was really inspirational for me. I was funded my NSF and IGERT to continue my education. The final years of my Ph.D. work was supported by the Army Research Laboratory under

ACKNOWLEDGMENTS

the Corporate Agreement Number Cooperative W911NF-12-2-0022 Agreement. The views and conclusions contained in this documents are my own and should not be interpreted as representing the official policies, either expressed or implied, of the Army Research Laboratory or the US Government. The US government is authorized to reproduce and distribute reprints for government purposes notwithstanding any copyright notation herein.

Finally, I would like to thank my family for their unconditional love and support for me always.

Dedication

To my family and friends for their unconditional love and support.

Contents

x

List of Tables

List of Figures

Chapter 1

Introduction

Brittle materials like rock, concrete, glass, and ceramics. are subjected to dynamic loading in a number of applications. Planetary impact, armor applications, and blast loading on structures are some relevant examples for brittle materials undergoing extreme dynamic loading. During these extreme dynamic events, a large amount of energy is deposited in a very short time. The speed of energy propagation in the material from the point of deposition is finite, leading to a rapid rise in local energy density. The material dissipates this excessive energy through various internal pathways, or mechanisms (e.g. fracture, melting, and vaporization). The type of mechanisms activated are dependent on both the material type and the nature of the loading as reflected through the local stress state. The most common failure mechanism in brittle materials is microcracking from preexisting defects (e.g., pores or inclusions) [6].

CHAPTER 1. INTRODUCTION

Pre-existing microstructural defects in brittle materials can include weak grain boundaries, triple junctions, second phases (sintering aids), inclusions, pores, pre-existing microcracks among others. The defects or flaws (here flaws and defects are used interchangeably) serve as the stress concentration sites. Different ceramics have different processing induced defect populations, which are characterized using electron microscopy. A detailed study on hot pressed boron carbide (B4C) by Hogan et. al. [7] shows the presence of three types of processing-induced inhomogeneities: aluminum nitride inclusions, small graphite particles and pores, and larger graphitic disks. Scanning electron microscopy of the fracture surface confirms the graphitic disks as likely fracture initiation sites. Two distinct types of defects have been identified in silicon carbide (SiC) in a study done by Bakas et. al. [8]. The first category of defects are carbonaceous inclusions (resulting from carbon impurities in sintering aids). The second category of defect is aluminium-iron-oxide phase. The large inclusion were found on the fracture surface suggesting crack formation. Several defects at different length scales are also found in sintered aluminum nitride (AlN) [9]. The sintering agent yttrium oxide is present between the grains resulting in a weaker grain boundary strength. At a slightly larger scale, irregularly shaped pores were observed. Flake-like carbon rich inclusions were found at even larger length scale. All of these flaws are found on the fracture surfaces, suggesting their major role in secondary crack nucleation and growth.

Uniaxial dynamic compression tests suggest that axial splitting is the primary

mode of failure in ceramics under uniaxial compression [3]. Axial splitting in the material is attributed to the opening of microcracks or wing cracks from the preexisting flaw surfaces. The growth and coalescence of wing cracks in the direction of maximum principal compression produce axial splitting. This failure mode is reported by many researchers in the past [10], [11], [12], [13] specifically for brittle materials like rock or ice under quasi-static loading. Under quasi-static loading, the largest flaw in the specimen causes failure, as predicted by the weakest link theory. However, multiple flaws influence the dynamic behavior brittle ceramics, making dynamic failure more complex than the Weibull-type approaches. Wing cracks from a wide range of flaws initiate, propagate and coalesce.

To predict the dynamic behavior of brittle materials under compression, various models have been developed to capture different aspects of microcracking (e.g. nucleation, propagation, interaction and coalescence). Most of the models relate axial splitting of the materials to the nucleation and growth of wing-cracks [14], [15], [16]. In particular, interaction plays a significant role in facilitating crack growth. Horii and Nemat-Nasser [17] developed the method of pseudo traction to capture the elastic fields of a periodic array interacting cracks. Kachanov [18] described a simple self-consistent approach to predict the elastic stress fields for periodic and arbitrary arrays of cracks. Kachanov's method is modified by Batista and Gross [19] to predict the effective stress intensity factors for interacting wing cracks. Some numerical approaches for capturing the effect of interacting microcracks are proposed by [20], [21].

All of these works capture the effect of arbitrary shape (wing cracks in some cases) crack interaction on the elastic stress fields of the material.

Nemat-Nasser & Deng [22] extended the wing crack model under quasi-static loading to the dynamic loading range. An effective dynamic stress intensity factor is calculated from the interaction of array of wing cracks subjected to far-field compression. The effect of strain rate is predicted by the dependence of dynamic stress intensity factor on the crack growth speed. Many researchers proposed models for the interacting and non-interacting microcrack growth under dynamic loading using a micromechanics-based approach [23], [24], [25], [26]. This class of model defines the growth of the microcracks by an effective crack driving force and a crack growth law. The instantaneous effective stiffness of the medium is obtained from the damage related to microcrack growth [27], [23], [28], [29], [30]. The nucleation, propagation (estimated by the crack growth law) and interaction (used to predict an effective stress field at the crack tip) are captured in the models using different approaches. However, microcrack coalescence is not captured by these models under dynamic loading.

A direct observation of micro-crack coalescence under dynamic compression is reported by [3]. The crack coalescence is observed in rock-like materials under quasi-static compression [31], [32], [2], [33]. The nature of coalescence based on the different properties (e.g. length, orientation, nearest neighbor distance etc.) of the pre-existing defects is observed in these experiments. Coalescence is occurring through the wing cracks associated with the closely spaced flaws. Coalescence through shear cracks

are also observed in these experiments. Numerical models [34], [35] have been developed to predict the nature of coalescence in a small number of pre-existing defects. However, capturing crack coalescence under dynamic compression is much more challenging as dynamic loading involves the activation of a large number of flaws. Under dynamic compression, coalescence occurs between numerous pairs of wing cracks resulting in formation of a large damage zone [3], which accelerates axial splitting [3].

The constitutive models for simple dynamic compression aim to capture the microcracking as the sole physical mechanism. However, multiple other mechanisms are activated in the material under an impact due to the heterogeneous stress state, including shock formation, microcracking, flow of disordered media, and pore collapse [6]. These mechanisms are modeled by physical laws at different length and time scales. The shock response is captured by an equation of state. Dynamic fracture models are used to capture the initiation, propagation and coalescence of microcracks. Granular plasticity represents the behavior of the disordered medium at a highly damaged state. The physics-based generalized constitutive model predicts the response of the material under complex loading scenarios.

This dissertation addresses three important modeling problems associated with the overall modeling approach of dynamic failure of armor ceramics. The first part of the work includes a numerical model to efficiently represent the input flaw population with minimal number of bins that represent heterogeneous microstructure. The second part of the work addresses a micromechanics-based model to capture micro-

crack coalescence under uniaxial compression. Finally, an efficient approach for the coalescence model is developed to improve the computational efficiency. The efficient crack coalescence model is implemented into the mechanism-based Tonge-Ramesh (TR) [36] constitutive model (a brief description is provided in later a section), which captures multiple mechanisms that occur under high velocity impact.

1.1 Selection of Input Flaw Statistics

The relationship between ballistic performance of armor ceramics and the processing induced anomalous defects has been studied by many researchers [7], [37], [38]. It is also reported in the theoretical and experimental studies that the materials exhibit considerable variability in performance [38], [9]. One reasonable explanation for this variability can be the presence of a widely scattered underlying defect population. To predict the dynamic strength accurately, it is important to capture this defect population. Capturing the random microstructure amounts to defining a local distinct defect population for each material point or integration point. However, there are several issues related to the selection of input parameters required to capture the realistic heterogeneous microstructure.

The natural choice for these input flaw populations are statistical samplings from their parent distributions. The important attributes (e.g. size, orientation etc.) of the defect population are determined based on their role in nucleation and growth of

the microcracks. Flaw sizes and orientations are two key parameters for wing cracks nucleation. The flaw size distribution and the average number of flaws per unit area (flaw density in other words) are obtained from characterization experiments (e.g. TEM) and they are considered as material parameters. Assuming a separation of scales, the flaw sizes sampled from the parent distribution are all at the element subscale (sizes much smaller that the computational mesh size). However, tracking a large number of cracks nucleated from those flaws for each integration point is computationally very expensive. To circumvent this problem, a statistical numerical method has been developed to aid the optimal selection of representative flaw statistics.

The numerical technique divides the initial flaw population sampled from the parent distribution into a smaller number of groups or bins. Each bin has a representative flaw with a given attribute (e.g. size or orientation) and a weight which represents the fraction of flaws associated with that bin. The binning scheme uses a grid laid down in probability space (range is $0-1$ in each direction of the space). Each direction of the probability space represents an attribute of the flaw. Each direction of the probability space is assigned to a particular flaw attribute which are represented by random numbers between $0-1$. The grid laid down in the probability space has uniform or non-uniform divisions. Each division is referred as cells. Each cells contains Gauss points which serve as bin location or the representative flaw attribute. Traditional finite element shape functions are used for lumping a certain number of flaws into the nodes of the probability space. The number of flaws associated with each bin

is obtained from the nodal weight using traditional Gauss quadrature. The binned flaw population is then used as the input for the simulations. The accuracy of the method is verified by using the binned solution in a simple 2D micromechanics model. The stress-strain response matches the exact solution (where every crack is tracked at each load step) accurately when zoomed grid morphology is used. The error level associated with binned solution is less than 0.1% while increasing the computational accuracy by two orders of magnitude. This method can capture the upper bins of the distribution pretty accurately for both bounded and unbounded distributions. The desired level of accuracy can be obtained by varying the grid morphologies using relevant mechanistic criterion. This method is in general well suited to a wide range of problems where function evaluations needs to be reduced by replacing the large set of random input parameters with a smaller set of parameters [39].

The binning scheme is applied for a 3D material constitutive model (TR model) that includes multiple mechanisms occurring during an impact event [36]. The constitutive model only includes initial flaw size and local density as microstructural variables. The binning scheme is applied to an initial flaw population for a representative volume. The scheme reduces the population by an order of magnitude. The random microstructure is thus characterized by the reduced flaw statistics defined by flaw sizes and local flaw density assigned to each material point or integration point residing at the macroscale mesh for solution of the boundary value problem of interest

1.2 Modeling Micro-crack Coalescence for Dynamic Brittle Failure

The basic methodology of the crack coalescence model proposed here is introducing coalesced cracks in the medium once the wing cracks growing from the flaws begin to intersect randomly. The patterns of coalesced cracks used in the work are obtained from the experimental observation for rock-like materials for a pair of cracks [2] (see chapter 3 for details). Figure 1.1 gives a basic scheme for coalesced cracks introduced

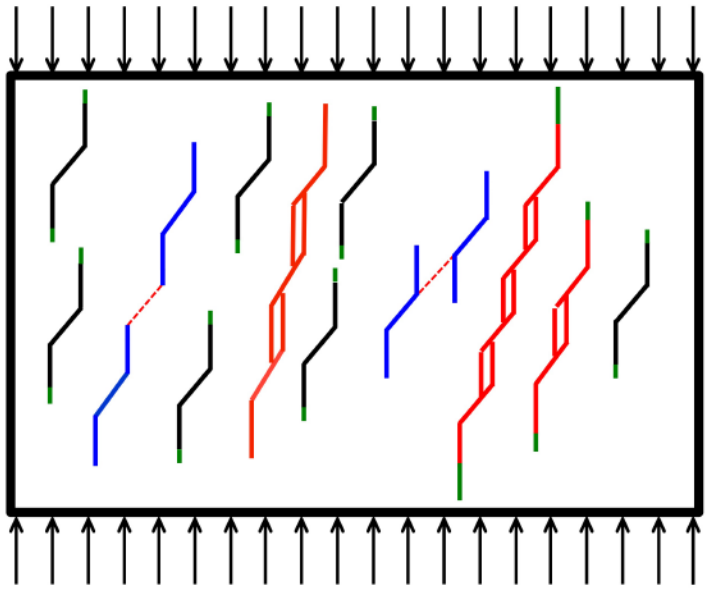

Figure 1.1: Schematic showing the basic idea of crack coalescence model. The medium has single (non-coalesced) and coalesced cracks at a given load step. There are two basic pattern of coalesced cracks. The larger cracks (shown in red) coalesce through wing cracks. The other pattern of coalesced cracks (shown in blue) coalese through a secondary shear crack (shown in dotted red line). The shear crack might form between wing crack tips or between the flaw surfaces. The green line represents crack growth increment. The patterns are consistent with [2].

at each load step.

1.2.1 Wing-Crack Model

The detailed analysis of the wing crack model was initially done in [40] and [16], which relates wing cracking to axial splitting of the material. The mechanism for the crack opening is the relative sliding of the faces of the flaw surface. The residual force available after overcoming the frictional resistance at the flaw surface acts as the crack opening force. Figure 1.2 shows the basic wing crack model. The crack driving for F for the coalesced cracks are calculated based on the self-consistent approach proposed in the Paliwal-Ramesh (PR) model [23].

1.2.2 Overview of the Paliwal-Ramesh Model

The Paliwal-Ramesh model (PR) [23] proposed an effective medium approach to estimate the dynamic strength of the material for interacting dynamically propagating microcracks. The concept of this effective medium approach follows the early work of Budiansky and O'connell [27]. An elliptic inclusion surrounding the wing-crack is placed in a medium with effective damaged properties. The material inside the inclusion is assumed to be undamaged. The local stress field inside the elliptic inclusion is estimated by solving the boundary value problem [41], [42] of an infinite medium with an inclusion under far-field principal stresses (see [43]). Each crack enclosed by the elliptic region experiences the presence of other cracks through the effective medium, in which the inclusion is placed. The effective medium approach is

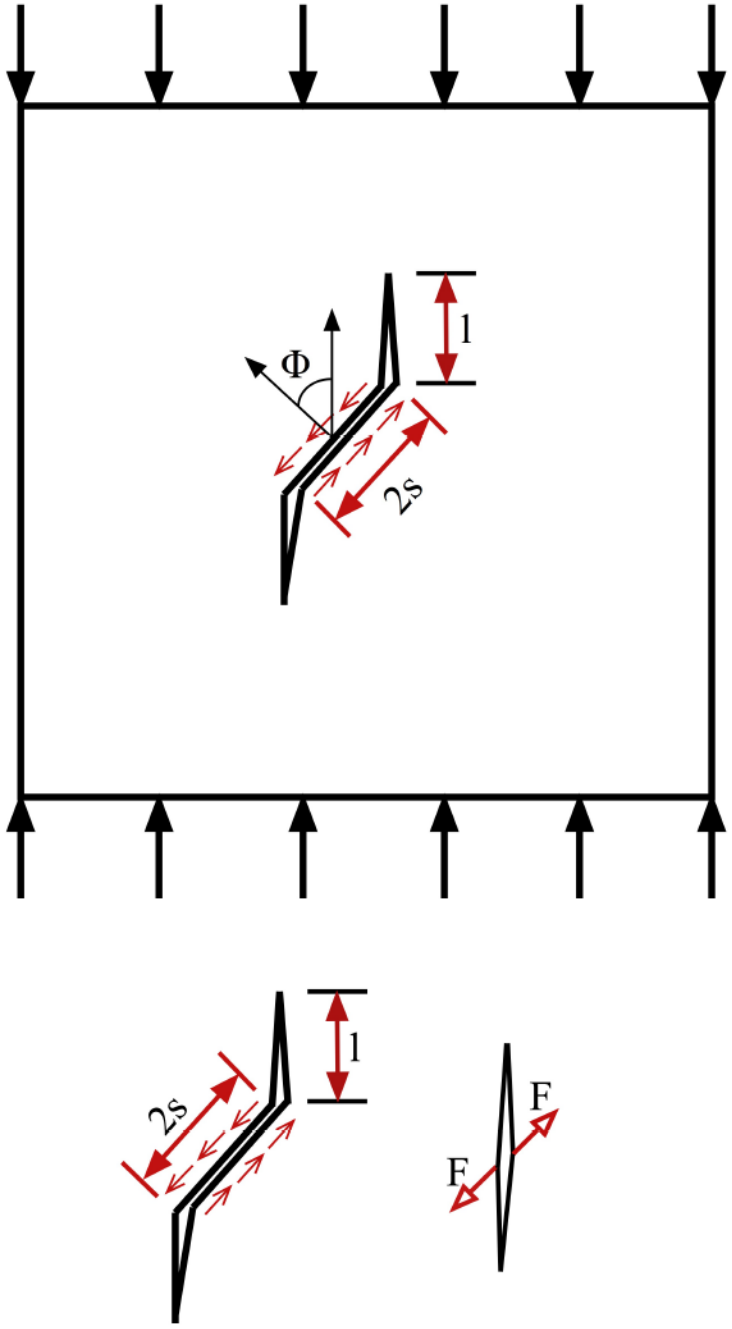

Figure 1.2: The figure is showing the opening of wing crack from flaw surface in a medium subjected to far-field uniaxial compression. The flaw is at an angle ϕ from the loading direction. The second row shows an idealized representation of the wing crack by a straight crack subjected to a pair of splitting force.

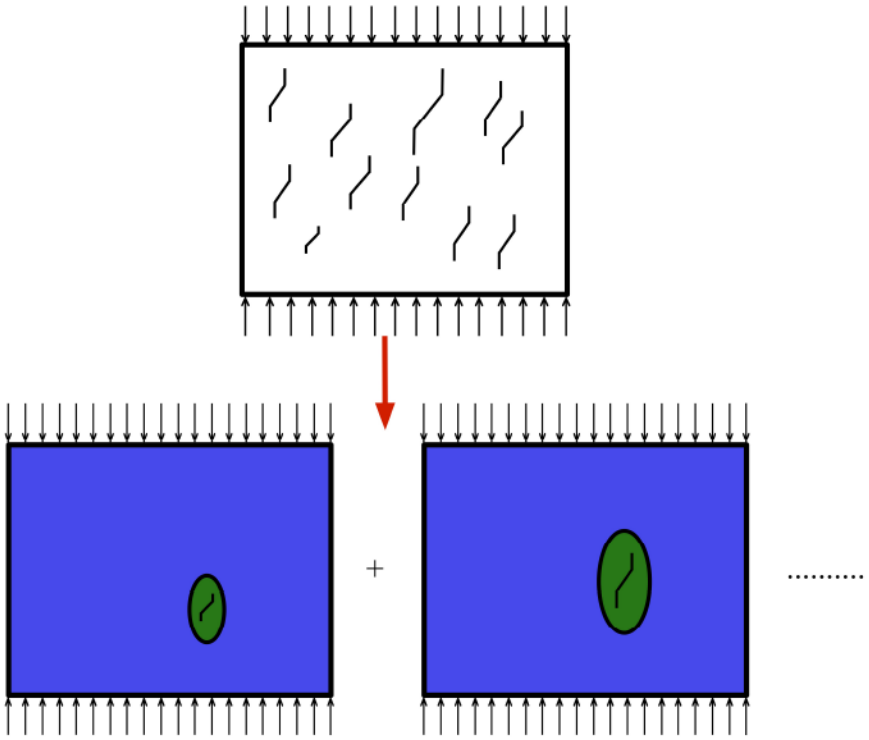

Figure 1.3: Illustration of effective medium approach proposed in PR model. Each elliptical inclusion with a distinct crack is placed in the effective medium. The property of the medium is updated by the scalar (described later in this section) damage parameter for all the cracks.

outlined by a schematic diagram in figure 1.3. A brief overview of relevant equations in the PR model is given here.

The local stress field inside the elliptic inclusion is:

$$\sigma^e = \begin{bmatrix} \sigma^e_{11} \\ \sigma_{22} \\ \sigma_{12} \end{bmatrix} \tag{1.1}$$

leading to the effective resolved shear stress on the flaw surface [23]:

$$\tau = \tau_c - \mu(\sigma^e_{11}\cos^2\phi + \sigma^e_{22}\sin^2\phi + \sigma_{12}\sin 2\phi) + \frac{1}{2}[(\sigma^e_{11} - \sigma^e_{22})\sin 2\phi - \sigma^e_{12}\cos 2\phi] \quad (1.2)$$

The shear stress τ multiplied by the flaw length $2s$ is the splitting force F acting on the center of the idealized straight crack shown in figure 1.2. The mode-I stress intensity factor for a crack subjected to a pair of splitting force [15] is:

$$K_{\mathrm{I}} = \frac{2s\tau\cos\phi}{\sqrt{\pi(l + 0.27s)}} + \sigma_{22}\sqrt{\pi l} \quad (1.3)$$

The mode-I static stress intensity factor is related to mode-I dynamic stress intensity factor $K_I^{(d)}$. Freund [44] proposed an expression for mode-I dynamic stress intensity factor in terms of the instantaneous crack speed $\dot{l}(t)$ of a growing crack and its static mode-I stress intensity factor $K_{\mathrm{I}}(l)$.

$$K_I{}^{(d)}(l, \dot{l}) = k(\dot{l})K_I(l) \quad (1.4)$$

$k(\dot{l})$ is a universal function for crack speed. Nemat-Nasser and Deng [22] obtained an expression for $k(\dot{l})$.

$$k(\dot{l}) = \left(1 - \frac{\dot{l}}{C_R}\right)\left(1 - \frac{\dot{l}}{2C_R}\right)^{-1} \quad (1.5)$$

where C_R is the Rayleigh wave speed. Following the experimental observation [45] that the mode-I dynamic fracture toughness $K_{Ic}^{(d)}$ is higher than static mode-I fracture

(K_{Ic}) toughness, the crack growth law proposed in PR model is:

$$\dot{l} = \frac{C_R}{\alpha}\left(\frac{K_I - K_{Ic}}{K_I - 0.5K_{Ic}}\right)^{\gamma} \tag{1.6}$$

where α and γ are fitting parameters to match the experimental data. The fitting parameter γ characterizes the toughness-velocity relations (for details see [23]).

The crack growth increment at each load step is obtained from equation (1.6). The macroscopic properties (e.g. elastic constants) are updated due to the microcrack growth to capture the softening of the material. This is done by means of a scalar damage variable in PR model. The damage models proposed by many researchers in the past [27], [46], [22], [26], [47], [48] incorporate the microstructural variables into internal state variables like damage. Damage is a measure of the characteristics (e.g. length, orientation, density etc.) of the crack population in a representative volume element (RVE). The scalar crack density parameter or damage Ω for a 2D solid can be defined as [23]:

$$\Omega = \frac{1}{A}\sum_{i=1}^{N_{\text{cracks}}} l_i^2 \tag{1.7}$$

For N_{cracks} in the 2D domain with an area A can be defined as:

$$\Omega = \sum_{i=1}^{N_{\text{cracks}}} \eta_i l_i^2 \tag{1.8}$$

In equation (1.8), η_i is the number density of each crack family.

The effect of the microstructural variables (e.g. crack length here) is upscaled into effective moduli of the damaged material through the relationship between damage and elastic constants developed by Budiansky and O'connell [27]:

$$\frac{\bar{E}}{E} = 1 - \frac{\pi^2}{30}(1+\bar{\nu})(5-4\bar{\nu})\Omega \tag{1.9a}$$

$$\frac{\bar{G}}{G} = 1 - \frac{\pi^2}{60}(10-7\bar{\nu})\Omega \tag{1.9b}$$

$\bar{E}$ and $\bar{G}$ are the Young's modulus and shear modulus of the damaged medium. The Poisson's ratio $\bar{\nu}$ is considered same as the Poisson's ratio of the undamaged medium. The material behavior is anisotropic due to preferential direction of wing cracking. A simplified assumption is used to represent this damage induced anisotropy. The damage in the axial direction is considered a fraction of damage in the transverse direction. For the case of uniaxial dynamic loading the stress rate is expressed as [23]:

$$\dot{\sigma} = E\left(1 - \frac{\pi^2}{30}(1+\bar{\nu})(5-4\bar{\nu})\Omega\right)\dot{\epsilon} - E\frac{\pi^2}{30}(1+\bar{\nu})(5-4\bar{\nu})\dot{\Omega}\epsilon \tag{1.10}$$

The step-by-step methodology of PR model can be summarized as:

- Use the global stress at the previous load step to calculate the local stress at the current load step using the effective medium approach in [23]
- Calculate the crack growth rate for all the crack families using equation (1.6)
- Update the crack length for each crack family as $l(t_{i+1}) = l(t_i) + \dot{l}\Delta t$

- Calculate the global damage Ω using equation (1.8)
- Update the stress rate using equation (1.10) and update the global stress
- Return to the first step unless $\Omega \geq \Omega_{max}$. The maximum damage level Ω_{max} in PR model [23] is assumed equal to 0.5.

1.3 Implementation of Crack Coalescence in PR Model

The crack coalescence model adopts a similar self-consistent approach as the PR model for the coalesced cracks. The coalesced cracks are treated as inclusions and placed in the effective medium with updated properties due to the presence of single and coalesced cracks. The crack growth rate for the coalesced cracks are estimated from the mode-I stress intensity factors, which is based on the effective local stress field. The damage due to the single and coalesced cracks is used to update to overall properties of the medium using equation (1.10).

Since the microscale cracks are not explicitly modeled, information on their spatial location is incorporated in an average sense through the average flaw density. The spatial location of the flaws is independent of each other and also assumed to occur randomly in space. To estimate the fraction of cracks that coalesce at each load step, the probability of a crack in a given region is calculated. The crack population

is updated at each load step based on this probability of coalescence. The crack coalescence model shows a significant reduction in peak stress when compared to the peak stress predicted by the PR model.

1.4 Efficient Approach for Crack Coalescence Model

The proposed crack coalescence model summarized in the previous section tracks a huge number of crack families. The number of crack families increases at each load step due to addition of new coalesced crack families. Therefore, the computational burden associated with the crack coalescence model can be significant. To address this issue, an alternative approach for crack coalescence model is proposed. In this approach, all the crack families within a particular pattern of coalescence are replaced by an equivalent crack. The properties of the equivalent crack (e.g. crack length, distance between the pair of splitting forces etc.) contains information about all of the crack families replaced by the equivalent crack. The equivalent crack approach tracks the stress-strain response predicted by the original crack coalescence model with small error, using significantly less computational time and mainly fewer state variables that require space in memory. In addition, the equivalent crack approach is very suitable for multi-scale simulations of brittle materials with an underlying computationally demanding mechanism-based constitutive model. To demonstrate this,

the equivalent crack approach is implemented in the Tonge-Ramesh (TR) mechanism-based constitutive model [36]. A brief description of the TR model is given in the next section.

1.4.1 Tonge-Ramesh Constitutive Model

High velocity impact events produce heterogeneous stress states in the material domain of interest. The stress state depends on a number of factors, such as geometry, microstructure, initial and boundary conditions, and the constitutive relations. Most of the current models for brittle ceramics are mainly phenomenological predicting the constitutive response in an average sense. These models do not capture every mechanism activated in high-rate behavior of the material observed in all relevant stress and strain loading conditions. To address this, the Tonge-Ramesh constitutive model [36] was developed, a large deformation framework that captures multiple mechanisms including shock formation, micromechanics-based damage evolution, granular plasticity and pore compaction in addition to capturing the random spatial variability in micromorphology.

1.4.1.1 Capturing Random Microstructure through varied Flaw Statistics

The random microstructure associated with each material point is captured through defining the local initial flaw population in the TR model. The flaw sizes and their densities sampled from the parent flaw size and flaw density distributions. A brief description of the process for selecting the representative flaw sizes and flaw densities for each family of flaws is provided here.

The statistics describing the initial flaw population in the TR model is associated with every discretization volume V_0. A flaw density $\hat{\eta}$ is defined in the model for the volume V_0 which is quantified as $\frac{N_f}{V_0}$ where N_f is the total number of flaws in the volume V_0. A local flaw distribution $\hat{g}(s)$ is also defined for the volume V_0. For a sufficiently large V_0 both $\hat{\eta}$ and $\hat{g}(s)$ converge to the parent flaw size distribution $g(s)$ and flaw density η. The evolution of damage Ω is computed within each V_0 as:

$$\Omega = \frac{1}{V_0} \sum_{i=1}^{N_f} s_i^3 \tag{1.11}$$

The binned representation of damage Ω in V_0 is:

$$\Omega = \sum_{k=1}^{N_{\text{bins}}} \omega_k s_k^3 \tag{1.12}$$

where N_{bins} is the total number of bins, ω_k is the bin flaw density calculated as $\frac{N_k}{V_0}$,

N_k is total number of flaws in k^{th} bin, and s_k is the representative flaw size for the k^{th} bin. The number of flaws within each bin residing in V_0 is assumed to be Poisson distributed random variable:

$$N_k = \text{Pois}[V_0 \bar{\omega_k}] \tag{1.13}$$

where $\bar{\omega}$ is the expected number of flaws within the k^{th} bin, found by multiplying the global flaw density with the probability that a flaw size s is between s_k and s_{k+1} ($\bar{\omega_k} = \eta(g(s_{k+1}) - G(s_k))$). The representative flaw size s_k for a particular bin is the mean flaw size within the bin. The bias binning technique (see chapter 2) is also adopted in the current work to reduce the number of bins to a reasonable quantity , in order to save computational time. Once the flaw families and respective local flaw densities for each family are assigned to each discretization volume V_0, the specific realization of the random microstructure is defined.

1.4.1.2 Thermodynamic Response via Equation of State

Impact events typically lead to shock wave formation in the material. This behavior is represented in the constitutive model through a pressure-volume relationship, which also couples the effect of temperature and pressure. The pressure-volume relationship (equation of state) is developed in the TR model using the basic formulation of Mie-Grüneisen equation of state. In particular the equation is:

$$p_s(J_e, \theta) = p_H(J_e)\left[1 - \frac{\Gamma_0}{2}(1 - J)\right] + \rho_0 \Gamma_0 \left[e_c(J_e) + c_\eta(\theta - \theta_0\right] \tag{1.14}$$

where (J_e) is the elastic volumetric deformation, J is the volumetric deformation, Γ_0 is the Grüneisen parameter, p_H is the pressure on principal Hugoniot, e_c is the cold energy, c_η is the specific heat at constant entropy, and θ is the temperature. Note that, details are given in [36], [49].

1.4.1.3 Micromechanics Model for Damage Evolution

Computational solution of the BVP requires discretization of the material domain in the macroscale. The material behavior at macroscale is considered as isotropic in TR model based on the assumption that the wing cracks are growing in the direction of maximum principal compression which is changing with macroscopic stress-state. At the microscale, the material behavior is anisotropic due to the nature of microcracking occurring at that scale (for details see chapter 3). At each material point, the damage due to microcracking is calculated using a micromechanics based damage model. The interaction between cracks is accounted for by using the self-consistent approach [23], [50], [36].

Similar to PR model, the 2D micromechanics problem uses a classical solution [41] of an inclusion in an infinite medium subjected to far-field biaxial loading. The maximum and minimum principal stresses obtained from the stress tensor at the macroscale material point are considered to be the far-field loading for the micromechanics problem. The effective property of the medium is obtained from the strain energy density of the representative volume V_0 with a population of cracks, based on

the function proposed by Grechka and Kachanov [29]. The original Grechka-Kachanov [29] strain energy density is modified by adding a fourth-order tensorial term [51] to account for the bulking observed in brittle material under compression. The modified expression for strain energy density is: The strain energy density is expressed as:

$$\begin{aligned} f =& \frac{1}{2}\tau : S_0 : \tau + \tau : \frac{1}{2V_0} \sum_{i}^{N_{cracks}} (n \otimes Z \otimes nA)^{(i)} : \tau + \\ & \tau : \frac{1}{2V_0} \sum_{i}^{N_{cracks}} \frac{Z_c a_i A_i}{\pi} (n \otimes n \otimes I + I \otimes n \otimes n - 2n \otimes n \otimes n \otimes n) : \tau \end{aligned} \tag{1.15}$$

where Z_n and Z_r are the crack compliance tensor in the normal and radial direction normalized by $\frac{a}{\pi}$. The parameter Z_c in equation (1.16) is a measure of the strength of coupling between loading normal and transverse to crack face, τ is the stress, ν_0 is the Poissons ratio, and E_0 is the Youngs modulus. Assuming the same orientation for all the cracks, the strain energy density at macroscale in terms of the scalar damage:

$$\begin{aligned} f_{iso} =& \Big(\frac{1+\nu_0}{2E_0} + \frac{\Omega}{30}(3Z_r + 2Z_n - 4Z_c)\Big)\tau : \tau \\ & - \Big(\frac{\nu_0}{2E_0} + \frac{\Omega}{30}(Z_r - Z_n + 8z_c)\Big)(\mathrm{tr}(\tau))^2 \end{aligned} \tag{1.16}$$

From equation (1.16), expressions for bulk Modulus $\kappa(\Omega)$ and shear modulus $G(\Omega)$ are obtained. The same strain energy density function is also used at microscale. However, the microscopic compliance tensor is obtained using the anisotropic form of the strain energy density function. The anisotropic compliance matrix associated

with the strain energy density function can be divided into three components as:

$$S_{aniso} = S_0 + \Delta S^{NIA}(\Omega) + \Delta S^{INT}(\Omega) \tag{1.17}$$

The first term of the equation (1.17) is the compliance of medium without cracks, the second term refers to the change in compliance due to presence of non-interacting cracks and the third term is the interaction term for cracks. S_0 is the isotropic compliance matrix. $\Delta S^{NIA}(\Omega)$ is obtained from the Grechka-Kachanov [29] model:

$$\Delta S^{NIA}_{ijlm} = \frac{8(1-\nu_0^2)}{3E_0(2-\nu_0)}((\alpha_{il})^p\delta_{jm} + (\alpha_{im})^p\delta_{jl} + (\alpha_{jm})^p\delta_{il} + 4(\beta_{ijml})^p \tag{1.18}$$

The crack interaction term for the anisotropic compliance matrix is:

$$\Delta S^{INT} = \frac{-2(1-\nu_0^2)}{2E_0} D(\hat{e}_2 \otimes \hat{e}_2 \otimes I + \hat{e}_2 \otimes \hat{e}_2 \otimes I - 2\hat{e}_2 \otimes \hat{e}_2 - \hat{e}_2 \otimes \hat{e}_2) \tag{1.19}$$

where $\hat{e}_1$ indicates the direction of the most compressive principal stress and $\hat{e}_2$ refers to the direction of crack face normal. The orientation density function is a delta function centered at $\hat{e}_1$ multiplied by $4 * \pi$. For details see [49].

TR model uses the same crack growth rate equation as used in PR model equation (1.6), and the damage is calculated using equation (1.11).

1.4.1.4 Granular Plasticity Model used in TR model

The material under dynamic compression experiences significant microcracking assumed to be at a damage level $\Omega = o.125$ and eventually creates local fragmented regions. At this highly damaged comminuted state, the material can be described as a granular material, [52] and the constitutive behavior is reasonably predicted by a granular flow model. Such approaches are adopted in [52], [53]. Since experimental observations on dynamic strength of the granular media under high confining pressure report a linear relationship between pressure and shear strength, the traditional Drucker-Prager plasticity model is used to represent the onset of plastic flow in TR model. The Drucker-Prager yield function is:

$$f(\tau) = \sqrt{\tau_{dev} : \tau_{dev}} - Y + A\left(\frac{\mathrm{tr}(\tau)}{\sqrt{3}} - B\right) \tag{1.20}$$

Where the parameter B represents cohesive forces between grains, the parameter A provides a measure of coupling between hydrostatic and deviatoric components, and Y is the deviatoric yield stress when the hydrostatic term is zero. The magnitude of the parameters is chosen as $A = 0.6$, $B = 0.1MPa$ and $Y = 0$ based on experiments on dry sand [54]. Granular flow in the TR model is considered to be a viscoplastic process, due to the time dependent rearrangement of grains occurring during granular flow. The tensorial viscoplastic rate of deformation d^{vp} is decomposed into a scalar

viscoplastic flow rate $\dot{\lambda}$ and an associative flow direction m:

$$d^{vp} = \dot{\lambda} m \tag{1.21}$$

The associative flow direction can be obtained from the yield surface equation:

$$m = n + A\hat{I} \tag{1.22}$$

where n is deviatoric unit tensor and I is the hydrostatic unit tensor. The details are given in [49].

1.4.1.5 Pore Collapse Mechanism

Ceramic materials usually contain pores. It is expected that the porosity of the material will reduce under high confining pressures. Pore collapse is represented by defining a traditional crush curve as:

$$J^{GP} = 1 + (J^{GP} - 1)J^2\left(\frac{P_c - P}{P_c - P_0}\right)^2 \tag{1.23}$$

J^{GP} is distension, P_0 represents the pressure at which the inelastic compaction begins at an initial distension of J_0^{GP}, and P_c is the pressure required for full densification. The crush curve is modified by assuming an exponential relation between distension

and crush pressure. The crush curve in the form of a yield surface is expressed as:

$$f_\phi(P, J^{GP}, J) = \begin{cases} \frac{P}{P_c - P_0} - \frac{P_0}{P_c - P_0} \exp\Big(- \frac{P_c - P}{2P_0(J_0^{GP} - 1)} (J^{GP} - J_0^{GP}) \Big) & P < P_0 \\ (J^{GP} - 1) - (J_0^{GP} - 1) J^2 \big(\frac{P_c - P}{P_c - P_0} \big) & P_0 \leq P < P_c \\ J^{GP} - 1 P > P_c \end{cases} \tag{1.24}$$

The crush curve above represents the quasi-static pore compaction. For details see [49].

1.4.1.6 Large Deformation Framework in TR model

To capture large deformation, the TR model uses a structural scale framework that incorporates the large deformation kinematic formulation outlined by Simo and Ortiz [55]. The traditional approach for multiplicative decomposition of deformation gradient

$$F = F^e F^{vp}$$

is adopted, which includes an elastic and viscoplastic part. The viscoplastic component of the deformation gradient is used to capture the granular plastic flow in the damaged material. For details of see [49].

1.5 Organization of this Thesis

The following chapters contain detailed information about the constitutive model development and integration. Chapter 2 discusses a generalized numerical technique to bin the random input parameters of a function to increase the computational efficiency. This approach decrease the number of function evaluations while maintaining a reasonable level of accuracy. The efficiency of the scheme is later verified by applying it in the context of a 2D micromechanics model to bin the initial flaw statistics. The same scheme with a new grid zooming function is applied to the TR constitutive model to select the initial flaw statistics for simulations under uniaxial compression. Chapter 3 discusses a micromechanics-based crack coalescence model using a self-consistent approach [23] to estimate the reduction in dynamic strength due to coalescence of cracks. An efficient reduced crack coalescence model is developed in chapter 4 to enable implementation of the coalescence mechanism into a full-scale mechanism-based constitutive model. The last part of chapter 4 discusses the implementation of the equivalent crack model in the TR constitutive model. A summary of the dissertation along with future directions are discussed in the last chapter.

Chapter 2

Sampling Input Flaw Statistics for Simulation

2.1 Introduction

Computational solutions to boundary-value problems (BVPs) typically discretize the domain into elements or similar finite subdomains. In modeling brittle materials, the constitutive response is characterized by the sub-grid-scale crack population enclosed within each individual finite element, which therefore varies between elements as a result of natural point-to-point variability in micro-morphology. If the expected number of cracks (defects are referred as cracks here to indicate the computational burden from tracking the growth of cracks nucleated from the defects) within each element is small, then they should be tracked explicitly as individual cracks. If, how-

ever, the model is at a length scale orders of magnitude larger than the individual crack spacing, then the element's constitutive model must be an upscaled representation of the element crack population. In a sampling-based approach, a macroscale property of the subdomain (such as a finite element's overall elastic compliance) is determined by sampled realizations of the domain's crack population. The sampling approach here is concerned with the case that such a property at a given time (t) is computed as a simple arithmetic average of some function $h(\hat{x}(t))$, evaluated for $p_{\max}$ individual time-varying crack "descriptors" $\hat{x}_p(t)$:

$$\overline{h}(t) \;= \Sigma[h(\hat{x}(t))] \;= \frac{1}{p_{\max}} \sum_{p=1}^{p_{\max}} h[\hat{x}_p(t)]\,. \tag{2.1}$$

Each crack descriptor, $\hat{x}_p(t)$, is an evolving set of values that describe micro-morphological attributes (such as length and orientation) of the p^{th} individual crack. Writing the function in the generic form of $h(\hat{x}(t))$ highlights the fact that the method derived here apply equally well to other applications that are unrelated to the crack-mechanics examples. As this is a sample-based approach, the notation $\Sigma[h(\hat{x})]$ refers to the expected value of the *sampled* population of crack descriptors, making it generally quite different from the expected value $E[h(\hat{x})]$ determined from the source distribution. Specifically, if the crack descriptors are random samplings taken from a known time-varying $p(\hat{x}, t)$ source probability density function (PDF), then the above summation

approaches the expected value of the function only as $p_{\max}$ approaches infinity:

$$\Sigma[h(\hat{x}(t))] \;\rightarrow E[h(\hat{x}),t] = \int h(\hat{x})p(\hat{x},t)d\hat{x} \qquad \text{as} \qquad p_{\max} \rightarrow \infty\,. \tag{2.2}$$

This method addresses the scale-bridging challenge, in which $p_{\max}$ is too large to explicitly model each $\hat{x}_p(t)$ descriptor realization, but $p_{\max}$ is not large enough to approximate $\Sigma[h(\hat{x}(t))]$ accurately by $E[h(\hat{x}),t]$. This method also outlines a basic framework for which the time-varying PDF $p(\hat{x},t)$ is never constructed explicitly, but is instead handled indirectly by using the *initial* PDF $p_0(\hat{X}) = p(\hat{x},0)$ to obtain realizations of *initial* crack descriptors $\hat{X}_p$ for $p = 1, 2, \ldots p_{\max}$, which are then evolved through application of a "growth model" that (for example) allows cracks to grow and kink in response to external loading. Accordingly, accuracy of this approach hinges upon accuracy of the *initial* crack descriptors and their binned approximations.

As a very basic (soon generalized) example, consider the following simple two-dimensional damage measure Ω for a collection (totaling $p_{\max}$ in number) of randomly oriented cracks:

$$\Omega = \frac{1}{p_{\max}} \sum_{p=1}^{p_{\max}} \eta\, \ell_p^2\,. \tag{2.3}$$

Here, there is just one descriptor (*i.e.,* each $\hat{x}_p$ is a set containing only the length, ℓ_p, of the p^{th} crack). The multiplier η, which is itself random, is the number of cracks per unit area in the two-dimensional medium (cracked plate). Consider a structural-mechanics simulation in which each finite element is regarded as a subdo-

main containing a finite number of cracks, $p_{\max}$. Further suppose that each individual crack length ℓ_p is exponentially distributed with mean 10 µm. Straightforward random number generation may be used to generate $p_{\max}$ sample crack lengths of any specified distribution, which are then substituted into Eq. (2.3) to calculate damage for each finite element. Element-to-element variability in damage is then the direct result of sampling variability in both the total number of cracks ($p_{\max}$) and their sizes ($\hat{x}_{p=1\ldots p_{\max}}$). Using $\eta = 10^8$ cracks per m^2, figure 2.1 shows a scatterplot of 100 sample values of the scaled global damage Ω. Whereas global damage Ω ranges from 0 to ∞, the scaled damage, defined by $\Omega/(1+\Omega)$, ranges from 0 to 1. Variability in damage decreases as the number of cracks within the macroscale finite element ($p_{\max}$) increases, primarily by using larger finite elements in the macroscale computational model (but also because $p_{\max}$ is itself a random variable). The rectangular region

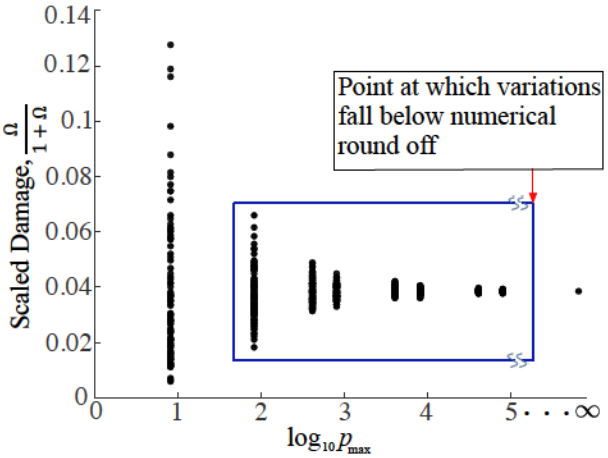

Figure 2.1: Scatterplot of 100 sample values of global scaled damage, $\Omega/(1+\Omega)$, for various values of the total number of cracks $p_{\max}$ in Eq. (2.1), with convergence to the homogenized expectation limit.

of figure 2.1 highlights several important points. The statistical scatter associated

with measures represented by Eq. (2.1) is not negligible for typical finite values of $p_{\max}$. After the scatter becomes imperceptibly small, these minuscule perturbations have little effect on elastic properties, but they still *strongly* affect intrinsic instabilities such as buckling or ultimate strength that are sensitive to flaw clustering [56]. Extending the definition of damage to 3D, the Appendix shows that the sampling error in Eq. (2.1) (which provides scale-dependent stimulus to activate localized instabilities) will be less than round-off error only when each individual finite element contains on the order of 5×10^{32} cracks, which (for typical microcracked materials) corresponds to a two-dimensional element size of millions of square kilometers, or a three-dimensional element size of hundreds of cubic kilometers. Addressing sub-grid-scale spatial heterogeneity of the crack population and the associated localization is therefore necessary for any reasonable computational model at scales for which finite elements typically fall in the scale-bridging range from cubic millimeters to cubic meters. While the need to model these perturbations is recognized [57], an explicit summation over each individual crack in Eq. (2.1) would entail untenable CPU and storage burdens as $p_{\max}$ increases to realistic values. This burden is exacerbated for higher-fidelity models that include more than just crack size and orientation in the flaw descriptors. For very small values of $p_{\max}$ (*i.e.,* left of the box in figure 2.1), calculation of Eq. (2.1) is not challenging, but explicit representations of individual cracks would be more appropriate in that case. Accordingly, it is assumed that the finite-element size (or equivalently $p_{\max}$) is large enough to warrant upscaling,

but not large enough to replace a discrete (realization) probability density function (PDF) with a continuous one for which variations in the crack population could be homogenized. Because it isn't feasible to track crack growth and evolution for all $p_{\max}$ cracks in every finite element, binning is required to predict the representative constitutive behavior of large populations of discrete cracks in a brittle medium. Binning is a process in which the large population of $p_{\max}$ cracks is replaced with a smaller number of $b_{\max}$ ($\ll p_{\max}$) cracks with characteristics that are representative of the much larger original population. A smaller number of bins increases efficiency, while a larger number of bins increases accuracy. As will be demonstrated in section 2.7, the binning method profoundly influences accuracy. A generalized binning approach is developed to provide a rigorous means for identifying the appropriate (and, optionally, optimized) bin descriptors and weightings, called occupancies. Briefly, the method maps the discrete distribution for the original large population of flaws to an approximate continuous distribution (somewhat analogous to approximating a large collection of point forces by piles of sand of the same weights), and then bin properties are identified from the Gauss points that would be used in numerical evaluation of expectation integrals over this approximate continuous distribution. Crack modeling serves only as an illustrative case study of the broader general framework for numerical tracking of a time-varying distribution $p(\hat{x}_p, t) = p(x_{p1}, x_{p2}, \ldots, x_{pN_{\text{rand}}}, t)$, which is a function of N_{rand} time-varying random variables: $\hat{x}_p = x_{p1}, x_{p2}, \ldots, x_{pN_{\text{rand}}}$ (*e.g.*, evolving crack size, $x_{p1} = \ell_p$, and orientation angle, $x_{p2} = \vartheta_p$, of the p^{th} crack)

assigned to $p_{\max}$ "points" (*e.g.,* cracks). In the interest of clarity, the discussions will presume exactly two random variables ($N_{\text{rand}} = 2$). Without any significant change in the framework to be developed in this work, the theory may be readily generalized to higher dimensions ($N_{\text{rand}} > 2$) and more complicated or coupled growth models by including additional pertinent random descriptors of each flaw, such as *two* spherical coordinate angles to quantify 3D flaw orientations, major and minor crack radii of ellipse-shaped cracks, surface roughness to accommodate friction, distance to the nearest neighboring crack to model crack interactions, *etc.* As this work uses damage mechanics only for examples of what is truly an abstract binning framework, the principles could be applied just as well to quasi-brittle media by, for example, including random morphological descriptors such as Schmid tensors. The binning framework isn't even limited to constitutive modeling.[1]The damage-mechanics examples in this work illustrate a practical framework for initializing and tracking changes in large populations of two random variables for a planar spatial domain (*e.g.,* a finite element) containing a total of $p_{\max}$ cracks, where $\hat{x}_p$ is an array that contains the

[1]In biology, for example, this binning framework could be used to identify a tractably small subset of millions of children (having known *initial* descriptors like height, weight, geographic location, socio-economic status *etc.* from hospital birth records if in developed nations); these representative (binned) children could then be tracked over their lifetimes to develop a growth model predictive of the larger ~ 7 billion world population. As a different application, this binning scheme could decimate a Gigapixel image down to Megapixels or smaller.

following random micro-morphological attributes (descriptors) for each crack:

$$\text{crack lengths:} \qquad x_{p1} = \ell_p \;:\; p = 1, 2, \ldots, p_{\max}\,, \tag{2.4a}$$

$$\text{crack orientations:} \qquad x_{p2} = \vartheta_p \;:\; p = 1, 2, \ldots, p_{\max}\,, \tag{2.4b}$$

$$\text{number of cracks:} \qquad p_{\max} = N_{\text{crack}}\,. \tag{2.4c}$$

A capital $\hat{X}$ is used to denote *initial* crack descriptors (ℓ_0, ϑ_0), which subsequently evolve to their current $\hat{x}(t)$ values in response to deformation. Assuming that a growth model is available governing such evolution in the flaw morphology, the binning phase of a simulation replaces an initial set of $\hat{X}_p$ crack-descriptor realizations, in which p ranges from 1 to $p_{\max}$, with a representative set of $\hat{X}_b$ flaw descriptors, where b ranges from 1 to $b_{\max}$. Of course, binning is appropriate only in situations where $b_{\max} \ll p_{\max}$. A sampling-based approach to statistical multiscale modeling begins by either directly defining the full-sized population from empirical data (*e.g.,* X-ray computed tomography of a microcracked specimen) or by generating statistical realizations of data from a given source distribution. In the latter case, the first step is to apply a scale-dependent Poisson process (or similar method) to obtain a statistical realization of the size of the sampled population, $p_{\max}$ (*e.g.,* the number of flaws in a finite element). For each p^{th} member of the population, standard methods such as inverse transform sampling (*cf.* [58]) are then applied to generate realizations of the descriptors $\hat{X}_p = [X_{p1}, X_{p2}]$, which are consistent with the *initial* continuous descrip-

tor PDF $p_0(X_1, X_2) = p_0(\ell_0, \vartheta_0)$. Correlations may be handled using techniques in [59]. The evolution of cracks from flaws are predicted by a micromechanical damage model. A function $p(\hat{x}, t)$, represents the evolving PDF resulting from application of the growth model to the initial population (*e.g.,* applying physical principles to induce crack growth and reorientation in response to an appropriate stress stimulus). The notation $p_0(\hat{X})$ refers to the initial PDF, $p(\hat{X}, 0)$. In upcoming equations, a PDF marked with an asterisk denotes a discrete distribution drawn from a corresponding non-asterisk continuous source distribution. A set of $p_{\max}$ "points" (*e.g.,* cracks) associated with the distribution $p(\hat{x}, t)$ is tracked through time using the growth models, which might (for example) apply linear-elastic fracture mechanics to suppress any growth until the stress is critically large, after which the crack size would increase at a rate that depends on the stress intensity [60], and the effective crack orientation might evolve through kinking [40], perhaps with revisions to account for crack interactions as well. Any further critical assessment of such theories is firmly outside the scope of this work, where our focus is on *model implementation* via a new binning paradigm that is flexible enough to accommodate a broad range of microphysical dynamic flaw morphology models. Recalling that $\hat{X}$ collectively denotes the initial descriptors (X_1, X_2), the initial sampled *discrete* distribution $p_0^*(\hat{X})$ approaches the source *continuous* distribution $p_0(\hat{X})$ in the limit as $p_{\max} \to \infty$. As for any discrete distribution, and as explained in greater detail in section 2.4, the discrete PDF $p_0^*(\hat{X})$ is a linear combination of $p_{\max}$ Dirac-delta functions centered at the actual descriptors

values, $\hat{X}_p$ for $p = 1, 2, \ldots p_{\max}$; the coefficients in this discrete expansion are uniform weights $w_p = 1/p_{\max}$. The primary goal of this method is to replace the initial discrete PDF $p_0^*(\hat{X})$ with an approximate *binned* (and still discrete) PDF that is a linear combination of a much smaller number of Dirac delta functions centered about representative descriptors values $\hat{X}_b$ for $b = 1, 2, \ldots b_{\max} \ll p_{\max}$, the coefficients in which are non-uniform weights (called occupancies) denoted W_b. This goal is accomplished in section 2.4 by replacing the large population of realizations with a much smaller representative population defined from Gauss points in numerical integration of a continuous approximation of the discrete distribution. Suppose that the initial distribution $p(X_1, X_2) = p(\ell_0, \vartheta_0)$ for the two flaw descriptors in equation (2.4) is known. Then each flaw in a population can be assigned its two descriptors values by applying an appropriate mapping from two uniform random variables (r_1, r_2), each ranging from 0 to 1, to physical realizations (X_1, X_2). For simplicity, the example provided later in Eq. (2.17) uses an uncorrelated distribution, but the concept applies to correlated distributions as well. An initial "population" is the collection of such points, $\hat{r}_p$ for $p = 1, 2, \ldots p_{\max}$ uniformly distributed in a reference unit square (probability space) and the associated non-uniformly distributed $\hat{X}_p$ initial descriptors points mapped from the unit square. Current $\hat{x}_p = (x_{p1}, x_{p2})$ descriptorsof the p^{th} member of the population are computed by applying a deterministic growth/evolution model to the initial $\hat{X}_p = (X_{p1}, X_{p2})$ values.

The aim of this scheme is to estimate equation (2.1) accurately without requiring

any particular assumptions about the nature of the generic function $h[\hat{x}]$. The summation over $p_{\max}$ in equation (2.1) is estimated as a weighted summation over a much smaller $b_{\max}$ bins, where the weights are called occupancies. We note similarities between this expression and other work using summations of random variables, such as polynomial chaos, Karhunen-Loeve expansion, spectral representation and modal decomposition. These techniques approximate random variables and stochastic processes by the summation of functions (*e.g.,* harmonic functions for spectral representation) of simpler random variables [61, 62, 63, 64]. In contrast to these methods, this method does not emphasize a series expansion of random variables or processes, but instead it is focused on an efficient lumped representation of a time-varying quantity (such as damage) using binning techniques.

There is a vast body of literature on binning schemes applied to different fields of science ranging from astrophysical measurement techniques to image processing methods. A method to bin X-ray data using weighted Voronoi tessellation is described in [65]. The X-ray image is spatially discretized into bins of nearly uniform signal-to-noise ratio. Another similar technique to bin integral-field spectroscopic data using Voronoi tessellation is proposed in [66]. There are works on different probability binning algorithms developed for comparing univariate and multivariate distributions. For a univariate distribution, binning is done in such a way so that any single event selected randomly from the distribution has the same probability of falling into any of the bins. For a bivariate distribution, a large number of smaller

bins containing densely packed data and a small number of large bins with less dense data are generated [67, 68]. All of this prior work describes specific procedures to efficiently bin large data sets, which is the goal of the current scheme. However, this method generalizes and formalizes these ideas by developing bins in the context of the probability space (herein referred to as the "reference space").

Working in the probability reference space evokes parallels in random sampling procedures, such as stratified sampling or Latin hypercube sampling. These techniques sample from pre-defined subsets of the probability space, which provides higher accuracy from a smaller number of samples [69, 70, 71]. The concept of "zooming" these subsets to identify optimal unevenly spaced bins in the probability space is only marginally similar to importance sampling, which samples random variables from a transformed distribution designed to optimize convergence to a particular output (such as an expectation integral, or a failure probability) [72, 73, 74, 75, 76, 77, 78]. The current method differs from these techniques in the fundamental goal of representing equation (2.1) as a reduced summation of binned variables in order to *capture* (not minimize) discrepancies between a sample's mean and the expected value of its source distribution, but otherwise complements or extends existing method where possible.

Overall, the approach outlined for binning is appealing because it replaces a very large initial population of cracks with a much smaller representative "binned" population. Accuracy of an initial binned population of cracks is herein shown to provide

accuracy of predictions of subsequent evolved (stress-induced) damage. In upcoming examples, a simple growth model will be applied to the initialized binned population and compared to the same growth model applied to the full-sized population. The quality of the binning scheme will be then assessed quantitatively in section 2.7.2 by comparing two methods for evaluating deformation-induced strength degradation: (1) the BASELINE method uses the original arithmetic averages of damage involving equally weighted terms over the original very large number of $p_{\max}$ points found by a Poisson process, the number of which is theoretically unbounded, while (2) the BINNED method uses bin-weighted averages over $b_{\max} \ll p_{\max}$ bins, the number of which is bounded. It will be seen that around two orders of magnitude reduction in computational burden (CPU and internal variable storage) can be achieved at the cost of less than 1% relative error in predictions of the evolved stress-strain response curve.

2.2 Mathematical Framework for Random Variable Cluster Tracking

This section outlines a mathematical framework for numerically modeling a continuously evolving joint PDF $p(\hat{x}, t)$ during a time interval $(t_1 \leq t \leq t_2)$. Details of any *specific* application of this binning and evolution framework fall outside the scope of this paper. However, some results from statistical crack mechanics are provided to

illustrate the concepts and to demonstrate its practical advantages. The mathematical framework does not include sources (*e.g.,* "birth" of new cracks via nucleation), sinks (*e.g.,* "death" of a crack via a healing process such as sintering), splitting (*e.g.,* a single crack being represented as equivalent to two different cracks, as might occur when modeling crack kinking), or merging (*e.g.,* crack coalescence [34]). The methodology easily accommodates these complications, but they are ruled out purely for clarity of this first presentation of the binning scheme. When sources and sinks are disallowed, the time evolution of any given overall (macro-scale) distribution property is determined exclusively from the time history of motion of the individual population points through state ($\hat{x}$) space. A binning scheme essentially replaces subpopulations with single representative points having an "occupancy" defined to quantify the size of the original subpopulation relative to the entire population. Similar to continuum deformation analysis, a motion function is defined as χ,

$$\hat{x} = \chi(\hat{X}, t) \ , \tag{2.5}$$

which is treated as a mapping from the initial random descriptor array $\hat{X} = \{X_1, X_2\}$ to the current array $\hat{x} = \{x_1, x_2\}$. This mapping is determined exclusively from the (presumed available) growth model. The p^{th} point $\hat{X}_p$ in a population transforms under the growth model to become $\hat{x}_p = \chi(\hat{X}_p, t)$ at some later time. The premise of this work is that accuracy of the evolved population can be achieved by applying the

growth model to a binned *initial* subpopulation. Properties of a continuous population are typically expressed as weighted integrals over the state space (*i.e.,* the space of admissible values of the random variables, x_1 and x_2), where the weight function is the probability density function (PDF). Numerical evaluation of such integrals requires tessellating the integration domain ($\hat{x}$ state space) into a collection of zones or "bins," which are analogous to finite elements used on a spatial domain. As is known from elementary calculus, a difficulty in binning (*i.e.,* laying down a grid) on state space is that the random variables of interest might range over infinite domains. For example, common PDFs used to describe crack length typically allow crack sizes in the range from 0 to ∞. Evaluating integrals over bins therefore requires mapping the infinite state space to a finite reference space, the natural choice for which is probability space, whose coordinates $\{r_1, r_2\}$ (denoted collectively by $\hat{r}$) each range from 0 to 1. The time-varying mapping from $\hat{r}$ to $\hat{x}$ is denoted $\hat{x} = g(\hat{r}, t)$. The *initial* population properties are generated by applying this mapping at t=0. That is, letting $\{X_1, X_2\}$ be collectively denoted $\hat{X}$, the initial mapping is $\hat{X} = G(\hat{r}) = g(\hat{r}, 0)$. A notional example of these initial and evolved mappings for statistical crack mechanics is provided in Fig. 2.2, where the probability reference $\hat{r}$-space is the unit square in the figure's first two rows. The initial state $\hat{X} = \{\ell_0, \vartheta_0\}$ and a notional current state $\hat{x} = \{\ell, \vartheta\}$ are depicted in the bottom row as mappings of the reference space. As seen, severe distortions are anticipated in the convected grid that represents the evolving mapping function $g(\hat{r}, t)$ in a way that might represent axial splitting

(producing the spike in the distribution at a crack normal angle of $\vartheta = 0$, which is measured from the horizontal and thus represents an evolution towards *vertical* cracking). The anticipated severe mesh distortion in this notional mapping would preclude using Lagrangian finite-element methods to model flaw evolution, as they would suffer the same numerical difficulties (especially inversion) as seen when conventional Lagrangian elements are applied to large-deformation continuum-mechanics problems such as penetration. Moreover, a continuous Lagrangian mapping would not easily lend itself to enhancements such as flaw birth and death associated with nucleation and/or coalescence. The binning strategy outlined in this section refactors some key concepts from large-deformation numerical methods to easily address these binning evolution challenges. As with reference spaces in continuum mechanics, a presumed continuity of the mapping ensures that discrete points (shown as dots) are stationary in the reference space (*i.e.,* their $\hat{r}$-coordinates are the same at both the initial and current times). The domains spanned by admissible ranges of $\hat{r}$, $\hat{X}$, and $\hat{x}$ are herein called the the *reference*, *initial*, and *state* spaces, respectively. Thus, for example, the reference space in the 2D crack-mechanics application is a unit square (middle row of figure 2.2), and it maps to initial and state spaces that are infinite in one direction (corresponding to crack length ranging from 0 to ∞, as seen in the bottom row of figure 2.2). This section describes how to transform abstract (continuous and discrete) expectation integrals on the initial ($\hat{X}$) state space to integrals on the reference ($\hat{r}$) space through the use of the mapping connecting those spaces. Various binning

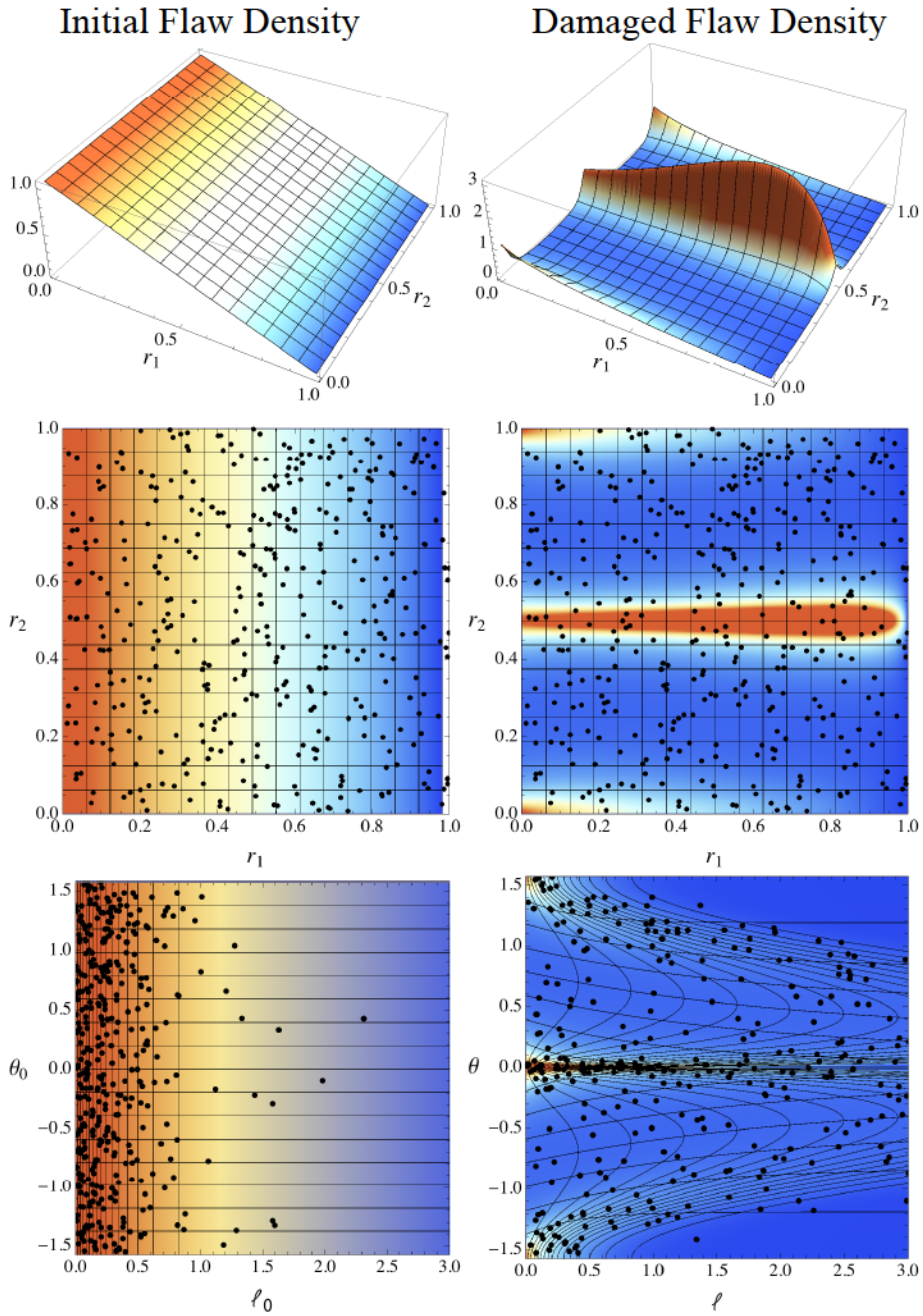

Figure 2.2: Notional initial and damaged states colored by probability densities. The pinching and stretching in the notional damaged state (right column) corresponds to vertical splitting in which cracks grow such that $\vartheta \to 0$. Colors (and altitudes in the top row) depict $p_0(G(\hat{r}))$ and $p(g(\hat{r}), t)$, which are reference descriptions of the initial and evolved non-uniform PDFs for $\hat{X}$ and $\hat{x}$, respectively. Crack realizations (dots) are uniformly distributed in the reference $\hat{r}$ space and hence clustered in $\hat{X}$ and $\hat{x}$ state spaces. With a uniform grid in reference space, the same number of dots exists, on average, within each grid cell (a nonuniform grid is later advocated to improve accuracy).

strategies will then emerge from different approaches to approximating the integral in reference space. A typical illustrative mapping from statistical crack mechanics is then provided in section 2.3. In section 2.4 the mathematical framework for large-population binning scheme is developed in reference space. The remainder of this section establishes the overall principles in a generic context that is applicable beyond the damage-mechanics applications that are used in subsequent examples. Let G and g respectively denote the mapping functions from the reference ($\hat{r}$) probability space to the initial ($\hat{X}$) and evolving ($\hat{x}(t)$) realization state spaces:

$$\hat{X} = G(\hat{r}) \qquad \text{and} \qquad \hat{x} = g(\hat{r}, t)\,. \tag{2.6}$$

figure 2.2, for example, used a typical initial crack-property mapping, $\hat{X} = G(\hat{r})$, corresponding to uniformly random flaw orientations and exponentially distributed flaw sizes, as defined by specific formulas in the next section. The evolved mapping, $\hat{x} = g(\hat{r}, t)$, exists only implicitly through application of the previously discussed growth model, $\hat{x} = \chi(\hat{X}, t)$, so that

$$g(\hat{r}, t) = \chi(G(\hat{r}), t)\,. \tag{2.7}$$

Associated with the mappings are the following $N_{\text{rand}} \times N_{\text{rand}}$ transformation matrices:

$$\hat{\hat{G}}(\hat{r}) = \frac{\mathrm{d}G(\hat{r})}{\mathrm{d}\hat{r}} \qquad \text{and} \qquad \hat{\hat{g}}(\hat{r}) = \frac{\partial g(\hat{r}, t)}{\partial \hat{r}}\,. \tag{2.8}$$

That is,

$$G_{ij} = \frac{\partial X_i}{\partial r_j} \qquad \text{and} \qquad g_{ij} = \frac{\partial x_i}{\partial r_j} \,. \tag{2.9}$$

The indices i and j each range from 1 to N_{rand}. We denote the determinants of these matrices by an overline:

$$\overline{G}(\hat{r}) = \det \hat{\hat{G}}(\hat{r}) \qquad \text{and} \qquad \overline{g}(\hat{r}, t) = \det \hat{\hat{g}}(\hat{r}, t) \,. \tag{2.10}$$

By excluding random variable sources and sinks, we assert a conservation principle that relates the initial and current joint PDFs, $p_0(X_1, X_2)$ and $p(x_1, x_2, t)$. Analogous to the integral statement of conservation of mass in continuum mechanics, and noting that the distribution on the reference configuration is uniform,

$$\int_{\Omega_X} p_0(\hat{X}) \, \mathrm{d}X_1 \mathrm{d}X_2 = \int_{\Omega_x(t)} p(\hat{x}, t) \, \mathrm{d}x_1 \mathrm{d}x_2 = \int_{\Omega_r} \mathrm{d}r_1 \mathrm{d}r_2 \,. \tag{2.11}$$

Here, Ω_r is an arbitrary contiguous subdomain in the reference ($\hat{r}$) space, while the subdomains Ω_X and $\Omega_x(t)$ are the images of Ω_r under the mappings in equation (2.6). The Jacobians defined in Eq. (2.10) may be used to perform a change of variables that re-casts all three integrals to be evaluated on the reference domain:

$$\int_{\Omega_r} p_0(G(\hat{r})) \, \overline{G}(\hat{r}) \, \mathrm{d}r_1 \mathrm{d}r_2 = \int_{\Omega_r} p(g(\hat{r}, t)) \, \overline{g}(\hat{r}, t) \, \mathrm{d}r_1 \mathrm{d}r_2 = \int_{\Omega_r} \mathrm{d}r_1 \mathrm{d}r_2 \,. \tag{2.12}$$

This conservation statement must hold for any Ω_r, thus implying equality of the integrands:

$$p_0(G(\hat{r}))\,\overline{G}(\hat{r}) = p(g(\hat{r},t))\,\overline{g}(\hat{r},t) = 1\,. \tag{2.13}$$

Since $\hat{X} = G(\hat{r})$ and $\hat{x} = g(\hat{r},t)$, these imply that

$$\boxed{p_0(\hat{X}) = \frac{1}{\overline{G}(G^{-1}(\hat{X}))}} \quad \text{and} \quad \boxed{p(\hat{x},t) = \frac{1}{\overline{g}(g^{-1}(\hat{x}),t)}\,.} \tag{2.14}$$

n other words, the PDF for $\hat{X}$ or $\hat{x}$ is merely the reciprocal of the Jacobian of the mapping from the reference space to the actual space. Consequently, the time-varying mean of any generic function $h(\hat{x})$ is

$$E[h(\hat{x}(t))] \equiv \int\limits_{\Omega_x(t)} h(\hat{x}(t))p(\hat{x},t)\,\mathrm{d}x_1\mathrm{d}x_2 = \int\limits_0^1\int\limits_0^1 h(\hat{x}(\hat{r},t),t)\,\mathrm{d}r_1\mathrm{d}r_2\,. \tag{2.15}$$

The final form was found by noting that $\mathrm{d}x_1\mathrm{d}x_2 = \overline{g}\,\mathrm{d}r_1\mathrm{d}r_2$, where $\overline{g}$ is the Jacobian of the mapping in equation (2.6), which (using equation (2.14)) then cancels the PDF $p(\hat{x},t)$ because they are reciprocals. The implication of this result is that any expectation integral of $h(\hat{x})$ over the current state $\hat{x}$ (*i.e.,* an integral weighted by the PDF) may be replaced by a regular (unweighted) integral of $h(\hat{x}(\hat{r},t))$ over reference space (*i.e.,* the unit square spanned by r_1 and r_2). Various binning schemes will be seen to result from different ways to numerically evaluate such integrals. Just as numerical methods for boundary-value problems (BVPs) ultimately lead to the need

to evaluate integrals over spatial domains, this work ultimately requires integrals over reference probability space. The integration scheme developed here is similar in character to the Material Point Method (MPM), which is used to solve large-deformation history-sensitive BVPs [79, 80].

2.3 Example: A Typical Crack-Mechanics Mapping

The mapping depicted in the the first column of figure 2.2 was generated using the following commonly adopted choices for initial flaw descriptors ($X_1{=}\ell_0$ and $X_2{=}\vartheta_0$):

$$\text{initial crack size PDF:} \qquad p_1(\ell_0) = \begin{cases} \frac{1}{\ell_0} e^{-\ell_0/\overline{\ell_0}} & \text{if} \quad \ell_0 > 0 \\ 0 & \text{if} \quad \ell_0 < 0\,, \end{cases} \tag{2.16a}$$

$$\text{initial crack orientation PDF:} \qquad p_2(\vartheta_0) = \begin{cases} \frac{1}{\pi} & \text{if} \quad -\frac{\pi}{2} < \vartheta_0 < \frac{\pi}{2} \\ 0 & \text{if} \quad \text{otherwise}\,, \end{cases} \tag{2.16b}$$

$$\text{initial joint size \& orientation PDF:} \qquad p_0(X_1, X_2) = p_1(X_1) p_2(X_2)\,. \tag{2.16c}$$

where $\overline{\ell_0}$ is the mean initial crack size. The joint distribution $p_0(X_1, X_2)$, which is denoted compactly as $p_0(\hat{X})$, is separable here as a result of a non-correlation assumption, which produces a rectilinear initial grid (and does not preclude correlations in general applications). The corresponding initial cumulative distributions functions (CDFs) are obtained integrating the initial PDFs in Equations (2.16a) and (2.16b), which is the first step to deriving the mapping functions that generate initial crack descriptor realizations from random reals on $[0, 1)$. For example, the mapping function required to generate a random realization of initial crack length $X_1 = \ell_0$ is found by setting $P_1(\ell_0) = r_1$ and then solving for ℓ_0. Here, $P_1(\ell_0)$ is the CDF associated with the PDF $p_1(\ell_0)$. A similar analysis for the crack orientation mapping then together defines the mapping, $\hat{X} = G(\hat{r})$, which transforms $\hat{r} = \{r_1, r_2\}$ on the unit square reference space to $\hat{X} = \{X_1, X_2\} = \{\ell_0, \vartheta_0\}$ on the initial state space:

$$X_1 = \quad \ell_0 \; = \overline{\ell_0} \ln\left(\frac{1}{1 - r_1}\right) \tag{2.17a}$$

$$X_2 = \quad \vartheta_0 \; = \pi(r_2 - \tfrac{1}{2})\,. \tag{2.17b}$$

For correlated distributions, the mapping $\hat{X} = G(\hat{r})$ would simply have X_1 and X_2 each depending on *both* r_1 and r_2. In this simple case of an uncorrelated mapping, X_1 depends only on r_1, while X_2 depends only on r_2, making the Jacobian matrix

(G_{ij}) in equation (2.9) diagonal. The determinant in equation (2.10) is

$$\overline{G} = \frac{\pi \overline{\ell_0}}{1 - r_1} \,. \tag{2.18}$$

Recalling that the PDF is the reciprocal of the determinant, it follows that the reference description of the initial probability density, $p_0(G(\hat{r})) = 1/\overline{G}(\hat{r})$, varies *linearly* with r_1, hence giving the flat ramp shape in the upper-left image of figure 2.2. The grid in the left-hand side of figure 2.2 represents the nominal undamaged mapping, $\hat{X} = G(\hat{r})$. The reciprocal of the Jacobian of this mapping is the nominal undamaged PDF. The dots (points) on these plots represent realizations of the PDF. The dots are statistical realizations drawn from a uniform distribution on the reference space (the total number of dots is generated via a Poisson process based on the size of the physical finite element and the average number of cracks per unit volume, which is treated as a material property). Because the dots are realizations, they are not themselves uniformly distributed and hence they have natural clustering and gaps. Application of the nominal mapping, $\hat{X} = G(\hat{r})$, transforms the points in the reference space to a finite number of realizations (dots) in the initial state space. The nominal undamaged mapping, $\hat{X} = G(\hat{r})$, will be herein required to be invertible in order to establish bin weights. Thereafter, the bins evolve under the growth model, hence making the mapping function $\hat{x} = g(\hat{r}, t)$ of this section purely notional. This strategy for statistical damage evolution avoids numerical pitfalls of convected grid

entanglement and it permits the growth law to be discontinuous. In other words, assuming existence of a growth model, the binning strategy may focus *exclusively* on initialization, the goal of which is to replace an intractably large population of cracks (dots in the plot) with a *much* smaller representative (binned) population of cracks.

2.4 Mathematical Framework for Binning Scheme

For spatial domains containing extremely large numbers of realizations (*e.g.,* finite elements larger than a few millimeters in breadth), there might be thousands of cracks within each finite element, making it impractical to explicitly evaluate the summation in equation (2.1). When modeling larger structures, such as armored vehicles or dams, each finite element might even contain *millions or trillions* of cracks. Even though these large populations have discrete distributions that are almost imperceptibly close to the nominal PDF from which they were generated, they still induce aleatory uncertainty in the stress field that is many of orders of magnitude larger than numerical round-off. These slight perturbations have little influence on stable material response, but they strongly dominate the character of unstable localization phenomena such as macroscale fracturing or formation of compaction zones [57, 56, 81], which is why it is essential for a population of $b_{\max}$ cracks to accurately

capture clustering of the original $p_{\max}$ cracks.

$$\overline{h}(t) = \int_{\Omega_x} h(\hat{x})\, p^*(\hat{x}, t)\, \mathrm{d}\Omega_x \ , \tag{2.19a}$$

where, using Dirac-delta functions, the *discrete* distribution $p^*(\hat{x}, t)$ sampled from the generally *continuous* source PDF $p(\hat{x}, t)$ is

$$p^*(\hat{x}, t) \equiv \sum_{p=1}^{p_{\max}} w_p \delta[\hat{x} - \hat{x}_p(t)] \qquad \text{in which} \quad w_p \equiv \frac{1}{p_{\max}}. \tag{2.19b}$$

Each $\hat{X}_p$ initial realization is created at time t=0 by first generating an array $\hat{r}_p$ of realizations of uniformly distributed random variables in the range from 0 to 1. The initial mapping function is then applied to obtain initial descriptor realizations $\hat{X}_p = G(\hat{r})$. Each damaged realization $\hat{x}_p(t)$ is obtained by applying the (presumed available) growth model $\hat{x}_p(t) = \chi(\hat{X}, t)$. Recalling that birth and death are disallowed for now, the $\hat{r}_p$ arrays do not change in time, so each time-varying $\hat{x}_p(t)$ is associated with a constant $\hat{r}_p$ through the mapping,

$$\hat{x}_p = \chi(\hat{X}_p, t) = \chi(G(\hat{r}_p), t) = g(\hat{r}_p, t) \ . \tag{2.20}$$

In the crack-mechanics application, the $g(\hat{r}_p, t)$ is constructed and applied *explicitly* as $G(\hat{r}_p)$ only at time t=0. Thereafter, it exists only implicitly, as each $\hat{x}_p(t)$ is directly integrated through time using the evolution equations of the growth model

(see section 2.7). In terms of this mapping, the desired expectation summation in equation (2.1) and its limit in equation (2.2) are expressed as simplified sums and integrals *over the reference probability space*,

$$\text{For } p_{\max} < \infty \qquad \overline{h}(t) = \frac{1}{p_{\max}} \sum_{p=1}^{p_{\max}} h(g(\hat{r}_p, t)) \tag{2.21a}$$

$$\text{As } p_{\max} \to \infty \qquad \overline{h}(t) \to \int_{\Omega_r} h(g(\hat{r}, t))\, \mathrm{d}\Omega_r \,. \tag{2.21b}$$

As in equation (2.19a), the discrete sum in equation (2.21a) may be written equivalently as

$$\boxed{\overline{h}(t) = \int_{\Omega_r} h(g(\hat{r}, t))\, \mathscr{P}^*(\hat{r})\, \mathrm{d}\Omega_r \qquad \text{where} \qquad \mathscr{P}^*(\hat{r}) \equiv \sum_{p=1}^{p_{\max}} w_p \delta_p(\hat{r}) \,.} \tag{2.22}$$

As before, w_p denotes (all equal) point weights, and δ_p refers to a Dirac delta function centered at the p^{th} point, except (unlike equation (2.19b)) applied in reference probability space:

$$w_p \equiv \frac{1}{p_{\max}} \qquad \text{and} \qquad \delta_p(\hat{r}) \equiv \delta[\hat{r} - \hat{r}_p] \,. \tag{2.23}$$

The domain Ω_r denotes the unit square (or hypercube in higher-dimensional applications) defining probability space, and the function $\mathscr{P}^*(\hat{r})$ is the *discrete* PDF corresponding to random numbers $\{\hat{r}_1, \ldots, \hat{r}_{p_{\max}}\}$ sampled from the *continuous* uni-

form source PDF $\mathscr{P}(\hat{r}) = 1$. The limit $\mathscr{P}^*(\hat{r}) \to 1$ is approached very slowly as $p_{\max} \to \infty$, so the summation in equation (2.21a) is not generally approximated well by equation (2.21b) even when the number of realization points is *extremely* large. The terms "grid" and "cell" are herein used for tesselation of probability space in order to distinguish it from tesselation of the physical domain into a "mesh" of "finite elements." The reference probability grid may be structured or unstructured, but a simple rectilinear grid is used purely for simplicity. If the rectilinear grid is furthermore *evenly spaced* (such as the one in the middle row of figure 2.2), then each grid cell contains, on average, the same number of realizations. The total number of points ($p_{\max}$) is set via a Poisson process, and the actual number of realizations within each cell varies because of clustering or gaps associated with uniformly distributed realizations of these points on the reference domain. Conditions favoring non-uniform and non-structured grids are discussed in section 2.4.1, and these situations are accommodated naturally in the binning framework because, as in conventional FEM, each grid cell has nodes and associated shape functions regardless of its logical shape (rectangle, triangle, *etc.*). Borrowing both notational conventions and mapping principles from the Material Point Method (*cf.* [80]), we let a subscript i always vary over the number of grid nodes, $i_{\max}$, while the subscript p ranges over the number of realization points, $p_{\max}$. Thus, for example, $\hat{r}_i$ denotes the location of the i^{th} grid node in the reference probability space, while $\hat{r}_p$ denotes the location of the p^{th} realization point in that same space. Letting $S_i(\hat{r})$ denote the shape function associated with

the i^{th} grid node in probability space, the number of realization points mapped to the i^{th} grid node is defined to be

$$N_i = \sum_{p=1}^{p_{\max}} S_i(\hat{r}_p)\,. \tag{2.24}$$

Each node's weight w_i, volume V_i, and "Delta-pulse" function $\Delta_i(\hat{r})$ is defined respectively by

$$w_i \equiv \frac{N_i}{p_{\max}}\,, \qquad V_i \equiv \int_{\Omega_r} S_i(\hat{r})\mathrm{d}\Omega_r\,, \qquad \text{and} \qquad \Delta_i(\hat{r}) \equiv \frac{S_i(\hat{r})}{V_i}\,. \tag{2.25}$$

These give the following *continuous* approximations to the formulas in equation (2.22):

$$\boxed{\overline{h}(t) \approx \int_{\Omega_r} h(g(\hat{r},t))\; q(\hat{r})\; \mathrm{d}\Omega_r \qquad \text{where} \qquad q(\hat{r}) \equiv \sum_{i=1}^{i_{\max}} w_i \Delta_i(\hat{r})\,.} \tag{2.26}$$

Since the grid shape functions in probability space are identical to those used in a conventional FEM setting, they satisfy the partition of unity property that $\sum_i S_i(\hat{r}) = 1 \;\; \forall \hat{r}$, and therefore

$$\sum_{i=1}^{i_{\max}} N_i = p_{\max} \qquad \text{and} \qquad \sum_{i=1}^{i_{\max}} w_i = 1\,. \tag{2.27}$$

From the definition of V_i in equation (2.25), note that $\int_{\Omega_r} \Delta_i(\hat{r}) = 1$. Furthermore, the support domain for $\Delta_i(\hat{r})$ goes to zero as the cells containing that node shrink

to zero. In the limit as all cell sizes go to zero, each Delta-pulse function $\Delta_i(\hat{r})$ approaches a Dirac-delta function $\delta[\hat{r} - \hat{r}_i]$, and each N_i goes to either 1 or 0. The definition of the Dirac delta function (*cf.* [82]) therefore ensures that, as the size of the largest cell goes to zero,

$$q(\hat{r}) \to \mathscr{P}^*(\hat{r})\,. \tag{2.28}$$

This convergence of the approximate continuous PDF, $q(\hat{r})$ to the actual discrete PDF $\mathscr{P}^*(\hat{r})$ is illustrated later in the example of figure 2.4. Applying Gauss quadrature and looping over Gauss points in the interior of the grid cells, the integral in equation (2.26) may be evaluated approximately as

$$\boxed{\overline{h}(t) \approx \sum_{g=1}^{g_{\max}} h_g(t)\, W_g \quad = \sum_{b=1}^{b_{\max}} h_b(t)\, W_b\,,} \tag{2.29}$$

where, letting k_g denote the g^{th} conventional scaled Gauss weight[2]

$$W_g \equiv k_g q(\hat{r}_g) \qquad \text{and} \qquad h_g(t) \equiv h(\hat{x}_g(t))\,. \tag{2.30}$$

The summation over "g" ranges over all $g_{\max} = c_{\max} N_{\text{gauss}}$ Gauss points in the domain, where $c_{\max}$ is the number of grid cells and N_{gauss} is the number of Gauss points per cell. The sum over "b" ranges over all bins, which are simply the Gauss points that have nonzero W_g weight values; this distinction is important only in cases of high grid

[2]For an integral over a cell of length L_{cell}, the conventional scaled Gauss weight is, $k_g = \frac{L_{\text{cell}}}{L_{\text{gauss}}} K_g$, where K_g is the g^{th} standard reference Gauss weight, and L_{gauss} is the length of the standard Gauss reference domain (usually $L_{\text{gauss}} = 2$ corresponding to a Gauss domain from -1 to 1).

refinement, where some grid cells might be empty and hence have zero weight (making their Gauss points *not* bins). Accordingly, the total number of bins is bounded by the number of Gauss points on the grid ($b_{\max} \leq g_{\max}$), irrespective of the size $p_{\max}$ of the original population from which the bins are generated.

Equation (2.30) uses the fact that $\hat{x}_g(t) = g(\hat{r}_g, t)$ gives the time-varying properties (*e.g.,* crack length and angle) associated with the g^{th} Gauss point. Using k_g as the conventional Gauss weight for reference-space integrals over the cell containing the g^{th} Gauss point, $q(\hat{r}_g)$ is the nodal weighting function $q(\hat{r})$ evaluated at the g^{th} Gauss point $\hat{r}_g$. With this scheme, the mapping function is evaluated only at the $\hat{r}_g$ Gauss points, which are always on the interior of the domain Ω_r, away from problematic boundaries and hence never cause the mapping function to evaluate to infinity. Additionally, the W_g weights do not vary with time, and hence they may be treated as constant properties of each Gauss point on the reference configuration.

During initialization, the source mapping is used to convert all r_b reference arrays to physical descriptor arrays: Namely, the initial descriptors of the b^{th} bin are found by

$$\hat{X}_b = \hat{x}_b(0) = g(\hat{r}_b, 0) = G(\hat{r}_b) \ . \tag{2.31}$$

Only bin data (i.e., nonzero W_b and associated initialized $\hat{x}_b$ arrays) are retained after the initialization phase. The index b ranges up to the number of bins, which are merely the Gauss points with nonzero occupancy, and hence $b_{\max} \leq g_{\max}$. Each $\hat{x}_b$ descriptor is evolved as described in section 2.7, with its weight (the bin occupancy

W_b) remaining constant in the absence of nucleation or coalescence. Of course, a nucleation/coalescence model would require a theory for changing bin occupancies under the constraint that they always sum to unity.

Direct use of the reference configuration is not needed after the initialization phase. Instead, by replacing the original large population's equal weights, $w_p = 1/p_{\max}$, with the W_b bin occupancies, the binning calculations effectively reduce the original problem,

$$\overline{h}(t) = \sum_{p=1}^{p_{\max}} h(\hat{x}_p(t)) w_p \qquad \text{for which} \qquad p^*(\hat{x}, t) \equiv \sum_{p=1}^{p_{\max}} w_p \delta[\hat{x} - \hat{x}_p(t)]\,, \tag{2.32}$$

to

$$\overline{h}(t) \approx \sum_{b=1}^{b_{\max}} h(\hat{x}_b(t)) W_b \qquad \text{for which} \qquad p^*(\hat{x}, t) \approx \sum_{b=1}^{b_{\max}} W_b \delta[\hat{x} - \hat{x}_b(t)]\,, \tag{2.33}$$

where it is mentioned that the MPM-style notation is adopted in which the subscript "p" or "b" indicates whether the array contains point data or bin data, respectively. The bin occupancies would be additionally dependent on time for models that allow sources and sinks (*e.g.,* crack nucleation and coalescence), but such features merely influence the growth model without affecting the *initialization* established by the binning scheme.

It is demonstrated that the advantage of equation (2.33) over equation (2.32) is

that quite acceptable accuracy for $\Sigma(t)$ might be obtained using orders of magnitude fewer terms (*i.e.,* using $b_{\max} \ll p_{\max}$), and hence dramatically fewer internal state variable arrays needed to store crack descriptors (*i.e.,* evolving lengths and orientations).

2.4.1 Non-uniform (optimized) binning via grid zooming

For various reasons, it might be desired to have high accuracy of the expectation integral in certain zones of state space. For example, since large cracks play the predominant role in both compliance changes and in structural failure, it would be advisable to use an uneven mesh that is zoomed to obtain a fine mesh at the large-crack part of probability space even though the greatest crack densities correspond to smaller cracks. As illustrated in Fig. 2.3, the space itself is not distorted – just the mesh laid on it. Unlike what is done in importance sampling (*cf.* [72]), which uses selective sampling to *minimize* the discrepancy between $\Sigma[h(\hat{X})]$ and $E[h(\hat{X})]$ in equation (2.2), this method seeks to *accurately capture* (not minimize) this discrepancy in order to provide scale-sensitive point-to-point variability in material properties that stimulates (and strongly influences the character of) unstable macroscale phenomena such as localization bands or runaway crack growth. To reduce the number of bins that can approximately capture the finite-sampling error of a large population, this

section defines a nonuniform grid such that each cell contributes equally (on average) to $\Sigma[h(\hat{X})]$. This zooming scheme ultimately produces a higher mesh density in the part of probability space that maps to larger values of $h(\hat{X})$ (*e.g.,* larger crack sizes in applications to damage mechanics). Unlike what is done in importance sampling, sample realizations are not affected by zooming. To avoid confusion with importance sampling, it is emphasized that the "influence" of any given point $\hat{r}$ in probability space is determined by its relative contribution to $\Sigma[h(\hat{X})]$. Therefore higher mesh density will be required in regions of higher influence where $h(\hat{X}) = h(G(\hat{r}))$ is large. The appropriate mesh density will be ultimately given by the reciprocal of the Jacobian of the zooming function to be derived below.

To identify a zooming formula, a helper "s" space is discretized into *evenly spaced* node locations $\{s_1, s_2, \ldots, s_{i_{\max}}\}$ in the range from 0 to 1. Then these node locations are transformed to *unevenly spaced* (zoomed) node locations on a reference r grid by a transformation function $r(s)$. For example, $r = \sqrt{s}$ would produce finer grid density near $r = 1.0$. The *ideal* zooming function, $r(s)$ that would produce *terms of equal magnitude*, on average, in the discrete summation that evaluates the expected value of $h(\hat{x})$ is derived here. The case study for this analysis will use $h(\hat{x}) = x_1^2 = \ell^2$, corresponding to the function that appears when evaluating the expected value of compliance in 2D microcrack models. In that context, it is the random variable r_1 that maps to crack length ℓ. To keep the ensuing formulas simple, the symbol r in this section stands for r_1.

The zooming function $r(s)$ for which terms in a discrete approximation of $\Sigma[h(x)]$ are of equal magnitude, *on average.* is determined here For a continuous distribution, this expectation is

$$E[h[x]] = \int_{-\infty}^{\infty} h[x]\, p(x)\, \mathrm{d}x = \int_{0}^{1} h[g[r]]\mathrm{d}r = \int_{0}^{1} h[g[r(s)]]\, \frac{dr(s)}{ds}\, \mathrm{d}s\,. \tag{2.34}$$

Thus, to achieve (on average) equal contributions from each bin to the evaluation of $E[h(x)]$, the zooming function $r(s)$ should be defined such that the final integral listed above has a constant integrand. This condition gives a first-order ODE,

$$h[g[r]]\frac{dr}{ds} = c \quad \text{subject to} \quad r(s) = 0 \;\; \text{and} \;\; r(s) = 1\,, \tag{2.35}$$

where c is an undetermined constant (justifying two solution constraints even though the ODE is first order). For the case that $h(x) = x^2$, the solution is

$$s = \frac{1}{2}\left[2r + (r-1)\ln^2(1-r) - 2(r-1)\ln(1-r)\right]\,. \tag{2.36}$$

This function, plotted in Fig. 2.3, is solved numerically for r to give the zoom function $r(s)$. Recalling that r represents the first random variable r_1, this simple zooming scheme increases the mesh density with increasing values of r_1 and keeps a uniform density with respect to r_2, thereby producing high-aspect-ratio (elongated) cells in the nonuniform grid of Fig. 2.3. The corresponding mesh anisotropy is easily accom-

modated in this simple example via an uneven rectilinear grid. More complicated influence metrics (as well optimization of this strategy to zoom the mesh toward point clusters) might lead to target mesh densities that cannot be achieved with a rectilinear grid. Fortunately, the general framework of the binning scheme has no intrinsic requirement for the grid shape functions to be defined on a rectilinear (or even structured) grid. Any other influence weighting scheme can be accommodated in this binning framework by simply replacing the rectilinear reference grid with an appropriate anisotropic Delaunay tesselation (*cf.* [83]) in which standard tetrahedral shape functions can readily serve as alternatives to the rectilinear shape functions that have been used here for clarity.

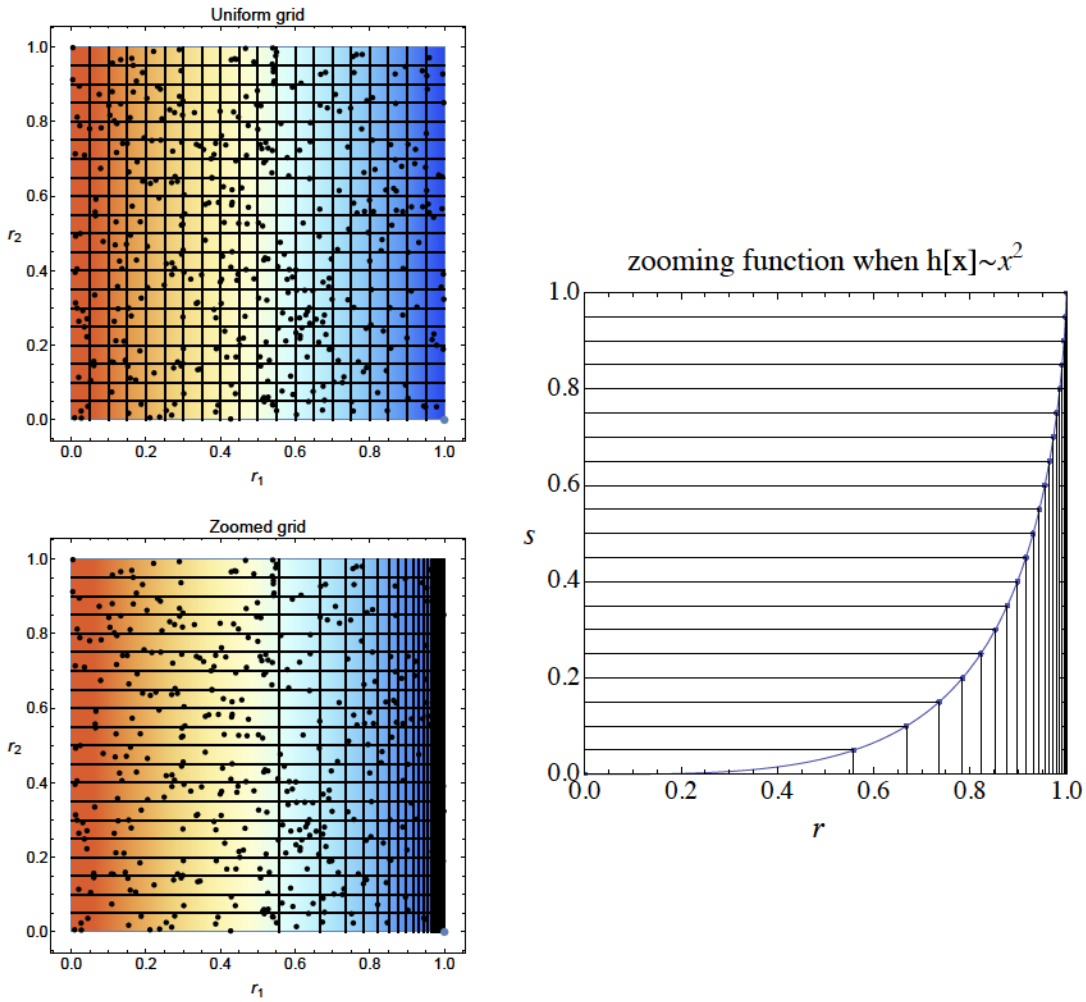

Figure 2.3: Uniform and zoomed tesselations of $\hat{r}$ reference space. Neither the field of interest (color map) nor Poisson point locations (dots) change with grid zooming. The grid nodal weights become more variable in the zoomed region, making that region more representative of the original discrete set of realizations and hence making integrals over that region more representative of the desired results.

2.5 1D Numerical Examples

This section provides 1D numerical examples to illustrate the binning calculations and convergence properties.

2.5.1 Simple numerical debugging example

This example uses a small number of points and grid cells to illustrate steps of the initialization phase. The primary goal is to compute modified Gauss-point weights (also called bin occupancies W_b) and Gauss-point locations (which are the bin centers X_b if the corresponding occupancy is found to be nonzero). Much of the analysis is performed in the reference ($\hat{r}$) space. Final results for bin centers are in the state ($\hat{X}$) space. To illustrate the calculation steps, the state space describes an exponentially distributed random variable with a mean of 1. The reference space is taken to have $p_{\max} = 5$ random realization points $\{r_{p1}, \ldots, r_{p5}\}$, the values of which would be normally generated as uniform pseudo–random numbers from 0 to 1, but which are listed as the first line of table 2.1 to facilitate debugging. That is, once an implementation matches our stated values for each intermediate step in the algorithm, the algorithm should then replace the 5 fixed r_p values with a much larger $p_{\max}$ population of r_p values that are uniformly random on $[0, 1)$. Alternatively, the scheme should import measured descriptors (*e.g.,* from X-ray computed tomography). Keep in mind that the binning scheme is designed for extremely large values of $p_{\max}$,

but a very small value of $p_{\max}$ is used in this section in order to provide a useful debugging example. Using equation (2.17a) with $\bar{\ell}_0 = 1$, the five points in reference r-space map to five realizations $\{X_{p1}, \ldots, X_{p5}\}$ in the state X-space. For simple debugging, probability r-space is discretized into two equal-sized grid cells (and thus the 3 evenly spaced node locations listed in table 2.1). This example uses 2 Gauss points per cell, so it finds the $N_{\text{gauss}} = 4$ bin occupancies (PDF-scaled Gauss weights) and 4 Gauss-point locations in initial state (not reference) space, which are the boxed results in table 2.1.

Steps required to compute the outputs are detailed in Algorithm 1, where each intermediate term is evaluated to provide clarity to assist with code debugging. The boxed equation in the algorithm shows a direct (more efficient) formula for finding the bin occupancies, which follows merely by simplifying the step-by-step calculations. Once the code passes this simple verification test, it should then be tested for a variety of population sizes and realizations, as explained in the remainder of this section.

Algorithm 1 Steps to evaluate W_g bin occupancies in the example of table 2.1

1: Set problem data [See "inputs" in table 2.1]
2: Set $p_{\max}$=length of $\{r_p\}$ array $= 5$.
3: Set $i_{\max}$=length of $\{r_i\}$ array $= 3$. The number of cells is then $i_{\max} - 1 = 2$.
4: Assign to each cell the list of points contained within that cell.
▷ In table 2.1, cell 1 contains points 1 through 3, while cell 2 contains points 4 and 5.
5: Initialize node volumes and node counts to zero: $V_i = 0$ and $N_i = 0$ for $i = 1, \ldots, i_{\max}$. Set integer e=0;
6: **while** $++e < i_{\max}$ **do** ▷ Begin loop over cell ID $e = 1 \ldots 2$
7: Find the cell's two global node IDs, i_1 and i_2.
8: Set a and b to the (reference) nodal coordinates on the cell and set $L = b - a$ as the cell length.
9: Applying equation (2.25) for the case of linear shape functions on the cell,
10: accumulate contributions of the cell to the nodal volume:
11: $V_{i_1} = V_{i_1} + L/2$ and $V_{i_2} = V_{i_1} + L/2$ (where i_1 and i_2 are nodal IDs on the cell)
12: Accumulate contributions to N_i from this cell as follows:
13: **for** each point at location r_p within the cell **do**
14: evaluate the two cell shape functions at the point: $S_1 = \frac{r_p - b}{a - b}$ and $S_2 = \frac{r_p - a}{b - a}$.
15: Accumulate contributions of the point to the nodal point count:
16: $N_{i_1} = N_{i_1} + S_1$ and $N_{i_2} = N_{i_2} + S_2$.
17: **end for**
18: **end while**
19: Loop over nodes and set nodal weights: $w_i = N_i / p_{\max}$
20: **while** $++e < i_{\max}$ **do** ▷ Begin loop over cell ID $e = 1 \ldots 2$
21: Set cell node locations a and b as before.
22: For the choice of 2 Gauss points per cell, set the standard Gauss weights as $\{\gamma_1, \gamma_2\} = \{1, 1\}$
23: and logical Gauss locations $\{\xi_1, \xi_2\} = \{\frac{-1}{\sqrt{3}}, \frac{+1}{\sqrt{3}}\}$.
24: Revise each standard Gauss weight, γ_g, to obtain the scaled weight: $k_g = \gamma_g * (b - a)/2$
25: ▷ This is the factor appearing in equation (2.30).
26: Evaluate the shape functions at each Gauss point in the cell
27: ▷ Check values against S_i pairs in table 2.1
28: For each node i and Gauss point g in the cell, evaluate $\Delta_i(r_g) = S_i(r_g)/V_i$
29: ▷ Check values against Δ_i pairs in table 2.1
30: For the g^{th} Gauss point on a 2-node linear cell, evaluate
31: $q(r_g) = w_1 \Delta_1(r_g) + w_2 \Delta_2(r_g)$ ▷ Check each term against "density pairs" in table 2.1.
32: where the subscripts '1' and '2' refer the the nodes of the cell
33:
34: Use k_g (from line 24) to evaluate occupancies $W_g = k_g q(r_g) = \boxed{\frac{\gamma_g}{2}\left(w_1 \frac{b - r_g}{V_1} + w_2 \frac{r_g - a}{V_2}\right)}$
35: where γ_g is the g^{th} standard Gauss weight (computed above in line 22).
36: ▷ See equation (2.30), and check against table 2.1.
37: **end while**
38: Apply an appropriate mapping function to convert each reference Gauss point location r_g to the initial descriptor X_g. In table 2.1, the descriptor X (initial crack length) was taken to be exponentially distributed with a mean of 1, thus requiring the transformation in equation (2.17a): $X_g = \ln\left[\frac{1}{1 - r_g}\right]$.
39: ▷ Check these X_g descriptor values against table 2.1.
40: Discard all data except for the nonzero W_g occupancies and associated X_g properties, which are thereafter called "bins" and indexed with "b" instead of "g." (A bin is merely a Gauss point with nonzero occupancy.)
41: If desired, compute expectation summations and errors. For example, the approximate mean of the square of the property is $\overline{X^2} \approx \sum_b W_b X_b^2$, which (to set error) is compared with $\sum_p w_p X_p^2$, in which $w_p = \frac{1}{p_{\max}}$.
42: ▷ See section 2.5.2 for details.
43: If desired, apply a growth model to evolve each initial X_b to become $x_b(t)$ at some later time.
44: ▷ See section 2.7 for an example in crack mechanics.

INPUTS
number of Gauss points per cell = 2
point locations, $r_p = \{0.11, 0.22, 0.37, 0.56, 0.92\}$
zoom exponent = 1 (no zooming and hence equal-sized grid cells)
node locations, $r_i = \{0, 0.5, 1\}$

OUTPUTS (and intermediate results to help with debugging)
Node volumes, $V_i = \{0.25, \quad 0.5, \quad 0.25\}$
Number of points per node, $N_i = \{1.6, \quad 2.44, \quad 0.96\}$
Node weights, $w_i = \{0.32, \quad 0.488, \quad 0.192\}$
Gauss-point locations, $r_g = \{0.105662, \quad 0.394338, \quad 0.605662, \quad 0.894338\}$
Standard Gauss weights on range $[-1, 1] = [K_1, K_2] = \{1, 1\}$
Scaled standard Gauss weights: $k_g = \frac{len_{\text{cell}}}{len_{\text{gauss}}} K_g = \{0.25, 0.25, 0.25, 0.25\}$
Shape functions at Gauss points: $S_i(r_g) =$
$\{(0.788675, 0.211325), (0.211325, 0.788675), (0.788675, 0.211325), (0.211325, 0.788675)\}$
Delta-pulse function evaluated at the Gauss points$=\Delta_i(r_g)$
$= \{(3.1547, 0.42265), (0.845299, 1.57735), (1.57735, 0.845299), (0.42265, 3.1547)\}$
Density pairs = terms that sum to give Gauss-point density $q(r_g)$
$= \{(1.0095, 0.206253), (0.270496, 0.769747), (0.769747, 0.162297), (0.206253, 0.605703)\}$
Sum these pairs: $q(r_g) = \{1.21576, \quad 1.04024, \quad 0.932044, \quad 0.811956\}$
Multiply these by the k_g values to obtain the W_g occupancies.

Alternatively, if intermediate results (like k_g) are not sought, the bin occupancies may be found by directly applying the boxed equation in Algorithm 1.
Either method should give the following W_b occupancies:

Bin occupancies: $\boxed{W_b = \{0.303939, \quad 0.260061, \quad 0.233011, \quad 0.202989\}}$
Bin descriptor properties = Gauss-point locations in state space:
$\boxed{X_b = \{0.111672, \quad 0.501432, \quad 0.930548, \quad 2.24751\}}$

CDF plot: this is the green line in the first (upper-left) graph of figure 2.4, which (as seen) jumps up at each X_b by the occupancy W_b. This green (binned) CDF is to be compared with the black CDF in the same plot, which jumps by equal 1/5 weights at each
$X_p = \{0.116534, \quad 0.248461, \quad 0.462035, \quad 0.820981, \quad 2.52573\}$,
which are defined by applying equation (2.17a) to the original r_p population.

Table 2.1: Uniform (nonzoomed) two-cell numerical example (designed to facilitate debugging implementations of Algorithm 1). Only the boxed outputs are retained. Here, 5 points were reduced to 4 bins, but even millions of points would reduce to 4 bins on this 2-cell-by-2-Gauss-point grid. Hence, grid refinement rigorously controls the balance of computational accuracy and expense.

2.5.2 Expectation integral (1D example)

This example explores the degree to which binning can provide an acceptably accurate evaluation of the mean of the square of the exponentially distributed random variable: $h(x) = x^2$. The goal is to approximate the mean of the squares, $\overline{x^2}$, of the *discrete population*, not the expected value $E[x^2]$ found from the original exponential distribution. Before evaluating this mean of squares, it is instructive to first visualize the degree to which the approximate binned CDF tracks the discrete CDF for different seeds.

Consider a single random variable x, with an exponential PDF $p(x) = e^{-x}$. The corresponding CDF, given by $1 - e^{-x}$, is shown as a thick gray line in figure 2.4. The black lines in that figure are the discrete CDFs corresponding to a $p_{\max} = 5$ population sample (matching that in Table 2.1 to facilitate debugging of CDF visualizations). The same plots for a $p_{\max} = 100$ sample are shown in figure 2.5. Figure 2.4 compares the discrete CDF (black) from equation (2.32) with the CDF (red or green) of the bin approximation in equation (2.33). The binned CDF is shown in red if the number of bins is larger than the actual number of discrete points in the exact realization (in which case, there is no benefit to using bins); otherwise, when binning is beneficial, the binned CDF is shown in green. The black (Npt) plot jumps by an amount $1/p_{\max}$ at each of the $p_{\max} = 5$ realizations. The colored (Nbin) plot jumps at each bin location by an amount equal to the bin occupancy, W_g in equation (2.30). The left column of figure 2.4 shows equal-sized cells in r probability space, while the right

column uses zooming based on equal contributions of each bin, on average, to overall damage. As seen, zooming better resolves the "influential" regions of the CDF where x is large.

The goal is for the colored (Nbin) plot to approximately match the black (Npt) plot. As more grid cells are used in reference space (bottom row), the binned line approaches the exact discrete (black) line, as it should; for the small value of $p_{\max}$ in figure 2.4, the binned solution under grid refinement appears in red because $b_{\max} > p_{\max}$. Because convergence eventually requires more bins than points, a binning scheme is not needed whenever there are fewer actual discrete realization points than bins. On the other extreme, a binning scheme is worthwhile in the case that there are are large numbers of points. Accordingly, for the larger number of bins in figure 2.5, the binned solution is shown in green (indicating $b_{\max} < p_{\max}$) even under grid refinement. As seen in that figure, zooming (using $h(x) = x^2$) accurately tracks with visible perturbations in the black (actual, discrete) CDF in the influential region of large values of x, and it will be shown that this influence-based zooming provides a far more accurate approximation to equation (2.1) despite the visible errors in the CDF at low values of x.

The relative error in evaluating the mean of x^2 (important for finding crack compliances) is illustrated in figure 2.6. The fact that the error decreases with the number of cells verifies the assertion that $q(r) \to \mathscr{P}^*(r)$ as the grid is refined. The second row in figure 2.6 shows that the error for a fixed number of cells is fairly insensitive

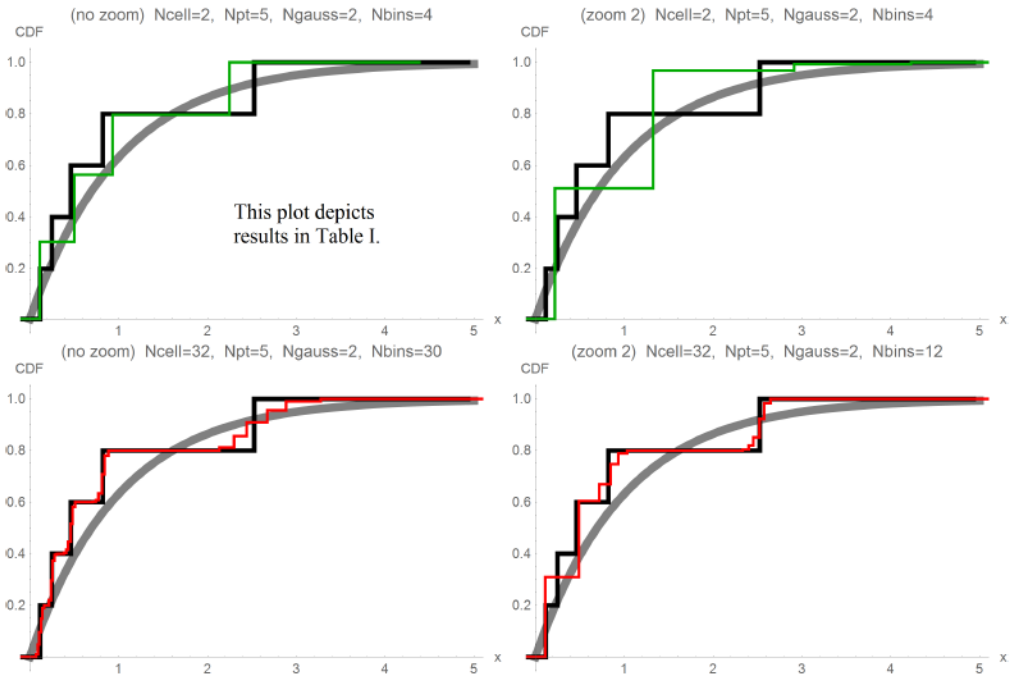

Figure 2.4: Comparisons of a source nominal CDF (gray), a $p_{\max}$=5 realization (black plot with 5 equal-sized jumps), and a binned approximation (in red if $b_{\max} \geq p_{\max}$ or green if $b_{\max} < p_{\max}$). The bottom row uses more grid cells (hence shown in red, as binning isn't worthwhile for this small, $p_{\max}$=5, population). The right column uses zooming to better resolve the CDF at large x values.

to the number of realization points ($p_{\max}$), which is evidence that the approximate discrete CDF from equation (2.33) tracks consistently with the realization CDF from equation (2.32) (as was already seen by the black and binned lines tracking together in Figures 2.4 and 2.5). Overall, the accuracy in the evaluation of discrete averages is determined predominantly from the number of grid cells used in the initial discretization of probability space. As seen by comparing the first column in figure 2.6 with the second column, it is clear that error can be dramatically reduced by using mesh refinement; in that case, the mesh in the right-hand column was zoomed to better discretize the large-x (large crack) portion of the CDF in order each bin to provide

(on average) equal contributions to the expectation summation of x^2.

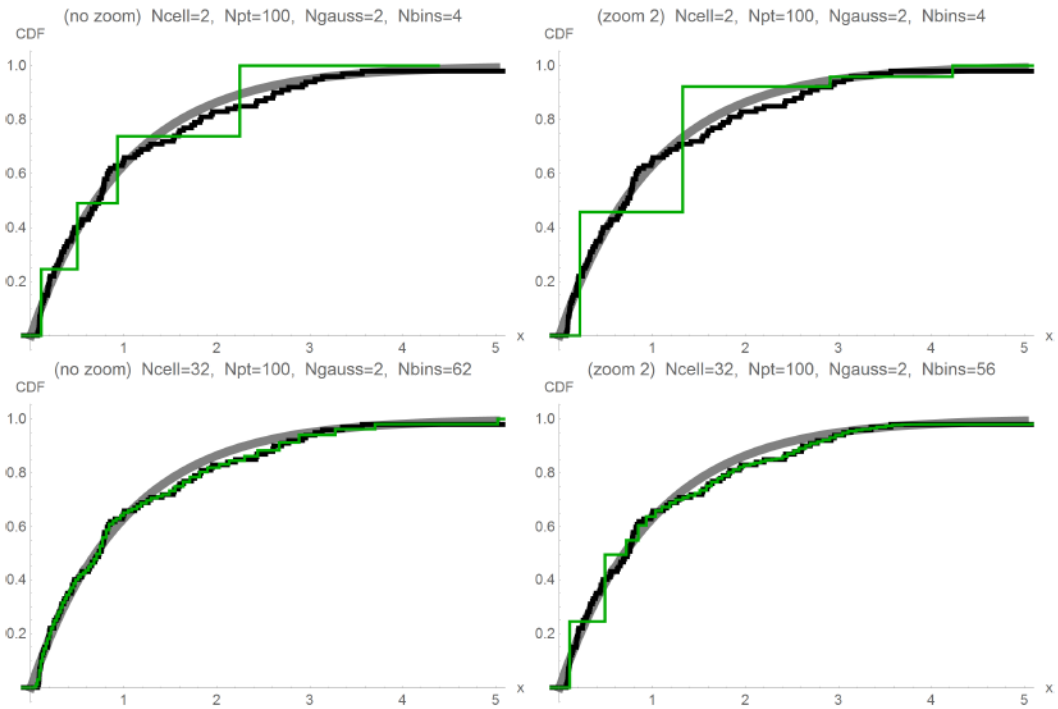

Figure 2.5: These plots are identical to those in figure 2.4 except using 100 Poisson realization points, which makes the discrete (black) CDF a much closer approximation to the source CDF (gray). In this case of a larger number of points (`Npt`=$p_{\max}$ =100) in comparison to figure 2.4 (where `Npt`=5), the binning scheme is consistently advantageous (`Nbin`<`Npt`). As before, zooming provides better resolution of the influential large-x zone. Note in particular that $b_{\max}$ might be smaller than the total number of Gauss points, given by $g_{\max} = c_{\max} N_{\text{gauss}}$, where $c_{\max}$ = `Ncell` is the number of cells.

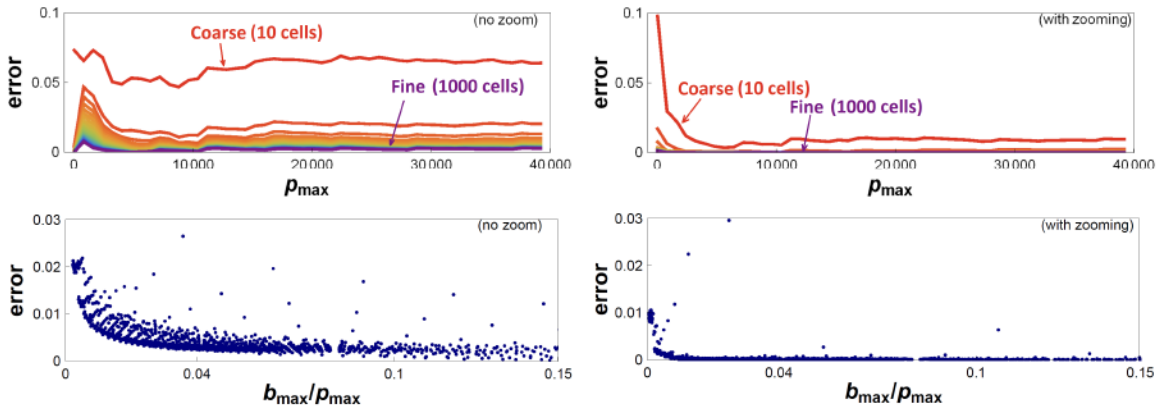

Figure 2.6: Relative error in the average of x^2, defined as $\bar{h}^{\text{binned}}/\bar{h} - 1$, where $\bar{h}$ is the *exact* average in equation (2.32) using $h[x] = x^2$, and $\bar{h}^{\text{binned}}$ is the binned approximation defined in equation (2.33). Plots in the left column use a uniform grid in r-probability space, while those in the right column use grid zooming to obtain, on average, equal contributions of each grid cell to the average of x^2. Top row: convergence with grid refinement, with no significant sensitivity to the value of $p_{\max}$. Bottom row: evidence that errors are typically less than 2% if using 15% as many bins as points (*i.e.,* an 85% computational cost reduction if this error is acceptable – and many orders of magnitude in cost reduction in the important case that $p_{\max}$ is extremely large). Each test used 2 Gauss points per cell.

2.6 2D Numerical Examples

This section provides a 2D numerical example to illustrate the binning technique and associated convergence of the joint CDF shown in figure 2.7. This is an extension of the example provided in section 2.5 with two random variables. Specifically, we estimate the Gauss-point locations and weights using two variables in the reference ($\hat{r}$) space or in state ($\hat{x}$) space. The two random variables ($\hat{r} = [r_1 \quad r_2]$) in reference space are assumed to correspond to crack length and orientation, which is defined in state space as in equation (2.4). The convergence in the CDF will be demonstrated along two sections for either fixed angles or fixed lengths (shown as straight red lines

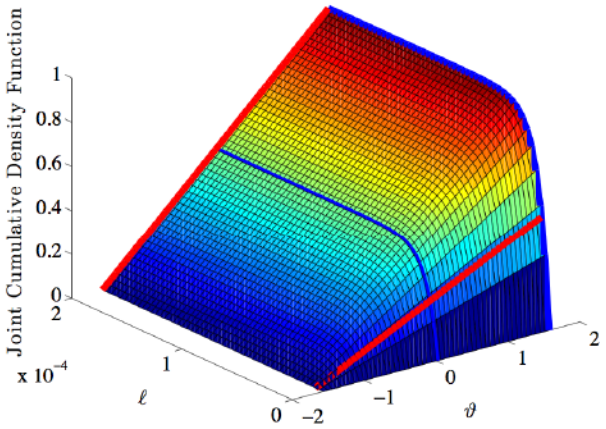

Figure 2.7: The joint cumulative density function (CDF) for both crack length and orientation. Crack length ℓ is exponentially distributed and crack orientation ϑ is uniformly distributed. It is assumed that crack length and orientation are independent, so that the joint CDF is obtained by multiplying the univariate CDF describing crack length by the univariate CDF describing crack orientation. Two blue lines are representing two particular section of joint CDF surface with fixed angle 0^o and 90^o respectively. The two straight red lines are two sections of the surface with varying angle but fixed length of magnitude 6.93 µm and 200 µm respectively.

for fixed angle and as curved blue lines for fixed length in figure 2.7). For the 2D case, the expectation summation involves two random variables r_1 and r_2. The first variable is described by an exponential probability density function (PDF) with mean 10 µm and the In order to verify the results of the 2D model, two sets of randomly generated samples of crack length and orientation (one with $p_{\max}$ =20 and the other with $p_{\max}$ =10000) are used to calculate a discrete bivariate CDF. Because the step functions in a discrete bivariate CDF are difficult to discern visually on a surface plot, in figure 2.8 we plot the values of the CDF as a function of ℓ along specific values of ϑ (shown by the blue lines in figure 2.7). In these plots, the values of the continuous CDF are plotted in gray, while the values of discrete bivariate CDF corresponding to

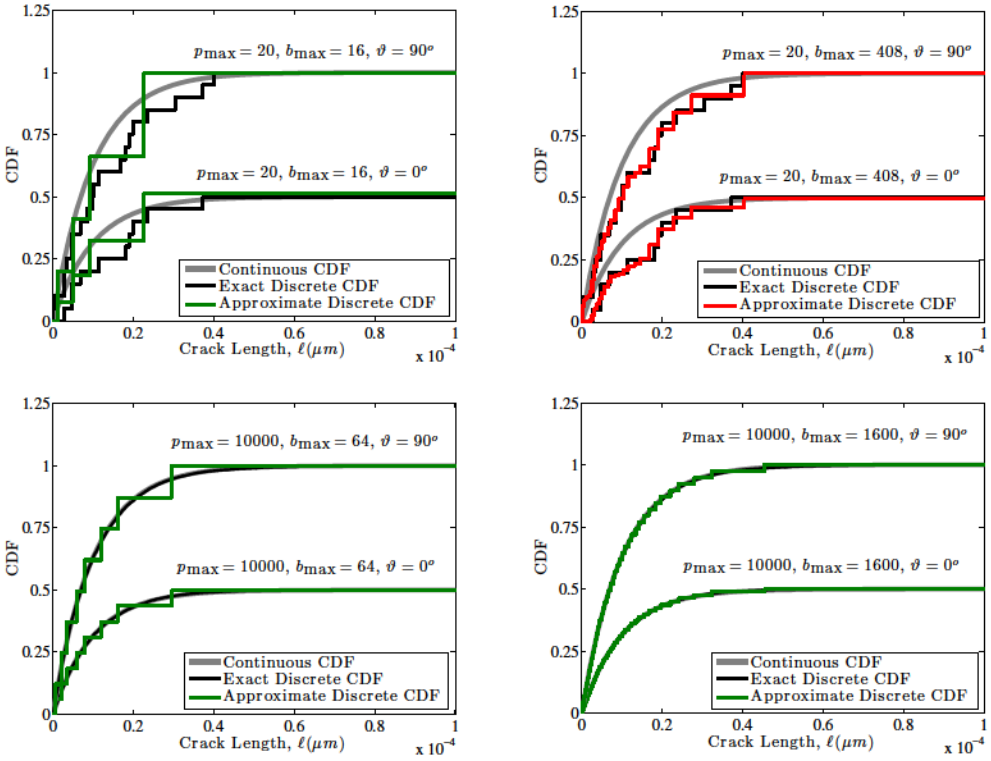

Figure 2.8: Comparisons of a source nominal continuous CDF (gray), the discrete CDF based on the actual p_{max} realizations (black) and the (red or green) binned approximation to the discrete CDF based on b_{max} bins for the 2D case for two fixed angles (0^o and 90^o) which represents lines $r_2 = 0.5$ and $r_2 = 1$ in the reference space (see figure 2.7). The line $r_2 = 1$ which corresponds to $\vartheta = 90^o$ are used to include all possible crack orientations ranging between $-\pi/2$ to $\pi/2$. The number of points p_{max} increases from the top plots to the bottom plots while the number of bins b_{max} in the probability space increases from the left column to the right column.

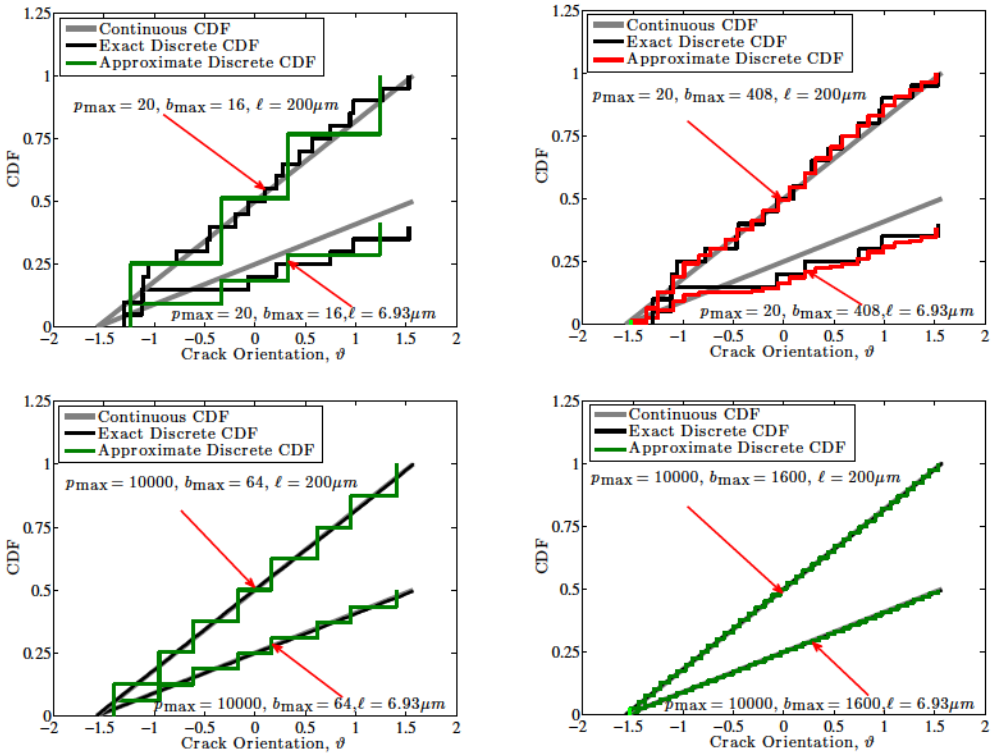

Figure 2.9: Comparisons of a source nominal continuous CDF (gray), the discrete CDF based on the actual $p_{\max}$ realizations (black) and the binned approximation to the discrete CDF based on $b_{\max}$ bins (green or red) for the 2D case for two fixed crack lengths. The two sets of plots in each figure compare these CDFs of crack orientation for crack lengths of 6.9 µm and 200 µm (shown as a the red lines in the two-dimensional CDF in figure 2.7). The number of points $p_{\max}$ increases from the top plots to the bottom plots while the number of bins $b_{\max}$ in the probability space increases from the left column to the right column. These two crack lengths correspond to lines $r_1 = 0.5$ and $r_1 = 1$ in probability space. Since maximum realized crack length is 200 µm, the line $r_1 = 1$ in probability space represents all of the cracks.

the randomly generated sample of $p_{\max}$ values are plotted in black and approximate discrete bivariate CDF based on the Gauss weights are plotted in green and red (red is used if $p_{\max} < b_{\max}$, otherwise green is used). As expected, an increased number of sampling points $p_{\max}$ provides a closer match between the continuous CDF and the discrete sample CDF. It is not our goal to match the continuous CDF, however, but rather to define a binning scheme that is able to capture accurately the discrete sample CDF. In figure 2.8 the green and red curves show the Gauss-point approximation to the discrete sample CDF for different grid cell sizes. As the number of cells (and therefore the number of representative bins $b_{\max}$) increases, the error between the discrete sample CDF and the Gauss-point approximation decreases. We note that for a crack population of $p_{\max}$ =20, it would not make sense to use 408 bins; however, this small number of sample points is included here since it helps to visualize the convergence of the Gauss-point approximation to the actual discrete sample CDF. figure 2.9 shows the CDF as a function of ϑ along specific values of ℓ (shown by the red lines in figure 2.7). The results are very similar to those in figure 2.8, in that we see convergence between the Gauss-point approximation and the discrete sample CDF as the number of cells in probability space increases (increasing the number of bins $b_{\max}$).

2.7 Comparison of Different Binning Schemes

In this section, three binning schemes are applied to a 2D micromechanics model that provides a uniaxial stress vs. strain relationship in brittle materials under high-rate loading [23]. In that model, the time dependent evolution of crack lengths and associated global stress under a constant strain rate is estimated using an explicit finite difference scheme in time. At each time step, the growth rate for each crack (or each bin of cracks) is calculated based on the mode-I stress intensity factor K_I at the crack tip:

$$\dot{\ell} = \frac{C_R}{\alpha}\left(\frac{K_I - K_{Ic}}{K_I - K_{Ic}/2}\right)^{\gamma}. \tag{2.37}$$

Here, $\dot{\ell}$ is crack growth rate, K_{Ic} is the material mode-I fracture toughness, C_R is the Rayleigh wave speed, and α and γ are fitting parameters. The mode-I stress intensity factor K_I is a function of the local stress state around the individual crack, which is estimated using a self-consistent scheme that assumes an elastic elliptical inclusion in a damaged matrix, using the damage and the stress computed at the previous time step. The compliance relates to the instantaneous crack length according to the following equations: (for details see [23])

$$S_{1111} = \frac{1}{\bar{E}_1(\Omega)},\ S_{2222} = \frac{1}{\bar{E}_2(\Omega)},\ S_{1122} = -\frac{\nu_{21}}{\bar{E}_2(\Omega)},\ S_{2211} = -\frac{\nu_{12}}{\bar{E}_1(\Omega)},\ S_{1212} = \frac{1}{4\bar{G}_{12}(\Omega)}, \tag{2.38}$$

$$\Omega = \frac{1}{N}\sum_{p=1}^{N} \eta \ell_p^2. \tag{2.39}$$

In equation (2.38), $\bar{E}_1$ and $\bar{E}_2$ are the effective Young's modulus in 1 and 2 direction. ν_{21} and ν_{12} are Poisson's ratio, and $\bar{G_{12}}$ is the shear modulus. In equation (2.39), N is total number of cracks, and η is the average flaw density per square meter. Based on this updated compliance the global stress at the current time step is updated and used as input to the following time step. The key equation here is equation (2.39), which is in a form consistent with equation (2.1). If the continuous source distribution is used in the micromechanics model with a very fine binning the damage can be expressed by the following equation instead of equation (2.39):

$$\Omega = \eta \sum_{p=1}^{N} g(\ell_p) \Delta \ell_p \ell_p^2 . \tag{2.40}$$

In equation (2.40), $g(\ell_p)$ is the probability density function of ℓ. Using this form, one could view binning as the way in which the probability density function is divided into N lumped values of $g(\ell_p)\Delta\ell_p$ in ℓ-space. This approach does not account for discrete sampling that would lead to variations in the population, which is addressed explicitly in the binning approaches based on equation (2.39). A very fine binning scheme will provide an accurate solution, but it is computationally inefficient. Therefore, different binning schemes are studied in this section to consider the balance between efficiency and accuracy of the binning scheme.

2.7.1 Infinite sampling of cracks

With a finite number of sample crack lengths, there is variability and error that arises from two sources: variations due to the limited number of samples $p_{\max}$ and error due to the binning approximation. In order to isolate the effects of binning errors, we first assume that $p_{\max}$ approaches infinity, which leads to a sampled discrete CDF that is equivalent to the continuous CDF describing crack length. For this micromechanics study, we assume that the crack lengths are exponentially distributed random variables with a mean value of 10 µm. As a basis for comparison, this infinite crack population is binned very finely in state space, with 10^5 bins. Smaller numbers of bins are established using three possible approaches to binning: 1) binned into equal increments of crack length for each bin $\Delta\ell$; 2) binned into equal increments in reference probability space (i.e., equal expected numbers of cracks in each bin); and 3) "zoomed" bins in which each bin on average contributes equally to the total damage in the material. Each of these three binning approaches is illustrated in figure 2.10 along with the stress-strain response for each individual scheme. The "zoomed" bins match the exact solution most accurately, followed by the equal-increment binning in probability space.

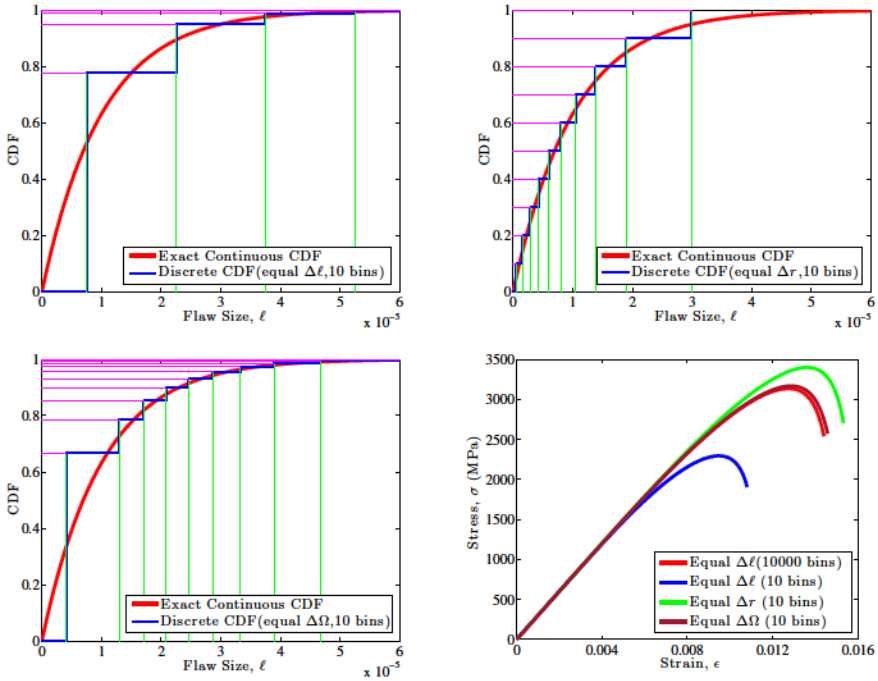

Figure 2.10: The first three plots show the CDF *vs.* initial crack size, with red and blue respectively being the continuous and binned (discrete) CDFs. The vertical green lines are bin locations (spacings of which suggest bin densities), and the horizontal pink lines indicate the probability increment for the bins (spacing of which depicts reference space zooming). In the top row, the first plot uses equal state-space (crack-length) increments $\Delta\ell$, while the second one uses equal probability-space increments Δr. The lower-left plot has bins zoomed to give equal damage increments $\Delta\Omega$ in each bin on average, where Ω is given in equation (2.3). The lower-right plot compares stress-strain responses (predicted by the micromechanics model) for these binning schemes.

2.7.2 Finite sampling of cracks

In the previous example, an infinite number of sample crack lengths was used so that binning was based on the continuous source PDF for the initial crack population. Now the same analysis is applied with a large but finite number of 10^4 cracks. The first step is direct calculation of the stress-strain response using 10^4 bins, each of which represents a single crack and has an associated probability of $1/p_{\max}$. Each

bin has a finite crack population which is a single crack whereas the crack population is considered to be infinite within each of the 10^5 bins in the previous case. The same three binning schemes are then applied for this crack population, varying the number of bins, with the results shown in figure 2.11. The stress-strain prediction using 10 bins based on equal damage increments clearly agrees best with the 10^4 crack population, demonstrating superiority of the equal-damage binning scheme.

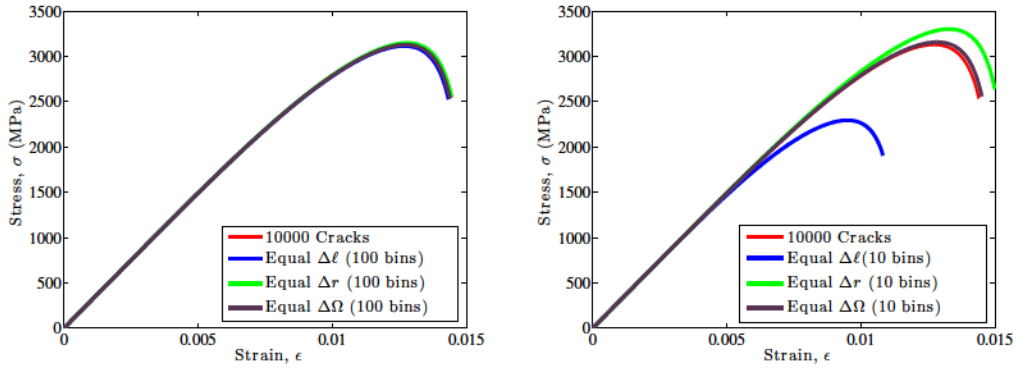

Figure 2.11: Stress-strain plot from micromechanics model for an actual solution predicted by an array of 10^4 discrete cracks. These discrete cracks are binned as per the methodology described in section 2.4.

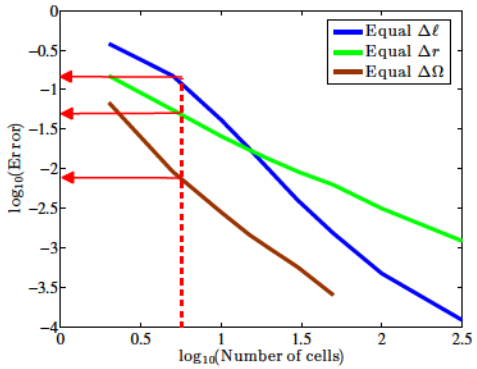

Figure 2.12: Error in peak stress with increasing number of cells in reference space, based on a crack population of 10^4 cracks. Using bins with equal initial damage leads to significantly less error and a faster rate of convergence than binning equally in state space or binning equally in probability space.

Figure 2.12 plots the error, defined as

$$\text{Error} = \frac{\sigma_{\text{approx}}}{\sigma_{\text{actual}}} - 1\,. \tag{2.41}$$

where σ_{approx} is the peak stress predicted from the binned solution and σ_{actual} is the peak stress predicted from the solution based directly on the 10^4 crack population. The error from all three binning schemes converges to zero as the number of bins increases, but the zoomed bins based on equal $\Delta\Omega$ provide a much lower magnitude of error and a faster rate of convergence than the other binning schemes. The three red arrows indicate the error associated with 10 bins, for each of the 3 different binning schemes, which are approximately 14%, 4% and 0.8% for equal $\Delta\ell$, equal Δr and equal $\Delta\Omega$, respectively. In other words, peak stresses predicted from the "zoomed" equal damage binning are over an order of magnitude more accurate than the other binning schemes. Next, the crack sample size p_{max} is taken to be 100. With only 100 cracks, there is notable variability in the stress-strain curve from one sample population to the next. In figure 2.13 stress vs. strain for three different sample populations are provided, both for the solution based on explicit tracking of every crack and from the three different binning schemes using 10 bins. Again, binning the crack population by equal contributions to damage provides results that are far superior to the other binning schemes. Furthermore, this binning approach is able to capture variability from sample to sample. The fourth plot in figure 2.13 shows how

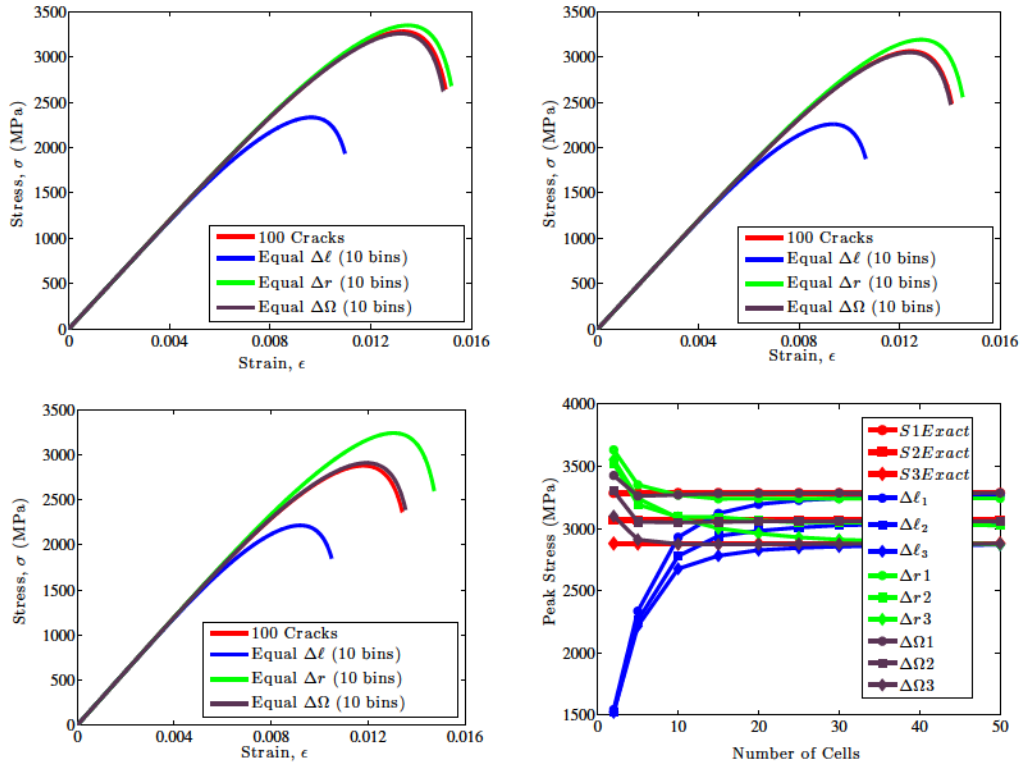

Figure 2.13: Stress-strain plots based on 3 different realizations of the population of 100 cracks, showing variations in predicted peak stress associated with sampling variability. Equal-damage binning consistently provides the most accurate prediction. The lower-right plot shows that all three binning schemes converge to the exact result with a sufficient number of bins, with the equal-damage binning converging fastest. Note: the number of bins is twice the number of cells.

the results converge with the number of cells in probability space.

2.8 Binning Scheme for Evolving Crack Population

The binning scheme discussed before is applied to the initial flaw population, assuming that all cracks remain in the same bins throughout the analysis. In reality,

however, the secondary cracks evolve and some of the merge to form bigger cracks. This crack coalescence process replaces some fraction of original cracks from the initial population by new coalesced crack families. In the context of a binned crack population, cracks may move from one bin to another due to growth and coalescence of cracks. The efficient binning methodology has been extended in this section to account for the evolving crack population. Note that more details on crack coalescence is given in the chapter that follows.

The phenomenon of crack coalescence represents a discontinuous evolution of the crack descriptors in which, for example, two distinct cracks are replaced by a single effective crack. Thus, coalescence may be modeled by a sink that removes two cracks from the population, together with a source that simultaneously gives birth to a single new crack having different descriptor values, which is determined from a presumably available coalescence theory that is part of the overall growth model. The proposed scheme for efficiently modeling this large-population evolution theory begins by lumping the initial population into a representative set of bins, with the size of each bin (called occupancy) summing to equal 100% of the initial population size. Then, the growth model is applied to the binned population to predict changes (including crack coalescence) in the population at the end of a computational time step, thus concluding the "Lagrangian" phase of the calculation. These updated descriptors are mapped to a unit reference space (not necessarily probability space), on which a grid is laid down in order to map the transformed updated descriptors to the

nearest Gauss points. These Gauss points are then mapped back to descriptor space to define the updated representative population at the end of the step. The mapping used to establish the reference unit domain, as well as the grid laid down on this space may be arbitrarily selected, retained, or discarded in subsequent time steps. In this sense, the proposal for evolving large random populations is analogous to the Material Point Method updated Lagrangian scheme that is used to solve boundary-value problems in large-deformation mechanics.

The method developed in [39] for binning the initial crack population is herein extended to model evolving crack populations *that might include sources and sinks*, which is a significant complication because it implies that the size of the population can fluctuate as a result of the "death" of two or more cracks when they coalesce to give "birth" to a new combined crack. The newly formed crack generally will not have descriptor values that coincide with any existing bin (or Gauss point). This section therefore outlines how to distribute the descriptors and occupancy of the newly formed crack to the nearest existing cracks.

The previous binning model recognized that descriptor (state) space, which is defined by the domain of all possible crack sizes and orientations is infinitely large. Each crack's initial pair of crack descriptors, denoted $\hat{X} = \{\ell_0, \vartheta_0\}$, was generated in the previous method by sampling from a known continuous probability density function (PDF), denoted by $p_0(\hat{X})$. Such sampling was performed in that work by first generating a uniformly random number $\hat{r} = \{r_1, r_2\}$ on the unit square, and then

an appropriate mapping function was identified,

$$\hat{X} = G(\hat{r}) \ , \tag{2.42}$$

that could transform a *uniformly random* set of samples, $\{\hat{r}_p : p = 1, \ldots, p_{\max}\}$, on the unit square to give the corresponding $\hat{X}_p$ realizations in the semi-infinite half-space of the nonuniformly distributed crack properties.[3] In this way, a realistic simulated crack population of nonuniformly distributed $\hat{X}$ descriptors (length and orientation realizations) for a total of $p_{\max}$ cracks were, in the previous scheme, generated by simply mapping the same number of $p_{\max}$ uniformly distributed points on the unit square under the transformation in Eq. (2.42). The $\hat{r}_b$ value of each b^{th} bin on the unit square was then converted to a binned crack property $\hat{X}_b$ by applying Eq. (2.42). The corresponding occupancy, W_b, found as part of the binning procedure, was the fraction of the original population of cracks associated with that bin. For a growth model without sources or sinks (*i.e.,* without nucleation or coalescence of cracks), the binned cracks may be evolved directly through time such that their occupancies remain constant. Such a model had been used in the case-study examples of the previous scheme, while this new scheme now describes an alternative method for evolving a flaw population governed by a growth model with sources and sinks where the bin occupancies and locations will be altered with time.

In this method, let $\hat{r}$ denote points in probability space, while an alternative

[3] In one-dimensional applications, the $X = G(r)$ function is merely the inverse of the CDF.

variable is introduced $\hat{R}$ representing reference points in a generally different reference unit square that is not necessarily probability space. Again, let $\mathscr{G}(\hat{R})$ denote any convenient invertible transformation function that maps the reference unit square to the semi-infinite half-space crack descriptors. One of an infinite number of possible mappings is, for example,

$$X_1 = \tan\left(\frac{\pi R_1}{2}\right) \tag{2.43a}$$

$$X_2 = \frac{\pi}{2}\sin\left[\pi(R_2 - \tfrac{1}{2})\right]. \tag{2.43b}$$

Another mapping that fits the simple requirement of transforming a unit square to the semi-infinite half space could be

$$X_1 = \ln(1/R_1) \tag{2.44a}$$

$$X_2 = 4\pi\left(R_2 - \tfrac{1}{2}\right)^3. \tag{2.44b}$$

For R_1 ranging between 0 and 1, either of these mappings will produce X_1 falling between 0 and ∞. Similarly, for R_2 ranging between 0 and 1, either of these mappings gives X_2 falling between $-\pi/2$ and $+\pi/2$. Of course, the $G(\hat{r})$ mapping in Eq. (2.17b) can (with the arguments replaced by R_1 and R_2) also define a suitable $\mathscr{G}(\hat{R})$ mapping.

Consider the situation for which a random sample of flaw descriptors $(X_1, \ldots, X_{p_{\max}})$ is known, but the corresponding PDF is unknown. This situation arises, for example

when flaw realizations are directly observed experimentally (rather than being synthetically generated samples from a known PDF). Another example arises in the case of crack growth models with coalescence. Even though the PDF is unknown, one can always introduce *any* convenient mapping function $\mathscr{G}(\hat{R})$ whose inverse maps the points in descriptor space to the unit square. Then binning can be performed on the reference unit square *even though it isn't probability space.* Once bins in the reference unit square have been identified, they can be transformed back to descriptor (state) space under the same mapping, $\mathscr{G}(\hat{R})$.

Let $p_{\max}$ denote the total number of cracks at the beginning of a load step. Let W_g denote the occupancy of the g^{th} Gauss point at the beginning of the step (of course, bins are the Gauss points with nonzero occupancy, but it helps to refer to all Gauss points because some of them will become active with coalescence and growth). The following steps has been performed to obtain the updated non-empty bin locations and change in occupancy due to growth and coalescence.

- Enforce the crack sink from coalescence which represents the number of cracks at Gauss point g that disappear because of coalescence. Let S_1 and S_2 denote the values of the nodal shape functions at the Gauss point. Then the change in number of cracks at the Gauss point is mapped to the nodes on the cell according to

$$\Delta N_i = \Delta N_i + \Delta N_g S_i \tag{2.45}$$

where i ranges over the nodes on the cell containing the Gauss point.

- Enforce the crack source from coalescence which represents the number of new cracks that form as a result of coalescence. Let S_1 and S_2 denote the values of the nodal shape functions at R. Then distribute this change in crack number to the two nearest nodes according to

$$\Delta N_i = \Delta N_i + \Delta N_g S_i \tag{2.46}$$

- Enforce the sink part of the simple growth rule. This represents the number of cracks at Gauss point g that disappear from that bin because they will grow and hence move away from the bin. Map this change in number to the nearest nodes in the reference space as was done in the preceding steps.

- Enforce the source part of the simple growth rule. Find the values of the shape functions at this new location and distribute the change in crack number to the nearest nodes as was done in the previous steps.

- Once the above steps have been completed for each Gauss point a set of nodal values *in the reference space* for the change in crack number are obtained. Add up the new number of cracks at Gauss points to obtain an update of the $p_{\max}$ value.

2.8.1 1D Numerical Example of Evolving Binning Scheme

The scheme described in the above section is applied in case of a micromechanics damage model where crack length is the only variable for binning. The evolving crack population due to growth of microcracks from flaws is lumped into previously defined finite number of bins. The coalescence of cracks is not considered for the current simulation for simplification. The coalescence in the current micromechanics model of interest initiates after the microcracking starts occurring in the specimen. The goal of this simulation is to check the number of bins required to predict the stress-strain response for exact solution (without binning) when the occupancy of the bins varies due to crack growth. The scheme initiates with a finite number of non-empty bins with zero occupancy. The microcracks (wing crack) starts to grow with an applied strain increment at a given load step. The microcracks length is mapped to the nearest Gauss points in the 1D grid ranging from 0-1. The non-empty Gauss point locations on the grid are then mapped back to the realization space using the appropriate mapping function to serve as the new wing crack length. The updated damage is calculated based on the new wing crack lengths. The micromechanics crack growth model predicts new wing crack length for the current time step based on damage variable obtained from the crack lengths in the previous time step. The bin occupancies and locations of non-empty bins changes with increased loading until

the damage threshold is reached. The actual wing crack lengths (if the model uses no binned solution) is replaced by the predefined bin locations in the grid. The scheme traces the actual solution (no binning used for evolving crack length) at a large number of bins. The example of the stress-strain response is given for a mapping function with a form of exponential distribution CDF. Similar procedure can be followed if the coalescence mechanism is included.

The CDF of wing cracks is considered as the mapping function for these simulations. Since the distribution of wing cracks are not known a priori, two case studies are done based on exponential and uniform distribution. It required a lot of bins (up to 8000) to match the exact solution where no binning was done.

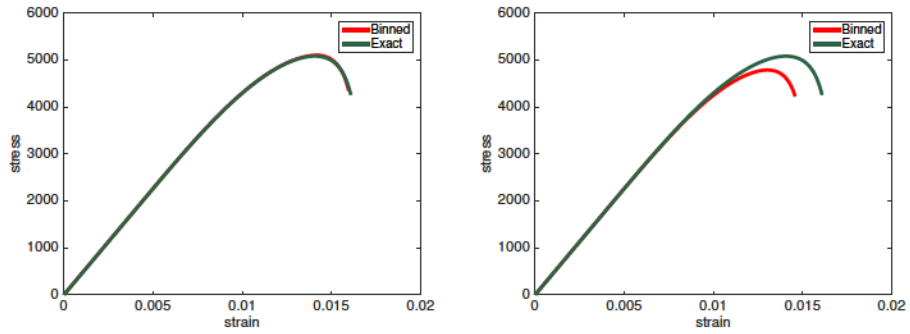

Figure 2.14: Stress-strain comparison for two different distributions of wing cracks. The stress-strain response history shown in the left plot corresponds to the exponential distribution of wing cracks while the response in the right plot corresponds to the uniform distribution of wing cracks. The binned solution is indicated by red color and the exact solution without binning is indicated by green color. 8000 bins are used for both cases.

The new scheme required a lot of bins to trace the exact solution depending on how the wing crack lengths are predicted by Gauss point locations on the unit space. The crack lengths are represented by smaller crack lengths on the realization space due

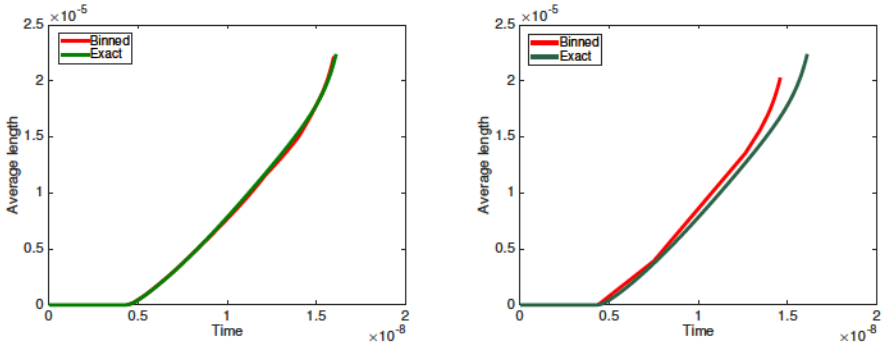

Figure 2.15: The average wing crack length for binned solution is compared with the exact wing crack length without binning. The left plot shows the comparison of average binned (green) and exact (red) wing crack length for exponential distribution of wing cracks. The right plot indicates the same comparison for uniform distribution of wing cracks. 8000 bins are used for both cases.

to mapping of crack lengths to the available nearest Gauss points. The coalescence problem was not attempted due to slow convergence of this method.

2.9 Efficient Binning Scheme Applied to Portable Tonge-Ramesh Model

The efficient binning scheme was applied to obtain the initial flaw statistics for a 3D mechanism-based constitutive model (Tonge-Ramesh model). Since there are many small flaws and few large flaws in ceramic armor materials [8], the flaw population can be categorized as explicit flaws (size in the range of computational mesh size) and subscale flaws (flaw size is much smaller than the computational mesh size). The flaw population in Tonge-Ramesh (TR) model is assumed to have subscale flaws only. The effect of this subscale flaw population in the overall constitutive response is repre-

sented by a micromechanical homogenization approach. To obtain the characteristic input flaw statistics of the specimen of interest a discrete number of realizations of the stochastic microstructure of the material is generated. The statistical distribution of flaw sizes and number of flaws within a sampled volume (V_0) can be defined by a joint probability distribution as [49]:

$$P_{n,a}(n_l < n < n_h, s_l < a < s_h) = \iiint_{V_0} (\int_{n_l}^{n_h} \int_{s_l}^{s_h} f(n, a, \mathbf{x}) da dn) dV \qquad (2.47)$$

The function $f(n, a, \mathbf{x})$ is the joint probability density function (PDF) which describes the probability $P(n, a)$ that there are flaws between n_h and n_l with sizes s_h and s_l within a material local volume V_0. $\mathbf{x}$ in the function in 2.47 represents the spatial location of the flaw population. It is assumed in the TR model that the flaw size, number of flaws and spatial location are independent quantities. So the PDF can be written as [49]:

$$P_{n,a}(n_l < n < n_h, s_l < a < s_h) = \iiint_{\Omega} dV (\int_{n_l}^{n_h} h(n) dn \int_{s_l}^{s_h} g(s) ds \qquad (2.48)$$

where $h(n)$ is the distribution of number of flaws and $g(s)$ is the flaw size distribution. Since it is assumed that the flaw size and their spatial locations are not correlated the number of flaws within a local volume V_0 is obtained from a Poisson distribution where the parameter of the distribution is the average flaw density η multiplied by

the local volume V_0. The flaw number PDF is given by [49]:

$$\iiint_{\Omega} dV(\int_{n_l}^{n_h} h(n)dn = \int_{s_l}^{s_h} \text{Pois}[\eta V_0](n)dn \tag{2.49}$$

The flaw size PDF is given by [49]:

$$P(s_l < s < s_h) = \int_{s_l}^{s_h} g(s)ds \tag{2.50}$$

The flaw size distribution and average flaw density are considered material parameters influenced by the processing techniques. The realization of the flaw sizes and number of flaws are generated based on the distribution within a local particle volume V_0 for a 3D simulation of dynamic brittle failure. The initial flaw statistics for TR model is used in estimating damage variable (D) due to N_f number of sampled cracks in V_0 similar to the 2D micromechanics damage model calculation described in 2.7. The damage variable is calculated for TR model as[49]:

$$\Omega = \sum_{k=1}^{N_{\text{bins}}} \omega_k {s_k}^3 \tag{2.51}$$

The representative flaw size s_k for a bin in TR model is chosen as the sample mean size of that bin where total N_k flaws are sampled within the particular bin. The N_k is

obtained from the Poisson distribution with a parameter $V_0\omega_k$. ω_k is defined as [49]:

$$\omega_k = \eta(G(s_k^h) - G(s_k^l)) \tag{2.52}$$

where G indicates the CDF of flaw size. For a smaller number of flaws within a bin all the flaws are sampled and their mean is calculated to determine the representative flaw size of the bin. If there is large number of flaws within each bin the N_k is sampled from a Gaussian distribution (applying Central Limit theorem). To create a local representation of the microstructure the flaw statistics is binned with a representative flaw size (mean of the sampled flaw sizes of a particular bin) and flaw density sampled from Poisson distribution if it sufficiently low (less than or equal to 20). The choice of the representative flaw size is skewed towards the larger flaws by using a bias function to make the bin width larger for the bin with larger flaw sizes. It is assumed in TR model that the initial flaw size distribution follows a bounded Pareto distribution. The CDF of the distribution is:

$$G(s) = \frac{1 - (\frac{s}{s_{\min}})^{-\alpha}}{1 - (\frac{s_{\max}}{s_{\min}})^{-\alpha}} \tag{2.53}$$

where $s_{\min}$ and $s_{\max}$ are the minimum and maximum flaw sizes and α is the distribution parameter.

The efficient binning scheme is implemented in TR model using a zooming function

based on the bounded Pareto CDF. The zooming function is:

$$s = \left(\frac{\alpha\left(\frac{1}{r\left(\left(\frac{s_{max}}{s_{min}}\right)^{-\alpha}-1\right)+1}\right)^{\frac{3}{\alpha}}\left(r\left(\left(\frac{s_{max}}{s_{min}}\right)^{\alpha}-1\right)-\left(\frac{s_{max}}{s_{min}}\right)^{\alpha}\right)}{(\alpha-3)\left(\left(\frac{s_{max}}{s_{min}}\right)^{\alpha}-1\right)} - k\right)\frac{1}{c} \tag{2.54}$$

k and c are integrations constants and can be obtained from $r(0) = 0$ and $r(1) = 1$.

The representative flaw size within each bin for efficient binning scheme is fixed for a given number of bins. In efficient binning scheme bin width varies and it is skewed towards the larger flaw sizes based on the criterion that each bin contributes equally to the global damage. The simulation result of different binned result for uniaxial compression is compared with an exact solution of 500 cracks for TR constitutive model. The flaw density is computed as η multiplied by the bin weight for binned

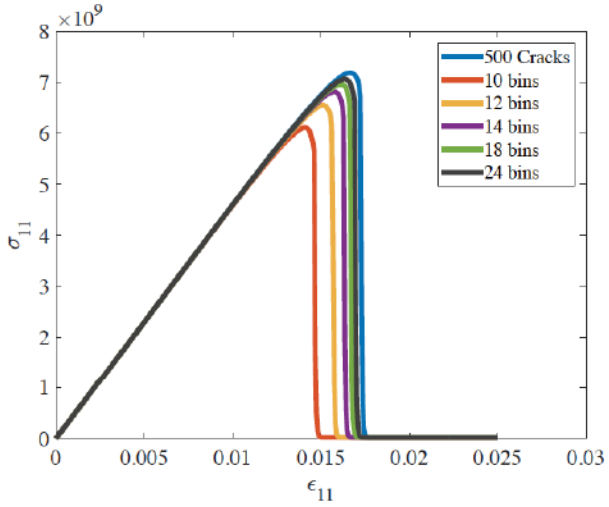

Figure 2.16: Stress-strain response of TR model for uniaxial compression with a strain rate of $500\,s^{-1}$. A flaw population of 500 is considered as an exact solution where each flaw and the microcrack from the flaw is evaluated in the damage calculation. The population of 500 flaws are binned into 10,12,14, 18 and 24 bins. 24 bins match the exact solution most accurately.

case and η multiplied by $\frac{1}{p_{\max}}$ for exact solution. The existing binning schemes in TR model can only use bounded distributions. The efficient binning scheme can use both bounded and unbounded distribution since it uses a random variable space with an upper limit of 1. It is shown in figure 2.16 that 24 bins predicts the most accurate solution when compared to the 500 crack solution. The stress-strain response using 18 bins also tracks the 500 crack solution accurately. Reducing the number of bins to 18 might be computationally beneficial in case of larger-scale simulations with millions of elements or material points used to solve the actual BVP of interest. The efficient binning scheme has the same degree of accuracy as the binning schemes proposed in TR model.

2.10 Summary

A novel and significantly cost-saving binning scheme is developed for sampling-based evaluation of expressions characterized by a discrete expectation summation, equation (2.1), in which we find the average of a function $h(\hat{x})$ evaluated over a population of random variable realizations $\hat{x}_1, \ldots, \hat{x}_{p_{\max}}$ in which $p_{\max}$ is intractably large. Similar functions are found in many applications, so the approach is broadly applicable to many disciplines of applied mathematics. As is true for any binning scheme, the large set of input variables of the function is replaced by a smaller set of bins containing the subpopulations of those variables. The purpose of binning is to increase the computational efficiency while maintaining an acceptable level of solution accuracy. Among the novel aspects of the new binning scheme is a rigorous mathematical basis for and straightforward control of the balance between accuracy and efficiency. To illustrate the efficacy of the approach, the binning scheme is applied in the context of crack population evolution in damaged media. In particular, viewing the crack population in the probability, or reference, space allows for a generalized approach that holds for random crack characteristics described by any probability distribution. In the context of a computational model of material failure, the overall constitutive response of the material within a particular subdomain is a function of global damage (*e.g.,* defined for a simple model in equation (2.3)), which results from the presumably large sub-grid-scale crack population residing within that material subdomain. To bin the large crack population, the crack data (*e.g.,* crack length and orientation for a

2D problem) are mapped to grid nodes and associated Gauss points on a reference grid laid out in probability space. The Gauss points on the grid are considered as bin centers that are associated with the crack characteristic(s) representing each bin, and the weights corresponding to Gauss points are considered as bin occupancies, which represent the fraction of cracks that are associated with that bin. The global damage for the binned crack population is determined using a reduced summation over only the bin weights and locations. Therefore, the large crack population is replaced by a *much* smaller (tractable) number of bins, which significantly decreases both CPU and memory computational costs. Different binning schemes for different computational problems are developed in many research works. Most of those previous works aim to reduce computational efforts by efficiently binning large data sets. While our goal resembles other works in developing binning schemes, the previous binning schemes are generalized by using the probability space. The accuracy of the solution can be improved by using a non-uniform grid or a zoomed grid in probability space. In general, this scheme is applicable to the evaluation of functions involving an arbitrary number of random variables. Example problems based on a micromechanics damage model demonstrate the efficiency and accuracy of the current binning scheme. Three types of binning based on the same binning concept are also compared: one based on equally spaced bins in the state (or crack length) space, one based on equally spaced bins in the reference (or probability) space, and one based on bins that are zoomed in order to ensure equal contribution of each bin to the initial global damage. Examples

assuming both an infinite number of sample crack lengths and a finite number of sample crack lengths are evaluated. The same binning methodology is applied also in the context of a 3D constitutive model (TR model) which accounts for the same micro-scale cracking mechanism as described in the 2D micromechanics model along with other microphysical mechanisms. A new zooming function has been developed for skewing the probability space towards the bins with larger crack sizes. The efficient binning scheme shows the same degree of accuracy when compared with an exact solution of 500 random flaws. In addition, an initial mathematical concept is laid out to bin an evolving crack population as an extension of the current binning framework. The results can be summarized as follows:

- For a fixed number of bins, the stress-strain response of the micromechanics model using the binned solution matches the exact solution (evaluating response for each individual crack) most accurately when the zoomed (equal-damage) grid is used. This trend is the same for both infinite and finite number of sample cracks.

- Error for all three binning schemes reduces to zero as a finer discretization is used in probability space. The error for the zoomed binning approach is typically about one order of magnitude lower than the other binning schemes. Binning using a zoomed grid converges faster than other schemes. More complicated metrics of influence (which merely define the grid density in the binning framework) may be easily accommodated by using, for example, anisotropic

Delaunay tessellations [83] with triangle (or tetrahedral) grid shape functions instead of the rectilinear grid used in our examples.

- Notable sample-to-sample variability in the predicted stress-strain response is observed when the crack population is small. As observed for the other cases, the zoomed grid binning shows the least error relative to the reference solution. In addition, the sample-to-sample variability is captured well by the binning schemes.

- The binning scheme shows an accurate tracking of the exact solution (500 flaw population) in case of a 3D constitutive model which accounts for the subscale mechanism via a micromechanics damage model with an advantage of capturing a wide range of bounded and unbounded initial flaw distribution.

The results demonstrate that giving attention to how one bins a crack population in damage mechanics can have a profound effect on the computational efficiency and accuracy of the associated models. Probabilistic methods provide the ideal construct for this through transformation into probability space. In particular, by applying a zooming function one can identify optimal bins for any population (e.g., a different damage model). The current results apply binning to the initial crack population, and assume that the bin locations in the reference (probability) space and the bin occupancies remain constant with loading. The crack characteristics evolve under loading, which simply manifests itself in a change of the transformation from the

reference space to the state space. This approach is consistent with a crack population in which there are no sources, sinks, splitting or merging that might develop under loading; however, it is recognized that maintaining a static binning over time may not be optimal from the perspective of accuracy and/or efficiency. For example, if in a particular case the majority of damage is associated with only a very few bins (*e.g.,* the large initial cracks only), then adaptively refining the bins that represent the larger cracks might provide a more accurate result while requiring fewer bins generally. While an evolving binning scheme was not developed explicitly, figure 2.2 provides a notional description of how such an approach would work. In effect, one would evolve binning according to the current configuration $\hat{x}(t)$, rather than simply the initial configuration $\hat{X}$. In a similar vein, an evolving binning scheme (modified to include sources and sinks) provides an elegant means to address crack populations in which new cracks nucleate, cracks self-heal, and cracks coalesce under loading. A methodology has been outlined in this chapter to address the issue of binning an evolving population of random inputs of a function. Simulations are also done based on the evolving crack population described by a 2D micromechanics model. The initial simulations match the solution by a large number of bins. Future work might focus on improving the efficiency of the current framework to capture the evolving crack population with a smaller number of bins.

Chapter 3

Crack Coalescence Model

3.1 Crack Coalescence in Brittle Materials

The continuum scale neighborhood of a material point or an integration point is heterogeneous at the micro-scale. Each material point has an underlying microstructure consisting of grains, grain boundaries, voids, inclusions, micro-cracks and other heterogeneities. The microstructure of brittle materials (rocks, ceramics, ceramic composites, cement etc.) shows the presence of defects which play a central role in the mechanical response. At the macro-scale, brittle materials under compressive loading exhibit complex nonlinear behavior that is strongly affected by the micro-scale defects. In particular, the stress-strain response is characterized by linear elasticity,

damage growth, and rapid strain softening.

The mechanisms underlying this response are associated with nucleation, propagation and coalescence of microcracks (discussed in chapter 1). The nucleation of open tension microcracks, or wing cracks, in brittle materials occurs due to the relative sliding on the flaw surfaces under global compression (the wing crack model is discussed in chapter 1). As these cracks grow, some of them begin to intersect with each other to form larger cracks. Under dynamic loading, micro-cracks develop from a large number of pre-existing flaws, therefore, coalescence of these cracks plays a major role in dynamic failure. In a recent experiment on transparent polycrystalline ceramics, Paliwal et. al. [3] demonstrated the effect of microcrack coalescence on the macroscopic stress-strain response of AlON under high strain rate loading. The results from this dynamic compression test are presented by a series of high speed images together with a stress-time history plot (see figure 3.1). The images in figure 3.1 depict the failure of an AlON sample under dynamic compression from an initially undamaged state. The formation and coalescence of the cracks are visible as white regions in the transparent sample. Image 1 in the upper row shows a relatively undamaged state, in which the sample remains intact and deforms fairly uniformly. Initial cracks become visible in image 2, indicated by white arrows. These cracks coalesce and a relatively larger damage zone is observed in image 4, when the sample is near its peak stress. From images $5-8$ the damage zone grows significantly larger due to coalescence of multiple cracks. This dynamic compression experiment

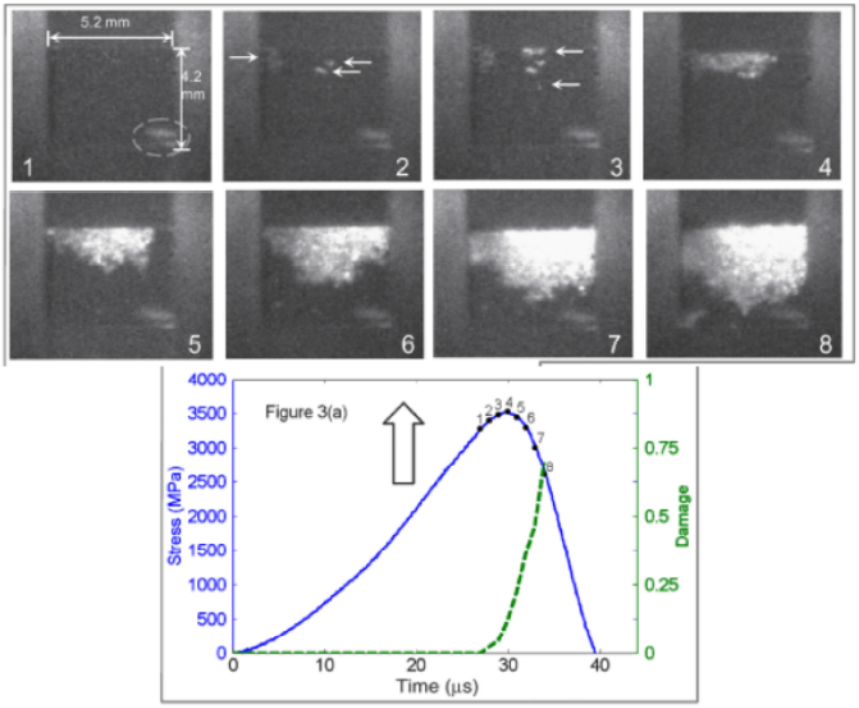

Figure 3.1: Kolsky bar experiment on AlON [3] at a loading rate of 155MPa μs^{-1}. The upper part of the figure shows images of the sample undergoing uniaxial dynamic compression, and the lower part shows the corresponding time history plot. The numbers on the high speed images correspond to the points indicated by the same number in the stress-time history plot. White regions in the high speed images indicate the presence of cracks.

demonstrates qualitatively that coalescence of cracks leads to significant damage.

The coalescence of crack pairs under quasi-static loading is observed in various experiments done on geologic materials [31], [33], [2], [32]. These experimental observations identify different modes of coalescence (see figure 3.3). Numerical approaches have also been developed to model these modes of coalescence [34], [35]. However, the existing models address only a few preexisting defects, matching the modes of coalescence that are observed in quasi-static experiments. These models do not capture the crack coalescence occurring for a large population of dynamically propagating microcracks.

A micromechanics-based crack coalescence model is proposed here to capture the effect of explicit micro-crack coalescence on the dynamic strength of brittle materials. The possible modes of coalescence are identified from the experimental observations in figure 3.3 (from [33]). As with the original PR model [23] described in chapter 1, the input for the micromechanics model is a number density and size distribution describing preexisting defect population. Coalesced cracks are introduced into the crack population as the loading increases, using a probabilistic approach. The model predicts that crack coalescence leads to significant reduction in the peak stress of the material under dynamic compression.

3.2 Crack Coalescence Model

The coalescence model proposed here aims at capturing the effect of crack coalescence on the macroscopic stress-strain response. The model is based on the basic sliding crack or wing crack model discussed in chapter 1.

The basic methodology of the crack coalescence model is to update the crack population to introduce newly coalesced cracks at each load step. The interaction of all the single and coalesced cracks in the medium is captured by the Paliwal-Ramesh (PR) [23] effective medium approach. As a result, the effective damage in the material is associated with both the single crack population and the coalesced crack population (see figure 3.2). Similar to the self-consistent model for single cracks, the analysis assumes an elliptic inclusion surrounding a coalesced crack is placed in a medium with effective properties updated by the global damage. The local stress field inside the elliptic inclusion is estimated by solving the 2D boundary value problem [41], [42] of an infinite medium with an inclusion under far-field principal stresses (see Appendix B). Each crack enclosed in the elliptic region interacts with other cracks indirectly, through the damaged effective medium in which the inclusion is placed. Figure 3.2 illustrates the self-consistent approach for the coalescence model. The lower left figure corresponds to the original PR model, in which damage is associated only with single cracks. The lower right figure corresponds to the proposed coalescence model, in which damage is associated with both single and coalesced cracks. The effective medium approach is adopted for different patterns of coalesced cracks. The

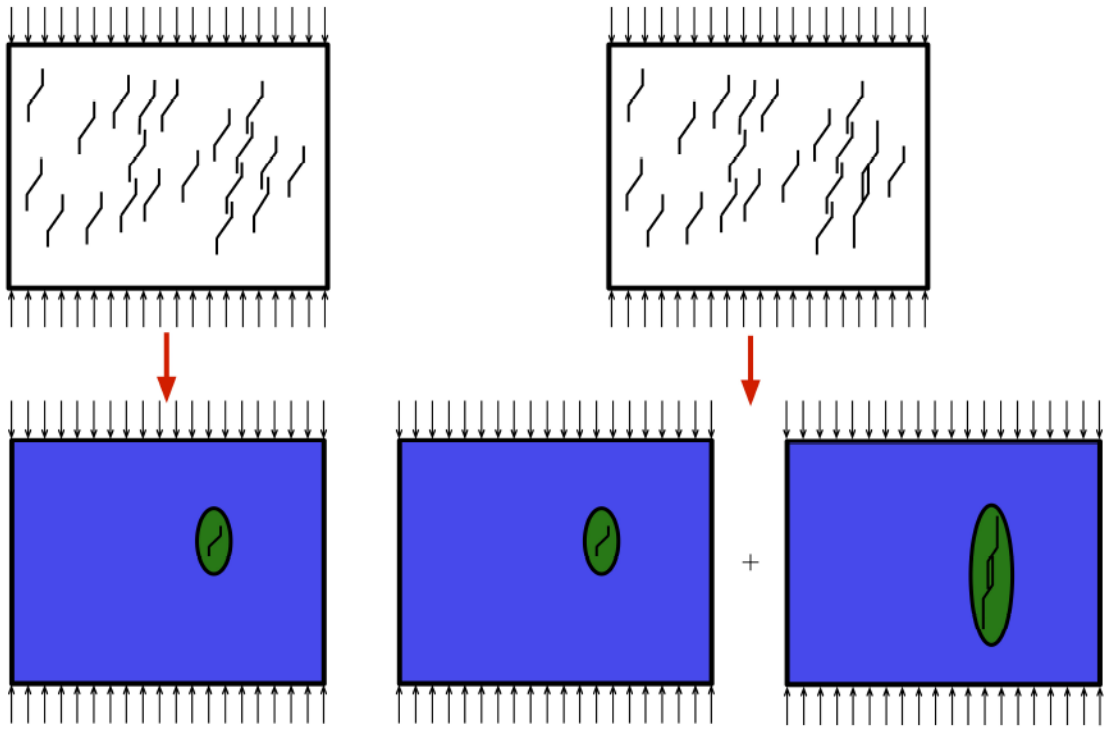

Figure 3.2: The left side of the figure shows the medium with single cracks only along with the corresponding effective medium approach underneath. The right side of the figure shows the medium with single and coalesced cracks along with the corresponding effective medium approach for single and coalesced cracks. Using the effective medium approach, single cracks are represented by an elliptic region (in green) surrounded by homogenized damaged medium (in blue). Similarly, single and coalesced cracks are also represented by elliptic regions.

patterns of coalesced cracks considered in the model are discussed in the next section.

3.2.1 Pattern of Crack Coalescence

Crack coalescence has been observed in brittle materials under both quasi-static and dynamic loading. However, the nature of the coalescence depends on a number of factors, one of which is the direction of crack propagation. In other words, the stress field at the crack tip plays a major role in the coalescence as the cracks propagate in the direction of maximum energy dissipation [60]. The stress field at the crack tip is influenced by interaction with neighboring cracks which is stronger as the two cracks are closer together [5]. Wing cracks in brittle materials under uniaxial compression propagate in the direction of maximum principal compression [16], [40]. Models of the wing crack mechanism usually deal with either a single wing crack in an infinite brittle solid or a periodic array of wing cracks. Coalescence between pairs of wing cracks have been reported by [34], [2]. Wong et. al. [2] report two typical patterns of coalescence under quasi-static compression (see figure 3.3). One pattern shows the wing cracks merging with a flaw surface of another crack (second and third row of figure 3.3), and the other shows a secondary shear crack forming either between the flaw surfaces or between the tips of the wing cracks (first row of figure 3.3). These two patterns of coalescence are considered as the modes of coalescence applied in the micromechanics model.

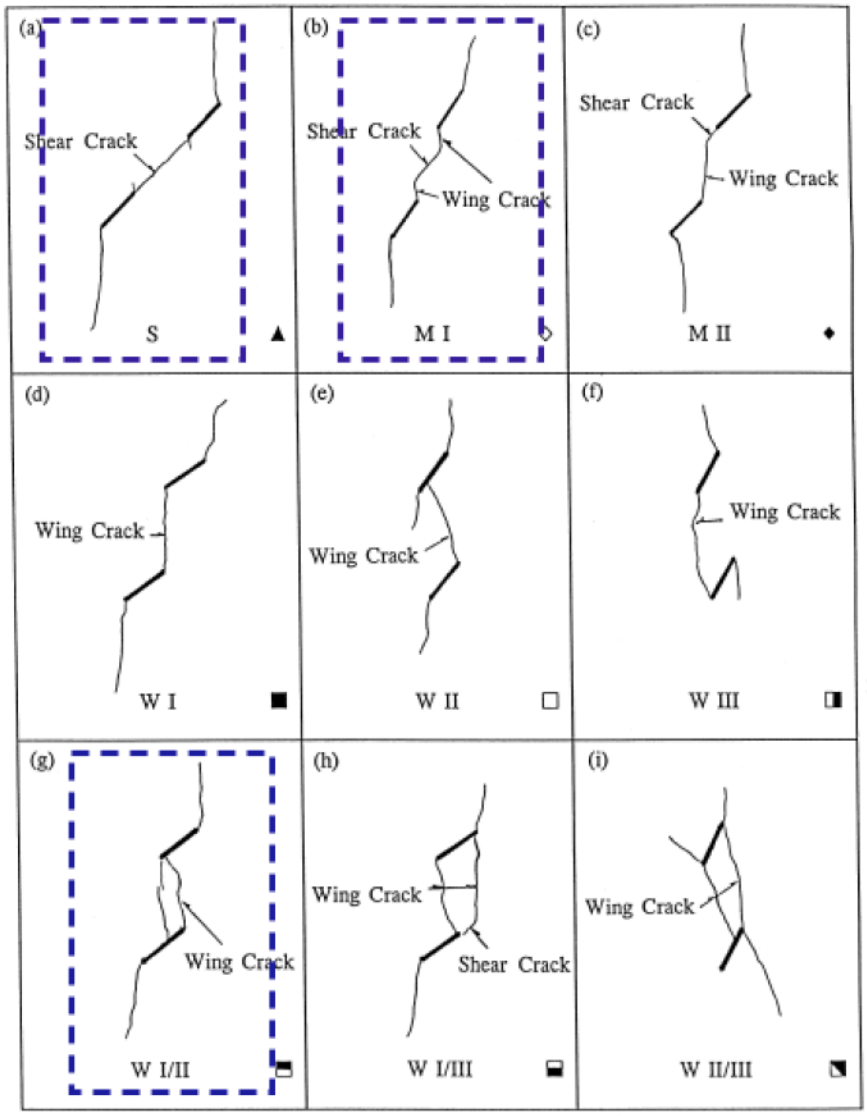

Figure 3.3: Different patterns of coalescence under quasi-static compression experiments on a rock-like material [2]. The sample contains two preexisting flaws at different spacings and angles with respect to the direction of compression. Wing cracks initiate from the tip of the preexisting defects. The different coalescence patterns are enacted by altering the angle between the two neighboring flaw tips, the distance between the flaw tips and also the angle of inclination for the flaws. The dotted box in the first row of the figure shows two patterns of coalescence through secondary shear cracks, and dotted box in the bottom row shows a pattern of coalescence when two wing cracks intersect each other's flaw surface. These are the coalescence pattrens that are incorporated into the coalescence model.

3.2.2 Crack Coalescence in a Population of Cracks under Dynamic Loading

The previous section described the possible modes of coalescence for two neighboring cracks. Under dynamic loading, multiple cracks initiate from pre-existing flaws, so models of dynamic failure must contend with coalescence of multiple cracks. Because the initial flaws are randomly located in the material domain, the spacing between the pairs of wing cracks vary randomly. Therefore, multiple coalescence patterns of cracks emerge.

A schematic for microcrack coalescence under dynamic compression is given in figure 3.4 matching the patterns of coalescence observed in the rock experiment [2]. There are several coalesced crack patterns shown in figure 3.4. The cracks shown in red are coalesced through wing crack growth. The cracks created when two single wing cracks coalesce are considered one pattern of the population (see figure 3.5a). A fraction of this pattern of coalesced cracks can coalesce with yet another single crack and form another pattern of cracks (see figure 3.5b). Furthermore, some of these coalesced cracks merge with each other, leading to the larger coalesced crack shown in figure 3.5c. For certain inter-crack spacings, the cracks coalesce through secondary shear cracks (shown in dotted green line in figure 3.4). These coalesced cracks produce a fourth and fifth pattern of cracks (see figure 3.6).

Within a crack pattern, there is a range of intercrack spacings depending on the

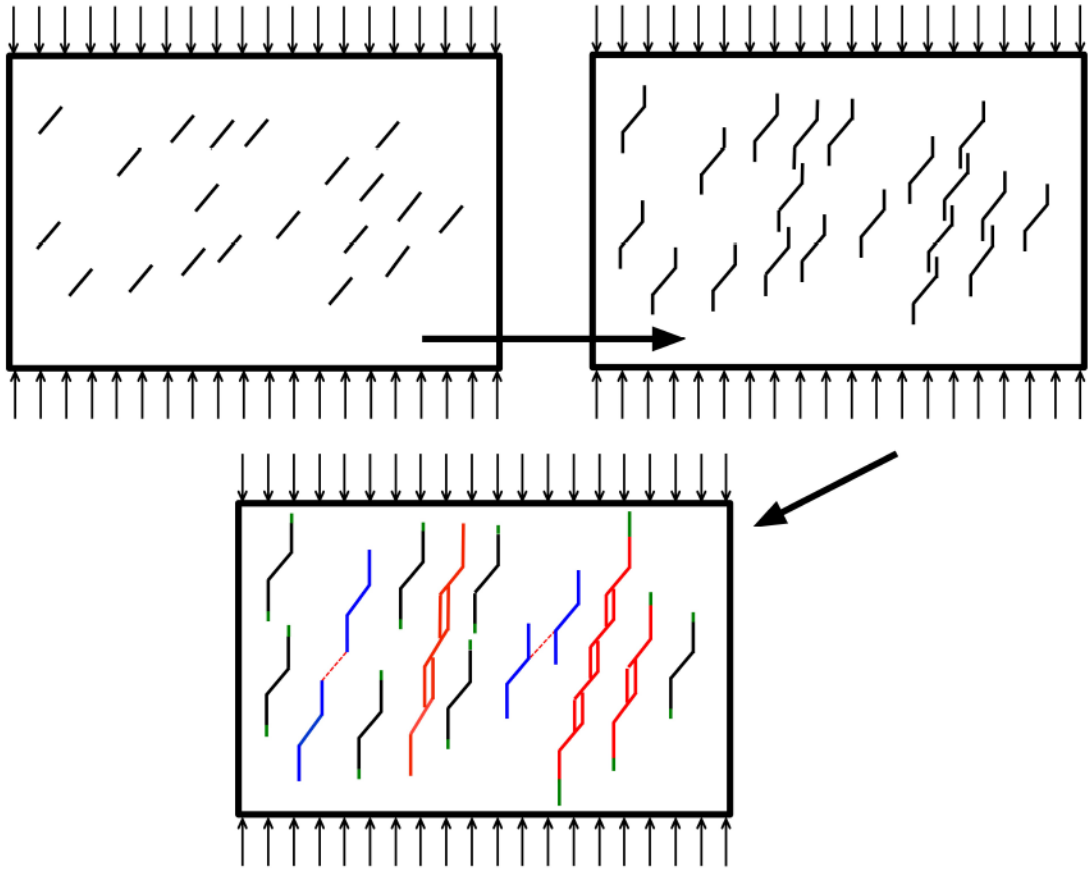

Figure 3.4: Schematic of the evolution of cracks under increasing loads. The first figure represents the medium with pre-existing flaws under dynamic compression. The second figure represents the wing-cracks propagating from the flaw surface. Different patterns of coalescence occurring at some stage of loading are shown in the third figure. The red cracks are pattern-1, pattern-2 and pattern-3 cracks while the blue cracks are pattern-4 and pattern-5 cracks (shear cracks). The green line indicates the crack growth increment associated with the cracks at a load step. The crack growth increments are larger for the larger coalesced cracks.

crack length at which coalescence occurs. Therefore, within each pattern there is a growing number of families as the load progresses. This sequential process of crack merging is outlines in figure 3.5.

- The first row of coalesced cracks in figure 3.5a relates to coalescence of two single cracks. Closely spaced pairs of cracks (left in figure 3.5a) lead to a different configuration of the coalesced crack than more distant pairs of cracks (right in figure 3.5b). Furthermore, each load step introduces a new inter-crack spacing of the coalesced crack. This means that a large number of families of coalesced cracks accumulates with increasing load. This pattern of coalescence will be referred as "pattern-1" coalescence hereafter. Each family of cracks belonging to pattern-1 differs from one another, as the distance between flaw surfaces (l in figure 3.5a) associated with each family is different. The contribution to total damage by pattern-1 cracks is $\Omega_1 = \eta_1 \sum_{i=1}^{N_{\text{family}}} \left(\frac{l_i}{2} + l_{1i}\right)^2 P_{1i}$, where η_1 is the number density of pattern-1 cracks, P_{1i} is the fraction of pattern-1 cracks with dimensions (l_i, l_{1i}) and l and l_1 are the crack lengths in figure 3.5a.

- The second row in figure 3.5b shows the coalesced crack families occurring by merging a single crack with a pattern-1 coalesced crack. This pattern, referred to here as "pattern-2", has three flaw surfaces. As in the case of pattern-1 cracks, multiple pattern-2 coalesced crack families are created as the load increases. Each family belonging to this pattern differs by the distance (l_1' in figure 3.5b between the flaw surfaces. The contribution to total damage by pattern-2 cracks

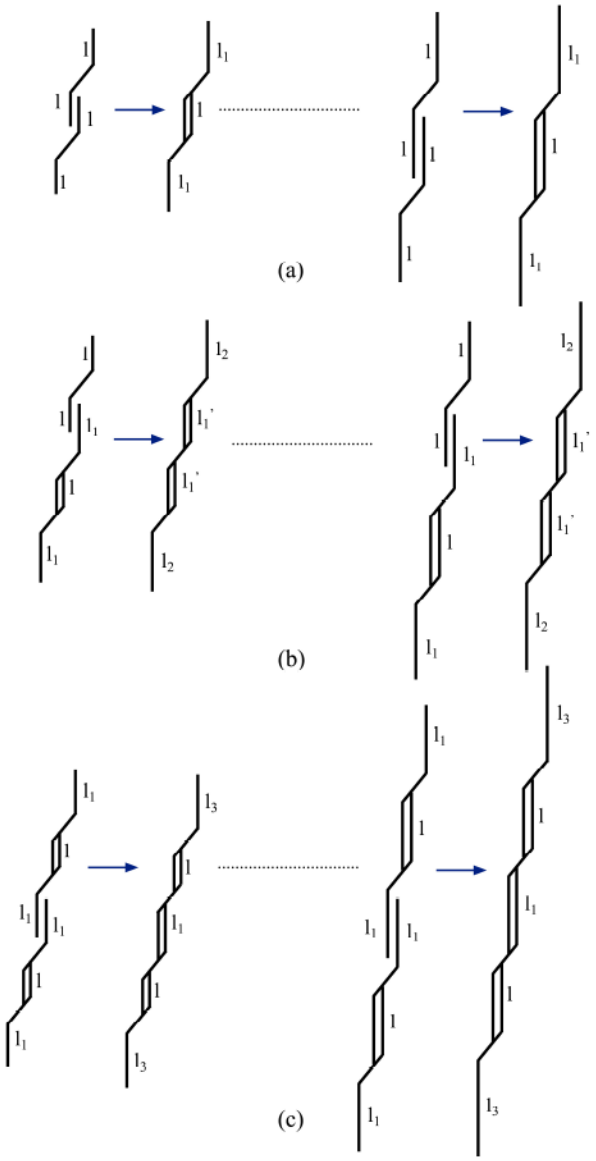

Figure 3.5: Illustration of pattern-1, pattern-2 and pattern-3 coalesced cracks: (a) Two single cracks merge to form a pattern-1 crack. A new coalesced crack family is formed at each load step. The length l_1 is the wing crack length associated with each pattern-1 coalesced crack family. The distance l between the flaw surfaces is different for the newly formed pattern-1 crack at each load step. (b) A single pattern-1 crack is merged with a single crack to form a pattern-2 crack. The length l_2 is the wing crack length associated with this pattern-2 coalesced crack family. The distance l_1' is different for each newly coalesced pattern-2 crack family. (c) Two pattern-1 cracks merge to form a pattern-3 crack, where l_3 is the wing crack length and l and l_1 represents the spacings between the flaw surfaces.

is $\Omega_2 = \eta_2 \sum_{i=1}^{N_{\text{family}}} \left(l'_{1i} + l_{2i}\right)^2 P_{2i}$, where η_2 is the number density of pattern-2 cracks, P_{2i} is the fraction of pattern-2 cracks with dimensions (l'_{1i}, l_{2i}) and l'_1 and l_2 are the crack lengths in figure 3.5b.

- The third row in figure 3.5c shows coalesced crack families occurring when two pattern-1 coalesced cracks merge with one another. This pattern of coalescence, here referred to as "pattern-3", has four flaw surfaces. The different crack families in pattern-3 coalescence are distinguished by the distances between the flaw surfaces (l and l_1 in figure 3.5c). The contribution to total damage by pattern-3 cracks is $\Omega_3 = \eta_3 \sum_{i=1}^{N_{\text{family}}} \left(\frac{l_{1i}}{2} + l_i + l_{3i}\right)^2 P_{3i}$, where η_3 is the number density of pattern-3 cracks, P_i is the fraction of pattern-2 cracks with dimensions (l_{1i}, l_i and l_{3i}) and l_1, l and l_3 are the crack lengths shown in the third row of figure 3.5.

- The evolution of coalescence can continue to higher order coalescence until the sample reaches a predefined damage threshold. However, any higher order coalescence is ignored here due to their very low probability of occurrence (to be discussed later in this section).

The same sequential coalescence process is also adopted for the coalesced crack families merged by the secondary shear crack (see figure 3.6). The coalescence shown in the first row of figure 3.6 will be referred as "pattern-4" and the coalescence shown in the second row will be referred as "pattern-5" hereafter. The contribution to total

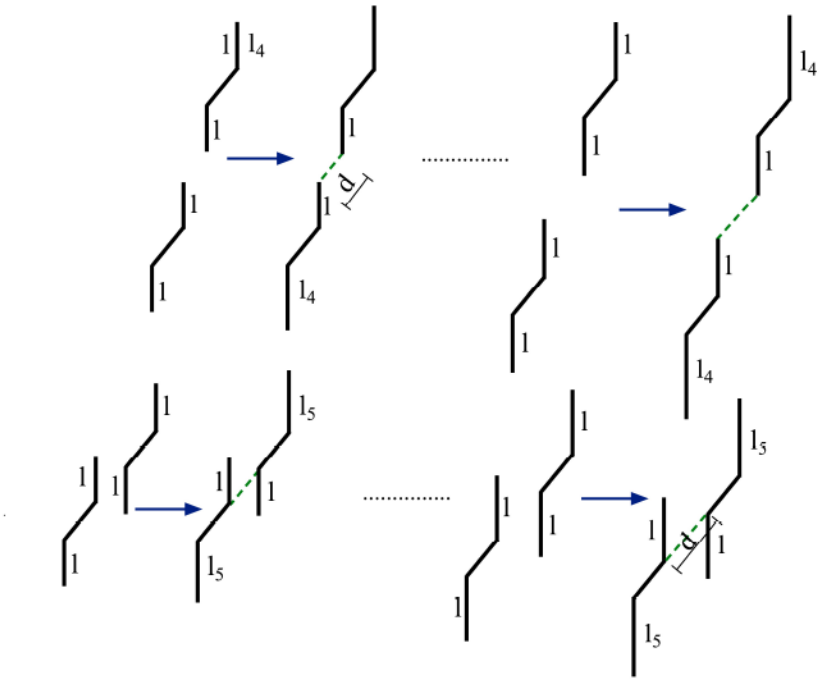

Figure 3.6: Illustration of pattern-4 and pattern-5 cracks. The first row of the figure shows pattern-4 coalescence, which occurs when a shear crack forms between the tips of the wing cracks of two single cracks. At each load step a new pattern-4 crack family forms with a growing new wing crack length l_4. The second row in the figure shows pattern-5 coalescence, which involves merging of two single cracks by a shear cracks forming between the two flaw surfaces. There is a new pattern-5 crack family formed at each load step, with a growing wing crack length of l_5.

damage by pattern-4 cracks is $\Omega_4 = \eta_4 \sum_{i=1}^{N_{\text{family}}} \left(l_i + l_{4i}\right)^2 P_{4i}$, where η_4 is the number density of pattern-4 cracks, P_{4i} is the fraction of pattern-4 cracks with dimensions (l_i, l_{4i}) and l and l_4 are the crack lengths shown in the first row of figure 3.6 while the contribution to total damage by pattern-5 cracks is $\Omega_5 = \eta_5 \sum_{i=1}^{N_{\text{family}}} l_{5i}^2 P_{5i}$, where η_5 is the number density of pattern-5 cracks, P_{5i} is the fraction of pattern-5 cracks with dimension (l_{5i}) and l_5 is the crack length shown in the second row of figure 3.6.

A number of crack families are created at each load step due to this sequential coalescence mechanism. The crack lengths associated with each family are homogenized into macroscale properties through the global damage variable, $\Omega = \Omega_0 + \Omega_1 + \Omega_2 + \Omega_3 + \Omega_4 + \Omega_5$ where $\Omega_0 = \eta_0 l^2$ is the damage associated with the single cracks, where η_0 in the number density of the single cracks and l is the crack length. The next section describes the calculation of crack growth rate and associated evolution of the coalesced crack families.

3.2.3 Estimation of Crack Growth Rate for Coalesced Crack Families

In pattern-1 coalesced cracks, two flaw surfaces produce the sliding force that drives the further crack growth. In particular, the two flaw surfaces are represented by a pair of splitting forces acting at the location of the flaw surfaces (see figure 3.7). Similar to the procedure used by Nemat-Nasser [14] for single wing cracks, the kinked

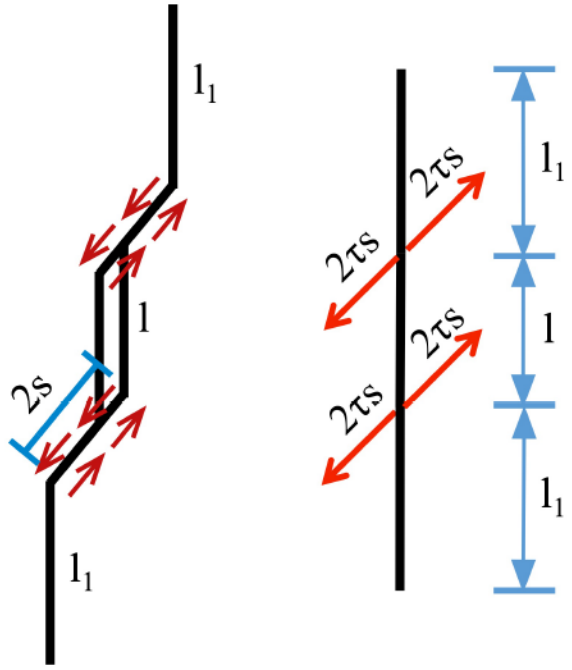

Figure 3.7: Pattern-1 crack with the two sliding flaw surfaces represented by two equal pairs of splitting forces acting at the flaw locations on a straight crack.

crack is represented as a straight crack with two pairs of splitting forces in place of the two sliding flaw surfaces. The distance l between the pair of forces varies from one pattern-1 crack family to the next. The crack driving forces for other coalesced crack patterns are estimated using an analogous approach (see figure 3.8). Pattern-2 coalesced cracks have three pairs of splitting forces, and pattern-3 coalesced cracks have four pairs of splitting forces that drive crack growth. In order to simplify the model, a symmetric crack is used to approximate pattern-2 coalescence. The distance $l_1' = \frac{2l_1+l'+l}{4}$ between the pair of splitting forces is assumed to be equal, where l_1 is the length of the wing crack for pattern-1 coalesced crack, l' is the distance between the driving forces of the pattern-1 coalesced crack, and l is the length of the single wing

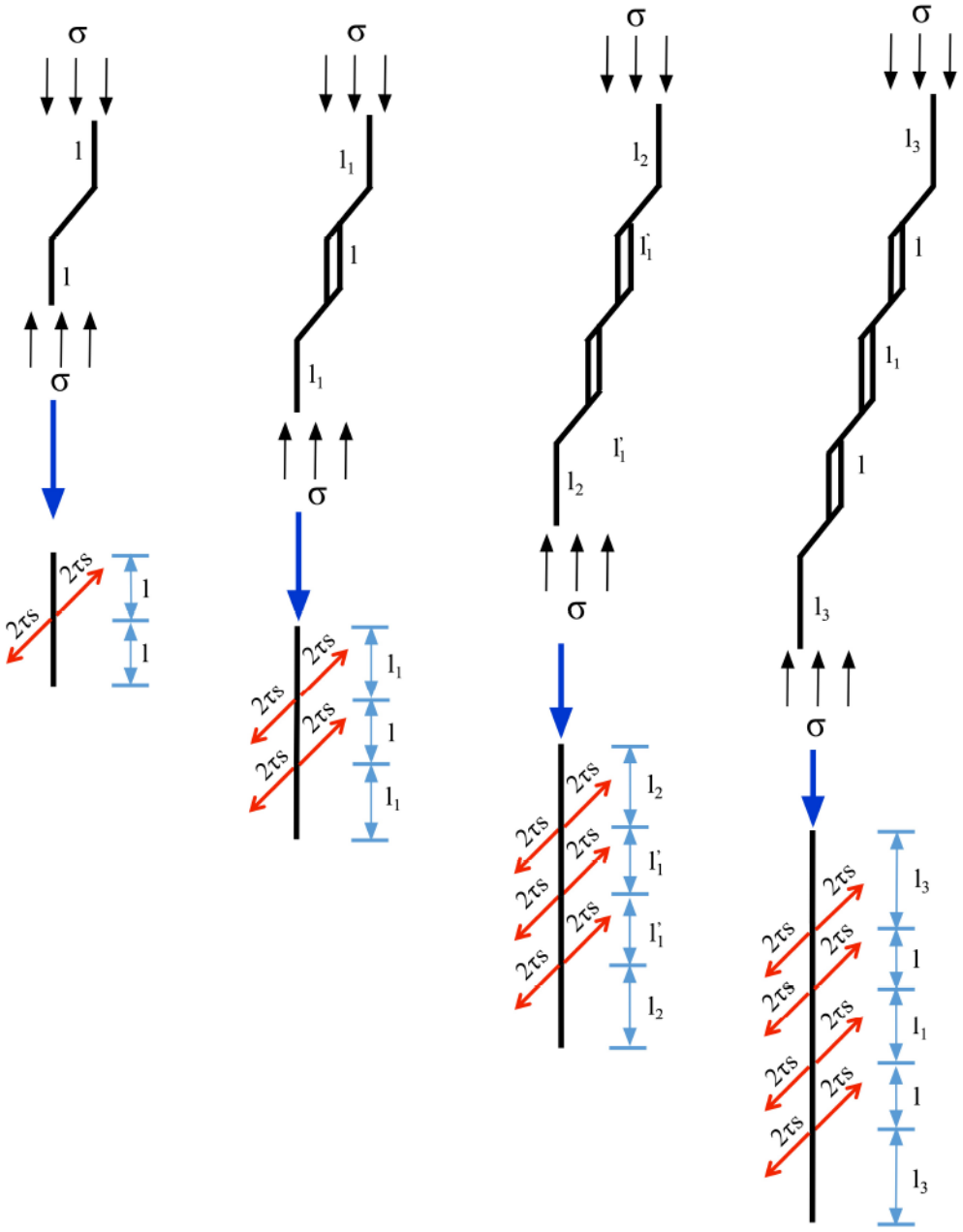

Figure 3.8: Idealized straight cracks representing pattern-1, 2 and 3 coalesced wing cracks. The larger coalesced cracks are driven by extra pairs of splitting forces acting at the location of flaw surfaces. The idealized straight cracks represent sliding flaw surfaces by pairs of splitting forces, as shown in the figure for each representative crack.

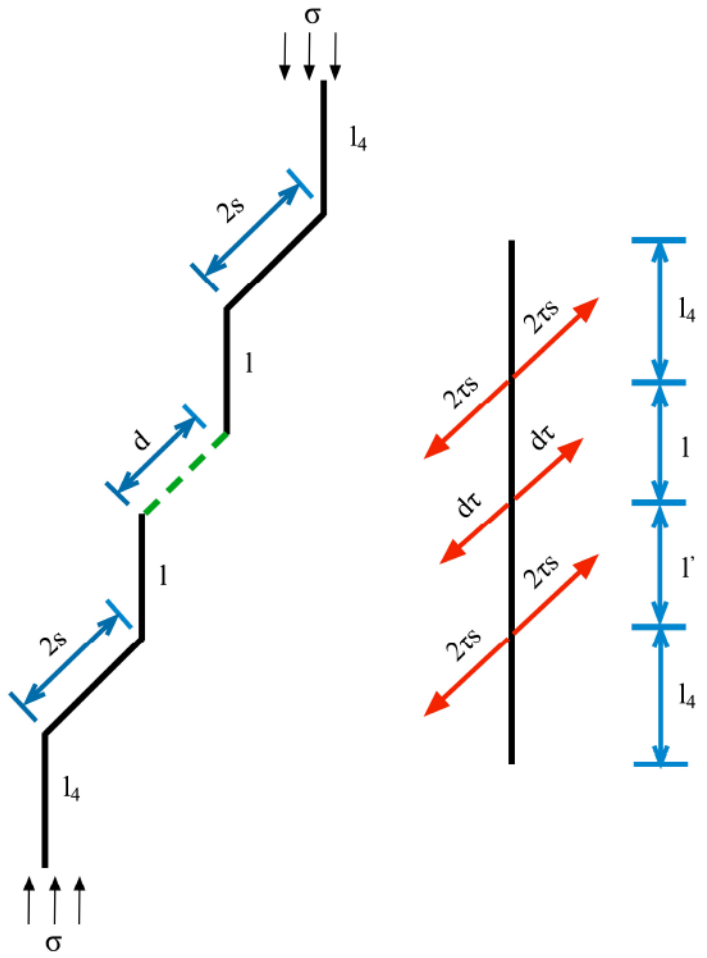

Figure 3.9: Illustration of a pattern-4 crack with a shear crack of length d formed between the tips of the underlying single wing cracks,. An extra pair of splitting forces represent sliding on the newly formed shear crack surface.

crack (see figure 3.8). The forces on the pattern-4 and pattern-5 coalesced cracks are outlined in figures 3.9 and 3.10, respectively. The fracture plane with length d shown in figure 3.9 is assumed to occur at the instant when the traction force acting on the plane exceeds the static shear strength of the material. The length d of this newly created crack plane is calculated from the criterion $d \leq \frac{F}{\tau_{\max}}$ where F is the traction force acting on the plane and $\tau_{\max}$ is the shear strength of the material. The

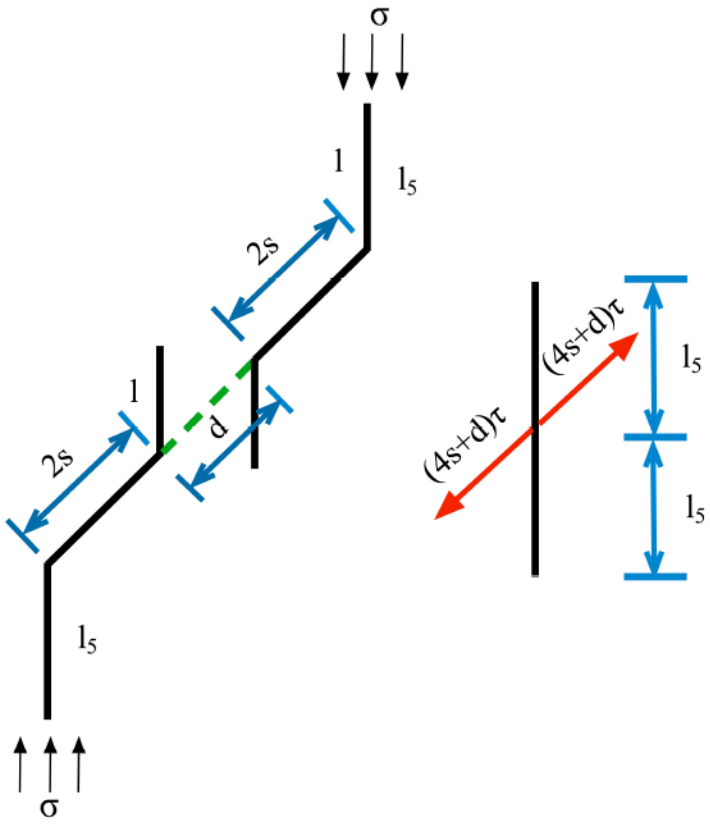

Figure 3.10: Illustration of a pattern-5 crack. The two existing flaw surfaces are joined by the shear crack formed between them. The length of the new sliding surface increases the crack driving force to $(4s + d)\tau$.

inclination of the shear crack plane is assumed to be the same as the inclination of the flaw surface. The new shear crack surface leads to an additional sliding force on the cracks equal to the critically resolved shear stress τ on the plane, multiplied by the length d. The criterion for shear cracking in pattern-5 coalesced cracks is similar to that for pattern-4 coalescence (see figure 3.10). The new shear crack is merged with pre-existing flaw surfaces to provide an increased driving force for crack growth.

The crack growth speed is directly related to mode-I stress intensity factor K_I [23] (see chapter 1 for more details):

$$\dot{l} = \frac{C_R}{\alpha}\left(\frac{K_I - K_{Ic}}{K_I - 0.5K_{Ic}}\right)^{\gamma} \tag{3.1}$$

The stress intensity factor [15] for a single crack family is:

$$K_{\mathrm{I}} = \frac{2s\tau\cos\phi}{\sqrt{\pi(l+0.27s)}} + \sigma_{22}\sqrt{\pi l} \tag{3.2}$$

where s is the flaw size, l is the wing crack length, ϕ is the angle between the direction of maximum principal compression to the flaw surface normal (see figure 1.2), τ is the local resolved shear stress on the flaw surface and σ_{22} is the local stress in the direction normal to maximum principal compression. The local stress is estimated by the self-consistent calculation used in [23]. The stress intensity factors for the coalesced cracks are obtained based on a traditional fracture mechanics analysis of the stress intensity factor at the tip of crack subjected to concentrated forces [60]. Using this approach, the effective stress intensity factors for the pattern-1, pattern-2, pattern-3, pattern-4 and pattern-5 coalesced cracks are, respectively:

$$K_{\mathrm{I1}} = \frac{2s\tau\cos\phi}{\sqrt{\pi(0.27s + l_1 1 + \frac{l'}{2})}}\left[\sqrt{\frac{l_1+l}{l}} + \sqrt{\frac{l_1}{l_1+l}}\right] + \sigma_{22}\sqrt{\pi(l_1+\frac{1}{2})} \tag{3.3a}$$

$$K_{I2} = \frac{2s\tau\cos\phi}{\sqrt{\pi(0.27s + l_1' + l_2}}\left[1 + \sqrt{\frac{l_2 + 2l_1'}{l_2}} + \sqrt{\frac{l_2}{l_2 + 2l_1'}}\right] + \sigma_{22}\pi(l_2 + l_1') \tag{3.3b}$$

$$K_{I3} = \frac{2s\tau\cos\phi}{\sqrt{\pi(0.27s + l_3 + l_1 + \frac{l}{2}}}\left[\sqrt{\frac{l_3 + l_1 + l}{l_3 + l_1}} + \sqrt{\frac{l_3 + 2l_1 + l}{l_3}} + \sqrt{\frac{l_3 + l_1}{l_3 + l_1 + l}} + \sqrt{\frac{l_3}{l_3 + l_1 + l}}\right] + \sigma_{22}\sqrt{\pi(l_3 + l_1 + \frac{l}{2})} \tag{3.3c}$$

$$K_{I4} = \frac{2s\tau\cos\phi}{\sqrt{\pi(0.27s + l + l_4)}}\left[\sqrt{\frac{2l + l_4}{l_4}} + \sqrt{\frac{l_4}{2l + l_4}}\right] + \sigma_{22}\sqrt{\pi(l_4 + l)} + \frac{d\tau\cos\phi}{\sqrt{\pi(0.27s + l + l_4)}} \tag{3.3d}$$

$$K_{I5} = \frac{\tau(4s + d)\cos\phi}{\sqrt{\pi(0.27s + l_5)}} + \sigma_{22}\sqrt{\pi l_5} \tag{3.3e}$$

The crack lengths l, l_1, l_1', l_3, l_4, l_5 are shown in figures 3.8-3.10.

3.2.4 Population Update by Poisson Process Statistics

The input parameters that characterize the preexisting defect population in the model are the flaw size distribution and the average flaw density. For simplicity in this work, the flaw size is assumed to be uniform, though the approach can be generalized to a distribution of flaw sizes. Since the PR model discussed in chapter 1 does not consider crack coalescence, the flaw density remains constant. In the current work, the flaw density (interchangeably referred as crack density) evolves, due to coalescence of individual cracks. This evolution of crack population with each load step is tracked

using a probabilistic approach.

The coalescence model includes the patterns of coalescence described in the previous section. The fraction of cracks that coalesce at a given load step is estimated using Poisson process statistics. The Poisson process refers to a collection of points that are randomly located in a space, with locations completely independent of one another. The Poisson process can represent effectively the random locations of objects (e.g. trees in forest, defects in a material domain). Assuming that crack locations are independent of each other, their occurrences in space can be described by a Poisson process. The number of occurrences in a Poisson process has the following probability mass function:

$$P[N = n] = \frac{\lambda^k}{n!} e^{-\lambda} \tag{3.4}$$

Where λ is the parameter of the Poisson distribution, which represents the average number of occurrences. Equating the cracks in a domain to a Poisson process, the probability of a crack occurring within a specific region in space is known. Crack coalescence is assumed to be the event that a crack intersects with another flaw in a given load step. For example, in figure 3.11, assume that the crack grows Δl in the current load step. The crack will coalesce with another crack if a flaw is located in the region marked in blue, with area $A = 2s\Delta l \cos\phi$:

$$P_1 = 1 - P(\text{no cracks in area A}) = 1 - e^{-2\eta A}, \tag{3.5}$$

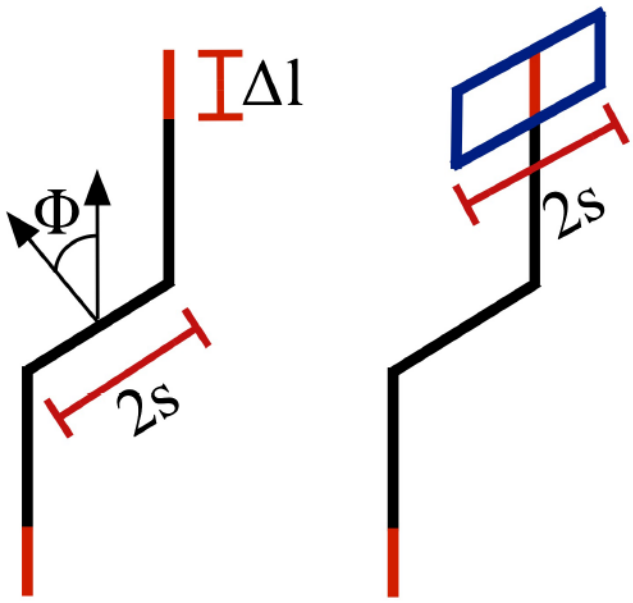

Figure 3.11: The red line on the left figure indicates the wing crack growth increment at a given load step. The area indicated in blue is the region where another flaw might reside to form a pattern-1 coalesced crack.

where η is the average number of flaws per unit area. The updated crack population at the current load step is calculated from this probability of coalescence. For example, the updated crack population due to pattern-1 coalescence is:

$$N = N - 2NP_1 \tag{3.6a}$$

$$N_1 = N_1 + NP_1 \tag{3.6b}$$

where N is the updated density of single cracks after the fraction $2P_1$ have merged and therefore have become a pattern-1 crack, and N_1 is the updated density of the pattern-1 coalesced cracks. The factor of 2 in the equation indicates that two cracks merge to form a pattern-1 coalesced crack.

A similar analogy is used for estimating the fraction of cracks that coalesce to form other patterns of coalescence. The probability of coalescence for pattern-2, pattern-3, pattern-4 and pattern-5 coalesced crack families are:

$$P_2 = 1 - e^{-2sN\Delta l_1 \cos\phi} \tag{3.7a}$$

$$P_3 = 1 - e^{-2sN_1\Delta l_1 \cos\phi} \tag{3.7b}$$

$$P_4 = 1 - e^{-dN\Delta l \cos\phi} \tag{3.7c}$$

$$P_5 = 1 - e^{-0.1sN\Delta d \cos\phi} \tag{3.7d}$$

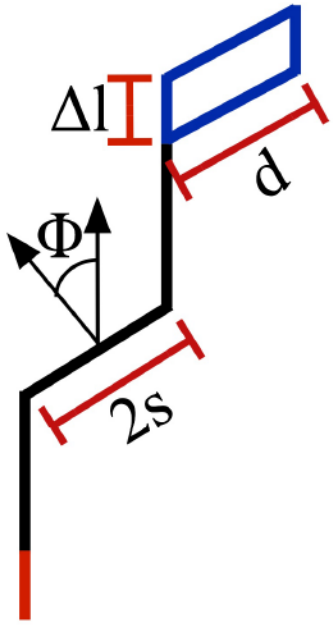

Figure 3.12: The blue region is the area $dN\Delta l\cos\phi$ used in calculating the probability (P_4) of pattern-4 cracks.

P_2 represents the probability that a pattern-1 coalesced crack will merge with a single crack. The crack density N is the density of non-coalesced single cracks. P_3 in equation (3.7b) is the probability of coalescence between two pattern-1 coalesced cracks, and N_1 is the number density of pattern-1 cracks. P_4 is the probability of coalescence of two single cracks based on shear cracks forming between the tip of the wing cracks that are a distance d apart from each other. In other words, P_4 estimates the probability that another wing crack tip will be in the area $dN\Delta l\cos\phi$ (see figure 3.12).

P_5 estimates the probability of coalescence of two single cracks to form a pattern-5 coalesced crack. Δd in equation (3.7d) is the length increment of the shear crack at a given load step whereas $0.1s$ is the height of the approximate area where another

flaw might reside to form the pattern-5 coalesced crack.

The updated population for each coalesced and single crack families is calculated using their respective probability of coalescence. The updated population for the crack families are:

$$N_2 = N_2 + N_1 P_2 \tag{3.8a}$$

$$N_3 = N_3 + N_1 P_3 \tag{3.8b}$$

$$N_4 = N_4 + N P_4 \tag{3.8c}$$

$$N_5 = N_5 + N P_5 \tag{3.8d}$$

$$N = N - 2NP_1 - N_1 P_2 - 2NP_4 - 2NP_5 \tag{3.8e}$$

$$N_1 = N_1 - N_1 P_2 - 2N_1 P_3 \tag{3.8f}$$

The population of the single crack family N is updated by subtracting the fraction of single cracks that merged to create coalesced cracks. Similarly, the population of pattern-1cracks N_1 is also updated by subtracting the fraction of cracks that merge to create pattern-2 and pattern-3 cracks. The populations for patterns $1-5$ are all updated by adding newly coalesced cracks.

3.2.5 Incorporating Microscale Cracks into Macroscale Damage

The macroscopic strain softening behavior observed in brittle materials is due to the growth of microcracks. Therefore, information about the microcracks informs the macroscale effective constitutive response of the material. The damage models proposed by many researchers in the past [27], [46], [22], [26], [47], [48] incorporate the microstructural features into internal state variables, such as damage. The current work uses the scalar crack density parameter or damage Ω for a 2D solid defined in [23]:

$$\Omega = \frac{1}{A} \sum_{i=1}^{N_{\text{cracks}}} l_i^2 \tag{3.9}$$

where N_{cracks} is the number of cracks in the 2D domain of area A and l_l is the length of each crack. For a uniform crack length l, this damage can be restated as:

$$\Omega = \eta l^2 \tag{3.10}$$

where η is calculated as $\frac{N_{\text{cracks}}}{A}$. Equivalently the damage parameter for a medium with multiple crack families is expressed as:

$$\Omega = \sum_{i=1}^{N_{\text{family}}} N_i l_i^2 \tag{3.11}$$

where the N_{family} is the number of crack families in the medium and N_i is the crack density for each individual crack family. In the crack coalescence model, the crack families include non-coalesced and coalesced cracks for all patterns with different underlying dimensions. The micro-scale information is upscaled into macroscopic effective properties using the damage-compliance relationship in equation (1.9b) (see chapter 1 for details).

The step-by-step methodology of the crack coalescence model in the context of the PR model (see chapter 1) can be summarized as:

- Use the global stress at the previous load step to calculate the local stress at the current load step using the effective medium approach in [23]
- Calculate the crack growth rate for all the coalesced and non-coalesced crack families using equation (3.1)
- Update the crack length for each crack family as $l(t_{\text{i+1}}) = l(t_{\text{i}}) + \dot{l}\Delta t$
- Calculate the probability of coalescence for each coalescence pattern using equations (3.5)-(3.7)
- Update the crack population using equation (3.8)
- Calculate the global damage Ω using equation (3.11)
- Update the stress rate using equation (1.10) and update the global stress

- Return to the first step unless $\Omega \geq \Omega_{max}$. Following the PR model [23] the maximum damage level Ω_{max} that the material can sustain is assumed equal to 0.5.

3.3 Model Validation via Finite Element Analysis

While the coalescence model is consistent from the perspective of retaining a statistically consistent progression of damage, there is some physical inconsistency in using the self-consistent approach. The self-consistent approach described in the PR model assumes that the cracks are far enough apart to assume that each crack resides in an undamaged ellipse. However, in order for 2 cracks to interact as shown in figure 3.5 the crack tips must interact before coalescence occurs. If explicit interactions are considered, as described in [5], the effective traction acting on a crack will be influenced by neighboring cracks. The coalescence model in the context of the self-consistent model assumes that cracks instantaneously transition from isolated cracks to fully merged cracks. This assumption is studied further in this section.

The assumption of instantaneous coalescence is taken to be approximately valid if two neighboring crack tips experience a sharp increase in the crack growth rate as a result of the crack interactions. This is assessed through a Finite Element (FE) model in which two single cracks with varying tip spacings are studied. In the finite

element study, it is assumed that the microstructure is periodic and each periodic unit contains a single microcrack, so that the RVE consists of a single microcrack. A pair of microcracks is modeled, assuming periodic boundary conditions (see figure 3.14). A series of FE analyses are performed varying the crack spacings and crack lengths. The wing crack itself is modeled using a contact pair at the flaw surfaces (for details see [4]). The varying input parameters in the simulations are the normalized flaw sizes ($\frac{2s}{L}$) and normalized wing crack length ($\frac{2l}{L}$), where $2L$xL is the size of the model. Since the simulation is performed with varying normalized crack length, the stress contour shown in figure 3.14 will change as the two crack tips approach each other. The change in the crack growth rate resulting from this interaction can be predicted by considering the change in the stress intensity factor or the change in the energy release rate of the cracks. Figure 3.15 shows the change in the J-integral and the stress intensity factor K_I for two wing crack tips, as a function of the normalized crack length. Since the simulations are done for a series of normalized crack length l_n, both the J integral and K_I are calculated at the inner crack tips (tips 2 and 3 in figure 3.14). Initially K_I decreases as the crack grows, as a higher crack driving force is required for further opening of the relatively longer crack. At some normalized crack length greater than 0.7 there is an increase in K_I until the normalized length is approximately 1.1. When this normalized length is equal to 1, this represents the situation in which the two crack tips begin to overlap. Since K_I is related to crack growth rate (equation (3.1)) there will be a sharp increase in crack growth rate as well. These results suggest that

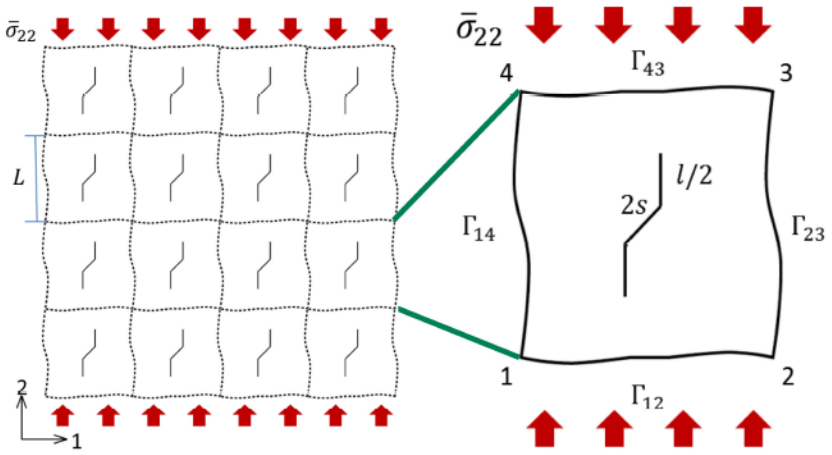

Figure 3.13: A periodic microstructure represented by a unit cell containing a single microcrack, subjected to periodic boundary condition. The figure is obtained from [4]

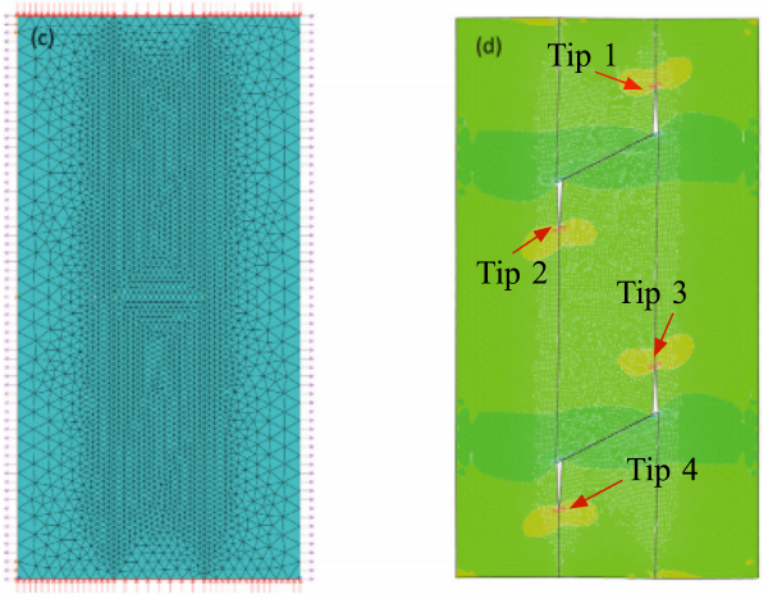

Figure 3.14: The ABAQUS FE mesh (left), along with the predicted distribution of lateral stress σ_{22} (right). The figure is obtained from [4]

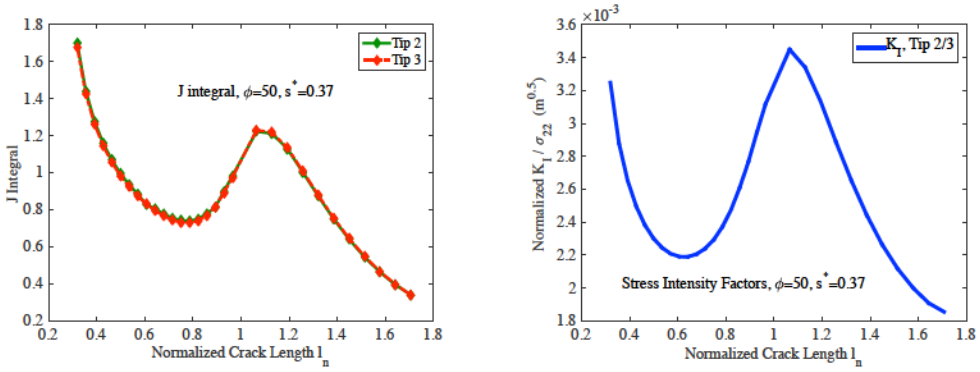

Figure 3.15: The J integral (left) and the mode-I stress intensity factor K_I (right) for crack tip 2 and crack tip 3 in figure 3.14, as a function of normalized crack length l_n. Both the J integral and K_I decrease with increasing crack growth for small crack length. As the two crack tips approach each other, the J integral and K_I both increase sharply.

the cracks accelerate under interaction, supporting the assumption that the cracks approximately transition from single cracks to coalesced cracks instantaneously.

3.4 Model Validation via Analytic Approch

The FE model analysis suggests that the interaction of two crack tips in close proximity promotes mode-I crack growth in both cracks. This increase in crack growth speed is also supported by analytical models of periodic straight cracks described in [5]. This model predicts the effective mode-I and mode-II stress intensity factors due to crack interaction for an array of straight cracks. The results from the model also confirm that the dominant mode of cracking in the wing crack model under uniaxial compression is mode-I crack growth, as assumed in the FE model.

Deng and Nemat-Nasser's [5] model for crack interaction uses a pseudo traction

to model a periodic array of loaded cracks subjected to far-field loading. Figure 3.16 shows how the mode-I and mode-II stress intensity factors change with a varying ratio of crack length to spacing, for a fixed angle β. K_I reaches its peak value when α is 10^o and the $\frac{l}{w}$ ratio is 0.9. A large $\frac{l}{w}$ ratio with a smaller α represents two overlapping crack tips. Figure 3.16 shows that when the crack tips overlap each other, the mode-I stress intensity factor is increased due to interaction. A similar trend is also predicted for mode-II stress intensity factors, though for a smaller range of angles. The results verify that the interaction promotes mode-II as well as mode-I crack growth, by increasing the stress intensity factors.

The proposed coalescence model addresses mode-I crack growth and neglects the mode-II crack growth in wing crack models [16]. A simple analysis based on the results Deng and Nemat-Nasser [5] compares the effect of mode-I and mode-II stress intensity factors. Figure 3.17 shows that for α between $25^o - 45^o$ and $\frac{l}{w}$ between $0.5 - 0.9$ K_I is much larger than K_{II}. This indicates that mode-I crack growth is dominant mechanism in this range, which is consistent with the values in the case of overlapping wing cracks under axial splitting. These results suggest that the nature of coalescence is consistent with the analytical model.

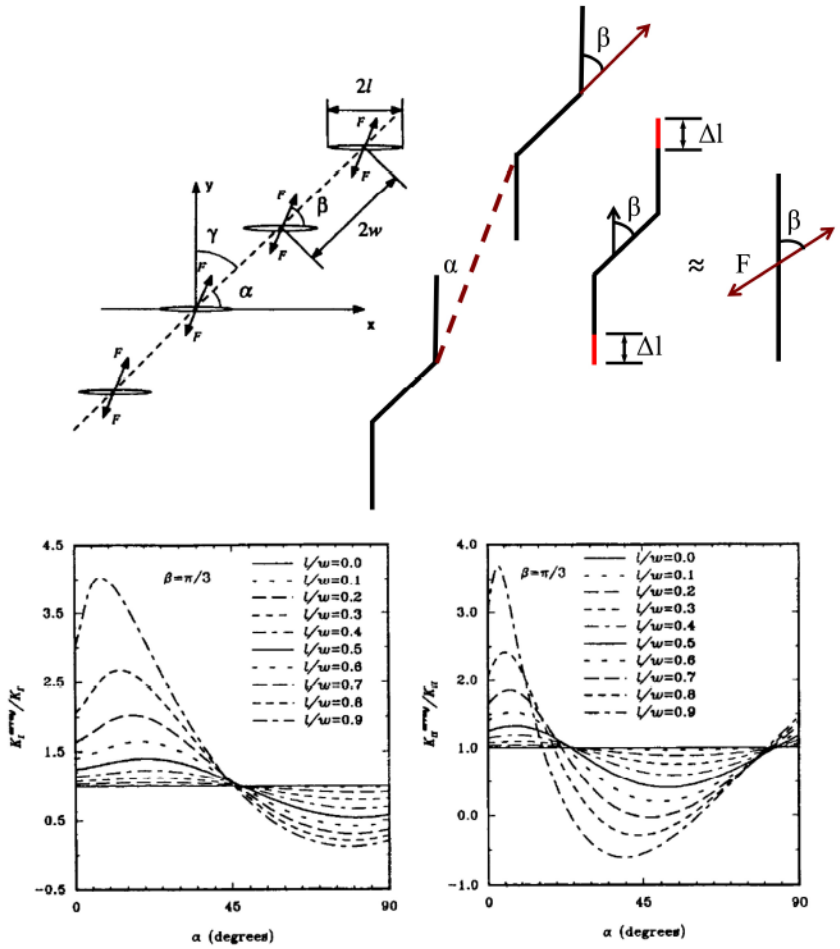

Figure 3.16: The loaded parallel crack array with an equal spacing of $2w$. The loaded cracks can be represented as the wing cracks. α is the angle between the line joining the cracks and the crack faces. β is the angle between the crack face and the direction of force acting on the crack. The wing cracks representing the loaded cracks are also shown with angle α and β. The figures at the bottom shows normalized K_I and K_{II} with respect to the crack length to spacing ratio $(\frac{l}{w})$ ration. $\beta = \frac{\pi}{3}$ is a reasonable assumption for flaw inclinations that lead to wing cracks. The figure is obtained from [5]

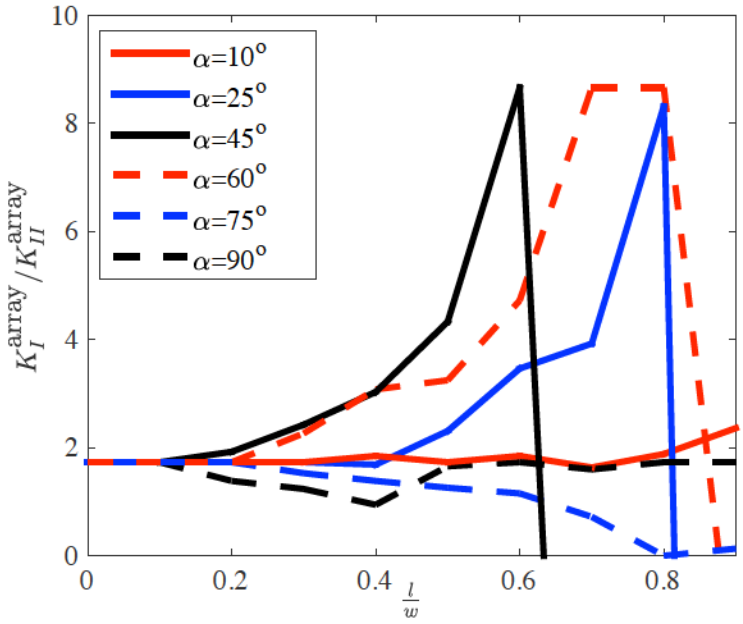

Figure 3.17: Comparison of K_I and K_{II} with respect to $\frac{l}{w}$ ration for different values of α.

3.5 Effect of Crack Coalescence in Dynamic Strength

The formation and progression of damage as the material reaches its peak stress is attributed to rapid merging of cracks, which results in a significant decrease in the dynamic strength of the material. Simulations using the proposed crack coalescence model have been performed to predict the constitutive response of the material under dynamic loading. In particular, the loading condition is dynamic uniaxial compression. The material properties used here are consistent with boron carbide, (see table 3.1). Simulations are performed, varying both flaw density and strain rate, pre-

E (GPa)	ν	K_{Ic} (MPa.m$^{0.5}$)	ρ (kg/m^3)	μ	Shear Strength (GPa)
453 [84]	0.16 [84], [85]	2.5 [85]	2520 [86]	0.8 [87]	8.7 [84]

Table 3.1: Material properties used in simulations for boron carbide.

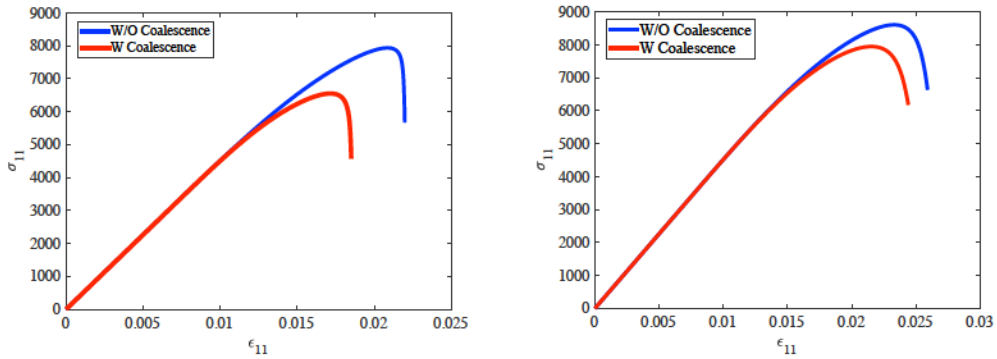

Figure 3.18: Comparison of stress-strain response at a flaw density of $10^9\, m^{-2}$. The strain rate for the left plot is $10^5\, s^{-1}$ while the strain rate for the right plot is $10^6\, s^{-1}$. The blue line in both plots indicates the response without explicit coalescence and the red line indicates the response with coalescence.

dicting the effective constitutive response and sensitivity of coalescence to the initial flaw populations. The flaw size s is assumed to be $10\, \mu m$.

Figure 3.18 shows the predicted stress-strain response at two different strain rates for a fixed flaw density of $10^9\, m^{-2}$. The results for the two strain rates show a significant decrease in peak stress when considering coalescence. The coalesced crack families exhibit a higher crack growth speed at each load step so that they add significantly to damage at higher loads, reducing the total stress levels. The decrease in peak stress at the strain rate of $10^6\, s^{-1}$ is smaller compared to the decrease in peak stress at the strain rate of $10^5\, s^{-1}$. The results at the higher strain rate shows a higher

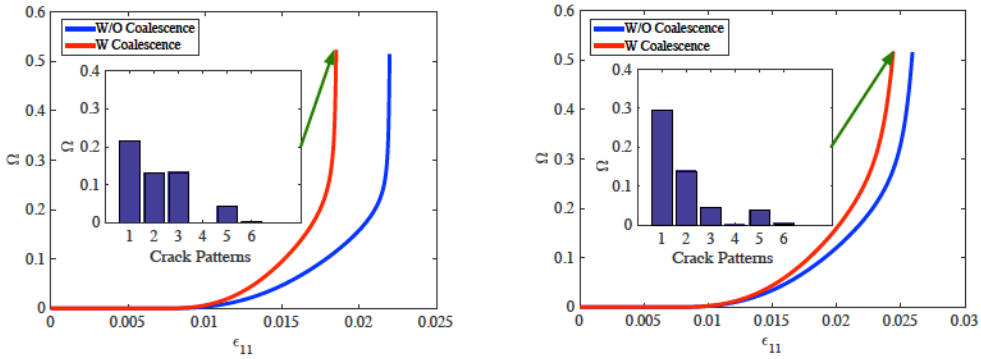

Figure 3.19: The left figure shows the damage (Ω) vs. strain (ϵ_{11}) at a strain rate of $10^5\, s^{-1}$ while the right figure shows damage vs. strain at a strain rate of $10^6\, s^{-1}$. The bar plots in both figures show the relative damage contribution by the different crack families. Family-0 is the single crack family. The green arrow indicates the time step at which the relative damage contribution is plotted. The flaw density in both cases is $10^9\, m^{-2}$.

peak stress. The increase in peak stress at higher loading rates is due to the inertial effect associated with the dynamic crack propagation. The cracks in the medium cannot propagate faster than the Rayleigh wave speed (C_R), so damage growth is limited while the stress and strain continue to grow at a rapid rate.

Damage associated with the coalesced crack families can be analyzed by considering the damage vs. strain plot in figure 3.19. The blue line shows the damage vs. strain plot without explicit coalescence while the red line shows the damage vs. strain plot with explicit coalescence. The damage threshold is reached at a much lower strain when coalescence is considered. The inset bar plots for both strain rates demonstrate the relative contribution of different crack patterns to damage. The damage contributed by a given crack pattern is a function of both the number of cracks in that pattern and the crack length associated with that pattern. For both

strain rates, the most damage is contributed by the single crack family (pattern-0 in figure 3.19) followed by the pattern-1 and pattern-2 crack families. The contribution by pattern-3 and pattern-5 crack families are small. The coalesced crack families include large cracks but there are fewer of them than non-coalesced cracks, so they contribute less to damage. For this reason, pattern-3 cracks and pattern-5 (see figure 3.19) contribute negligibly to damage due to their very low density. However, the damage contribution by pattern-4 crack family is relatively higher at the strain rate $10^6\ s^{-1}$ since the population of this pattern of cracks are based on the single crack family. The small contribution of the shear crack patterns to damage is consistent with experimental observations, which do not show this pattern frequently [31]. The single crack family at higher strain rate is more dominant than the lower strain rate. The damage contributed by the pattern-1 cracks are similar for both strain rates, but damage associated with pattern-2 cracks is significantly smaller at the higher rate, due to limited crack growth rate associated with these larger cracks.

The simulation results shown in figure 3.20 show the effect of further increasing the strain rate. The peak stress decreases when coalescence is considered in both cases, but the reduction is smaller at the higher strain rate of $3 * 10^6\ s^{-1}$. Again the peak stress for both coalescence and non-coalesced cases is higher at the higher strain rate. The increase in stress carrying capacity at higher loading rates is due to the inertial effect associated with dynamic crack propagation. This maximum crack speed is bounded by C_R (equation (3.1)). Therefore, the damage evolution rate is

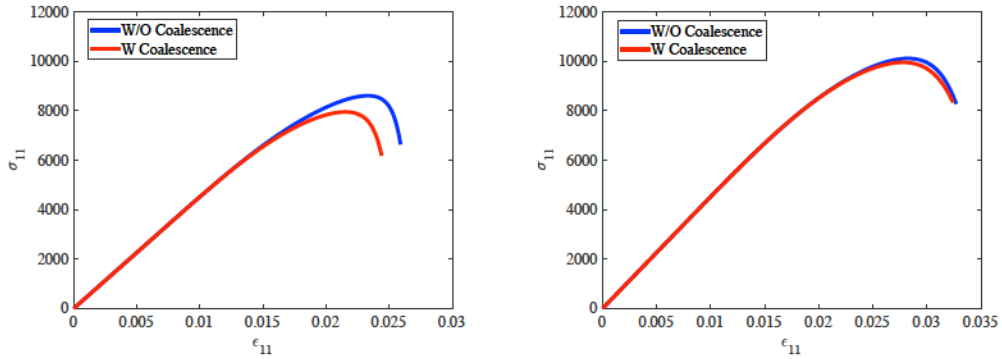

Figure 3.20: The left figure shows stress-strain response with and without explicit coalescence at a strain rate of $10^6\,s^{-1}$ while the right figure shows the stress-strain response with and without explicit coalescence at a strain rate of $3*10^6\,s^{-1}$. The blue line shows the stress-strain response without coalescence and the red line shows the response with explicit coalescence for both strain rates. The flaw density is $10^9\,m^{-2}$.

limited, allowing the loading to continue to increase more rapidly than the damage. The material shows a higher dynamic strength due to this low damage evolution at higher rates. When cracks coalesce, the same trend of increased dynamic strength holds true. In addition, the effect of coalescence is also less at higher strain rates as the crack growth speed limitation on the coalesced crack families inhibit their effect on damage. This effect is visible at the strain rate $3*10^6\,s^{-1}$ where there is almost no effect of coalescence. Figure 3.21 shows that the damage evolution at a strain rate of $10^6\,s^{-1}$ is slightly slower than the case in which no coalescence was considered. Under the strain rate $3*10^6\,s^{-1}$, the damage evolution with coalesced crack families is almost the same as the single crack family. The effect of coalescence is less significant at a rate of $10^6\,s^{-1}$ and has little significance at a rate $3*10^6\,s^{-1}$. The highest fraction of damage is contributed by the single crack family (pattern-0) for both strain rates. The coalesced crack patterns (pattern-1 and pattern-2) contribute more to damage

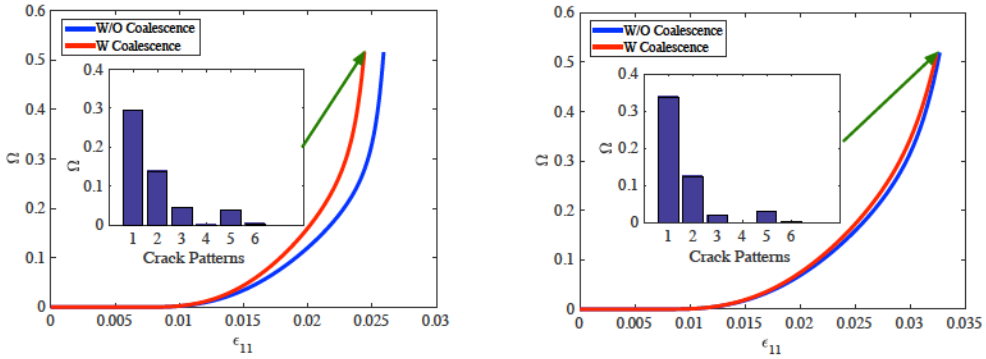

Figure 3.21: The left figure shows the damage vs. strain plot with and without coalescence at a strain rate of $10^6\,s^{-1}$ and the right plot shows the same at a strain rate of $3 * 10^6\,s^{-1}$. Both plots contain the relative damage contributions of the crack patterns at the last load step.

evolution at the lower rate than they do at the higher strain rate. Pattern-4 cracks have some contribution in global damage.

Simulations are also done to predict the role of flaw density on the stress-strain response shown in figure 3.22 for a fixed strain rate of $10^5\,s^{-1}$. The decrease in the predicted peak stress with coalescence is higher at larger flaw densities. Since cracks are more closely spaced at higher flaw densities, the probability of coalescence is higher, resulting in a higher fraction of coalesced cracks (see figure 3.23). With reduced flaw densities, the fraction of coalesced cracks decreases. The bar plots show that the damage evolution due to coalesced crack families is significant at the largest flaw density.

Similar results at a fixed strain rate of $10^6\,s^{-1}$ are consistent with the previous results (see figure 3.24). The effect of coalescence becomes small at the lowest flaw density under this higher strain rate. The damage vs. strain plots (see figure 3.25)

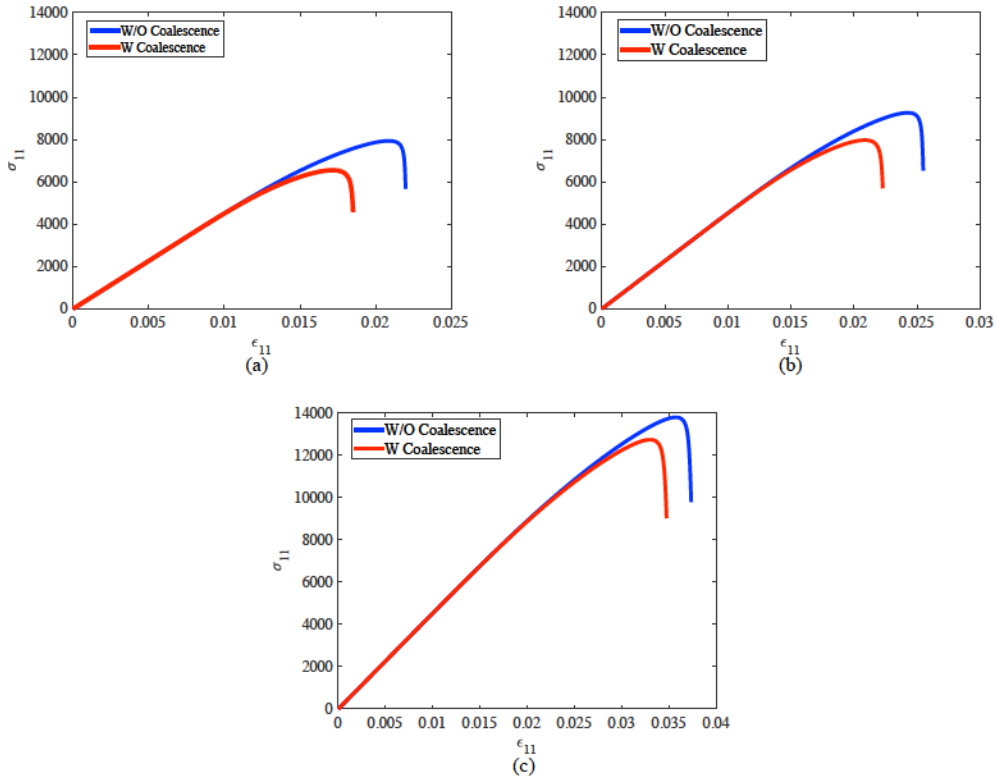

Figure 3.22: (a) Stress-strain response for flaw densities of $10^9\,m^{-2}$, (b) $5 * 10^8\,m^{-2}$ and (c) $10^8\,m^{-2}$ at a strain rate of $10^5\,s^{-1}$. The blue lines represent the response without coalescence while the red lines represent the response with coalescence.

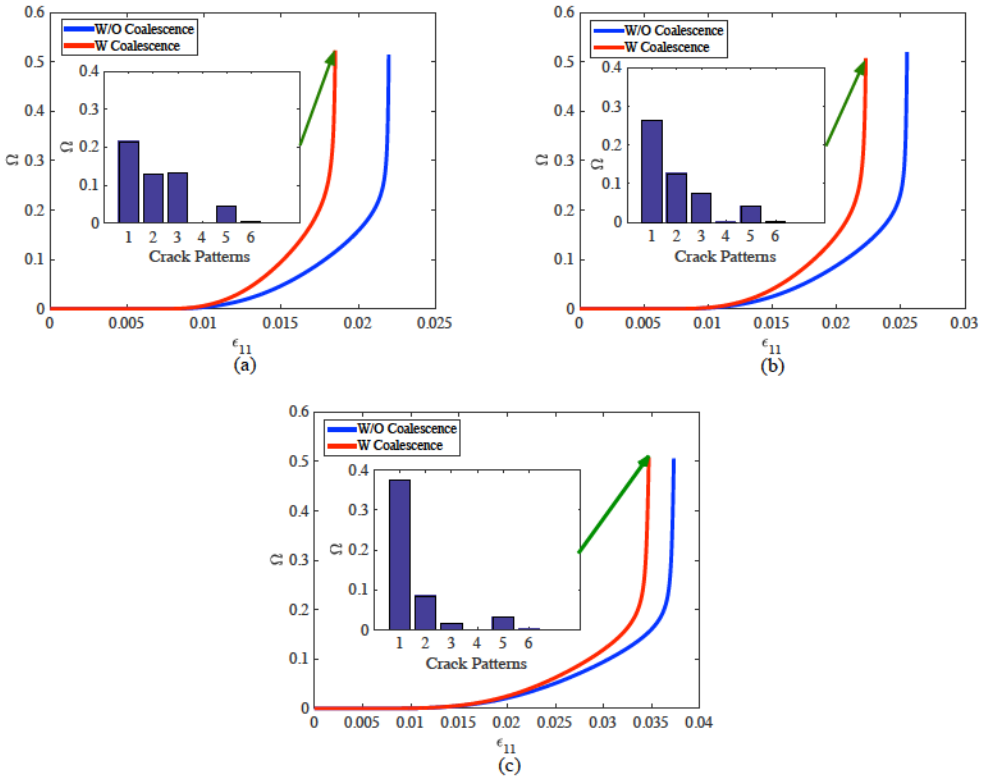

Figure 3.23: (a) Damage vs. strain plots at flaw densities $10^9\,m^{-2}$, (b) $5 * 10^8\,m^{-2}$ and (c) $10^8\,m^{-2}$ under the strain rate of $10^5\,s^{-1}$. The blue line is the response without coalescence while the red line is the response with coalescence. The bar plots associated with each damage vs. strain plot represent the relative contribution of damage from different crack patterns at the given flaw density and strain rate.

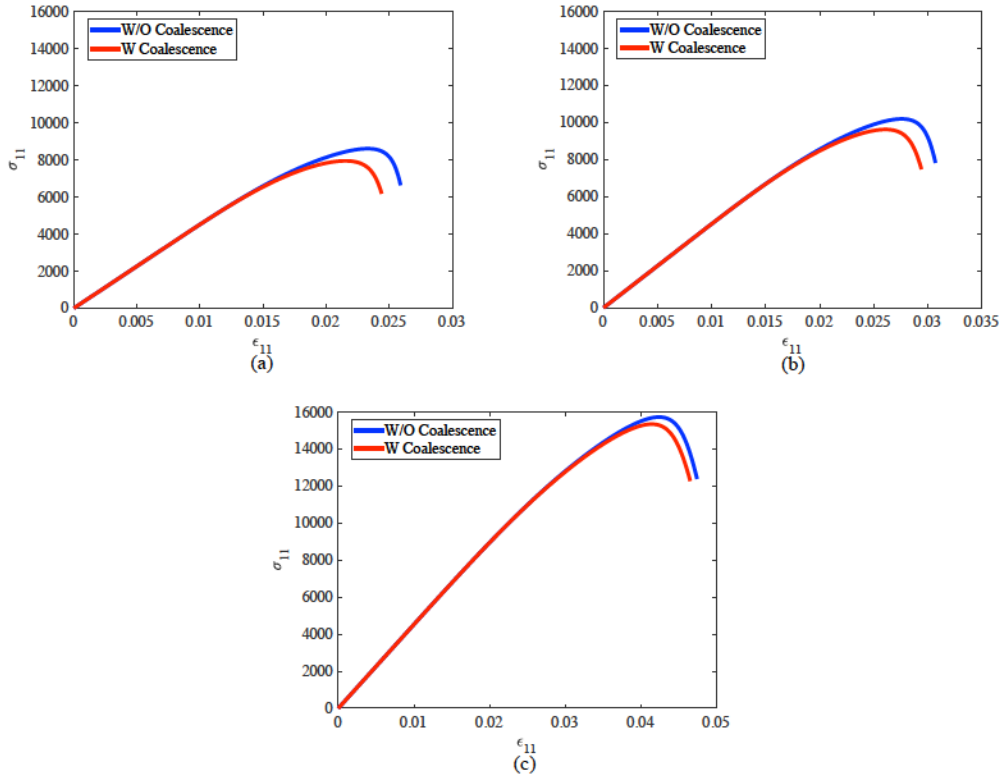

Figure 3.24: (a) Stress-strain response for flaw densities of $10^9\,m^{-2}$, (b) $5 * 10^8\,m^{-2}$ and (c) $10^8\,m^{-2}$ at a strain rate of $10^6\,s^{-1}$. The blue lines represent the response without coalescence while the red lines represent the response with coalescence.

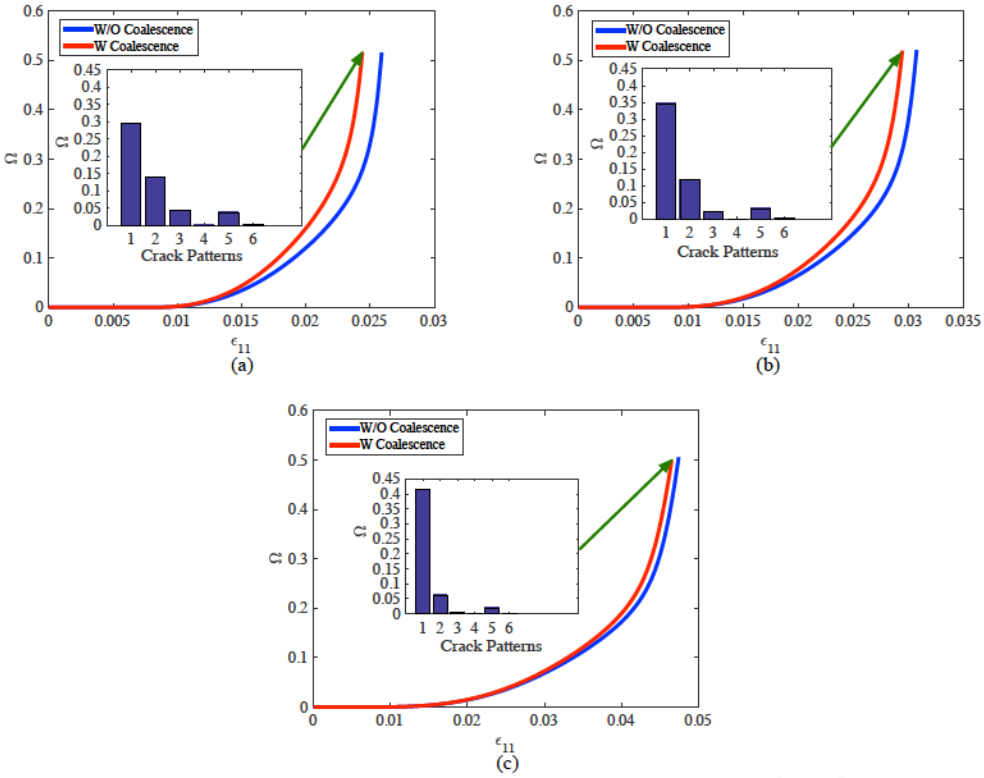

Figure 3.25: (a) Damage vs. strain plots at flaw densities $10^9\,m^{-2}$, (b) $5 * 10^8\,m^{-2}$ and (c) $10^8\,m^{-2}$ under the strain rate of $10^6\,s^{-1}$. The blue line is the response without coalescence while the red line is the response with coalescence. The bar plots associated with each damage vs. strain plot represent the relative contribution of damage between crack patterns at the given flaw density and under a higher strain rate than that shown in figure 3.23.

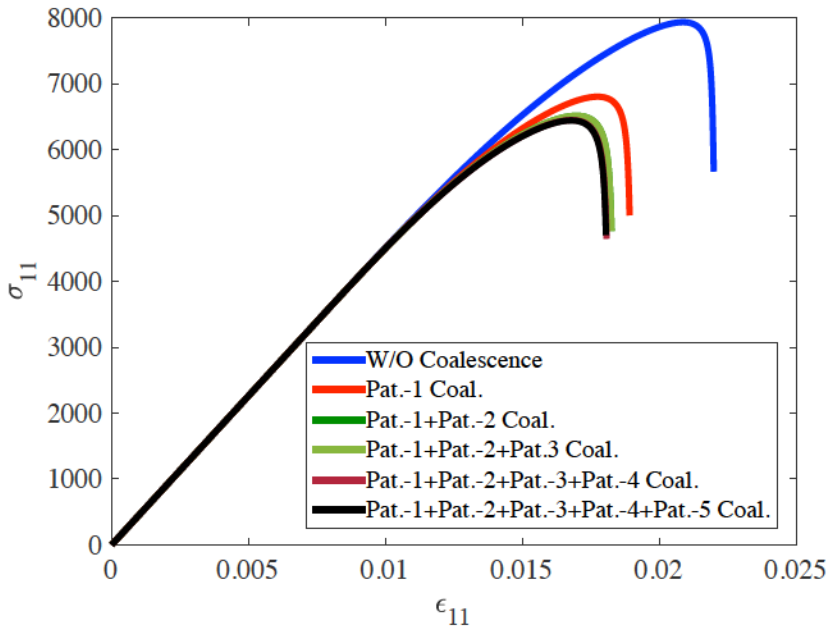

Figure 3.26: The predicted stress-strain response assuming different patterns of coalescence. The blue line on top is the response without coalescence. The lines below the blue line represents the effect of progressively adding new patterns of coalescence.

show slower damage growth with an increase in strain rate. The bar plots associated with the damage vs. strain plots show that the highest damage contribution is from the single crack pattern (pattern-0). Pattern-1 cracks produce some damage, but the contribution of other coalesced crack families is not significant.

The effect of coalesced crack families is demonstrated by the measure of relative damage associated with them. The reduction in dynamic strength is also shown in figure 3.26 by progressively adding one new crack pattern at a time. The red line represents the response when only pattern-1 coalesced cracks are present in the medium. The peak stress reduces significantly with this crack pattern. There is further reduction in peak stress when pattern-2 coalescence is added. The effect of

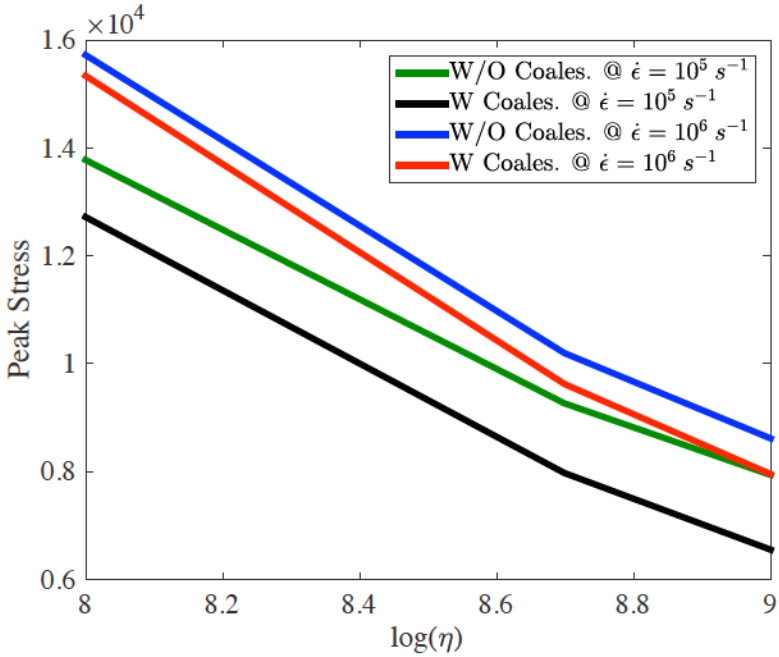

Figure 3.27: The change in peak stress with respect to flaw density. The blue line and the green line represent the change in peak stress without considering coalescence at two different strain rates ($10^5\ s^{-1}$ and $10^6\ s^{-1}$). The red line and the black line represent the change in peak stress considering coalescence at the same strain rates.

other coalesced cracks is negligible and very little further reduction in the response occurs due to those crack patterns.

The results demonstrating the change in peak stress due to coalescence at different flaw densities and strain rates highlight the effect of coalescence on dynamic strength. Figure 3.27 shows the reduction in peak stress with increasing flaw densities at two strain rates. At a fixed strain rate, the peak stress has the lowest magnitude at the highest flaw density. The reduction is significant when comparing the peak stress with coalescence to the peak stress without coalescence. The reduction in peak stress due to coalescence is smaller at higher rates. The most significant reduction in peak

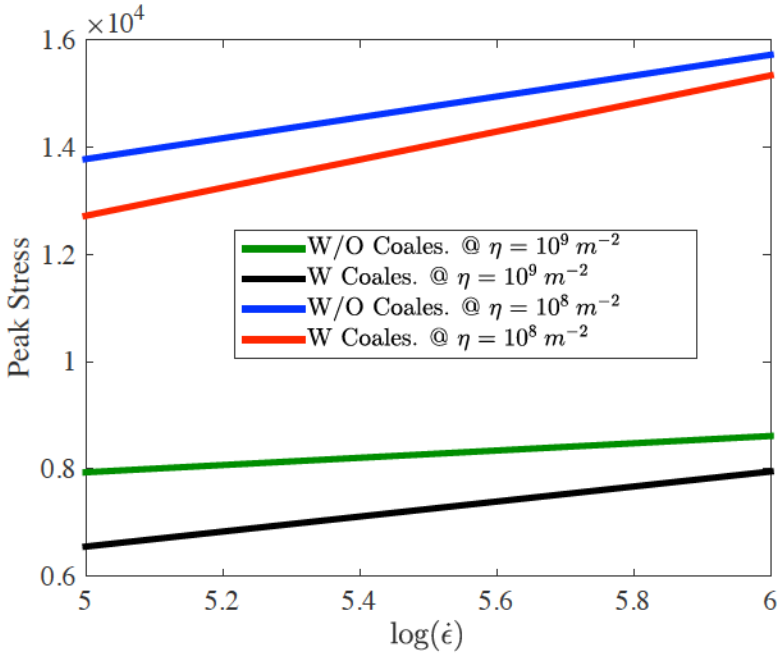

Figure 3.28: Peak stress vs. log ($\dot{\epsilon}$) plot at flaw densities of $10^9\ m^{-2}$ and $10^8\ m^{-2}$. The blue line and the green line represent the response without coalescence whereas the red line and the black line represent the response with coalescence.

stress due to coalescence is observed at higher flaw densities. The magnitude of peak stress will be approaches the magnitude of peak stress without coalescence increasing strain rate.

Figure 3.28 shows change in peak stress with varying strain rate for two fixed flaw densities. The lower two lines in figure 3.28 show that the predicted peak stress increases with an increasing strain rate and that the results from the coalescence model slowly approach the peak stress without coalescence. At a lower flaw density (represented by the two upper lines) the peak stress value is closer to the peak stress value without coalescence at a relatively lower strain rate, since the effect of coalescence is less at lower flaw density.

3.6 Summary

A micromechanics-based model is proposed to incorporate the micro-crack coalescence in brittle materials at high strain rate loading. Different patterns of coalescence of cracks are incorporated as inclusions in the medium to homogenize the effect of coalescence into macroscale effective properties. The amount of coalescence is handled by a statistical approach which determines the probability of coalescence by using Poisson process statistics. The crack population is updated using the probability of coalescence at each load step. The effect of coalescence is incorporated into the macro-scale stress-strain response through the scalar damage parameter which is a function of crack length. The effect of coalescence can be summarized as:

- Coalescence predicts a significantly reduced peak stress under uniaxial compression.
- The reduction in peak stress is more significant at lower strain rates. With increasing strain rate, the effect of coalescence decreases.
- The reduction in peak stress is more significant at higher flaw density. If the flaw density decreases, the effect of coalescence decreases.
- Pattern-1 coalescence plays a significant role in the reduced peak stress and pattern-2 coalescence plays a lesser role. The other patterns of coalescence do not have any significant effect on the constitutive response at any strain rate and flaw density studied here.

The coalescence model provides a simple solution to the complex crack merging process in brittle materials under high rate loading. However, the computational burden can still be a challenge in case of a lower flaw density and strain rate, since the number of crack families with very small associated probabilities becomes very large. The next chapter will discuss an efficient solution which can predict the response using single effective coalesced cracks to represent multiple crack families.

Chapter 4

Crack Coalescence Model: An Efficient Approach

The micromechanics-based crack coalescence model discussed in chapter 3 predicts the dynamic stress-strain response of a brittle material with a flaw population that interacts randomly. The model works well for higher strain rate loading on materials with a high flaw density, in which cases the damage grows relatively quickly and crack coalescence occurs with a reasonable probability. However, if the coalescence process is slower due to a lower fraction of coalesced cracks and/or a lower strain rate, it takes many load steps to reach the damage threshold associated with material failure. Because the model in chapter 3 generates new crack families for each pattern at every load step, the required memory to track that large number of crack families becomes prohibitive.

To address this issue, an alternative approach is proposed to replace all the crack families within a particular crack pattern by a single equivalent crack. This approximation introduces some error in the constitutive response, but it reduces the computational burden significantly. This allows for studies that consider a wider range of strain rates and flaw densities, which might be more directly applicable to experimental results. In addition, this coalescence model can be efficiently incorporated into a multi-scale modeling framework for brittle ceramics. This is demonstrated here by implementing the model into the mechanism-based TR model (see chapter 1). The equivalent crack approach is necessary for this implementation, since computational efficiency is required for a computationally demanding constitutive model like TR mode that captures multiple mechanisms in a multi-scale context.

This chapter briefly discusses the efficient implementation of the crack coalescence model. Numerical results are presented to compare the trade-off between efficiency and accuracy. The efficient approach only accounts for pattern-1 and pattern-2 coalesced crack families, since these crack families play the dominant role in stress-strain results (see chapter 3 results). The implementation of this effective coalescence model in the TR model is discussed. Numerical results using TR model with crack coalescence are presented.

4.1 Computational Efficiency Consideration

The process of coalescence is outlined by the schematic diagram as shown in figure 4.1. In summary, a new pattern-1 coalesced crack family forms at each load step, and a number of pattern-2 and pattern-3 crack families are also formed at each load step (see figure 4.1). Therefore, a large number of internal state variables associated with all of these crack families need to be tracked as the loading progresses.

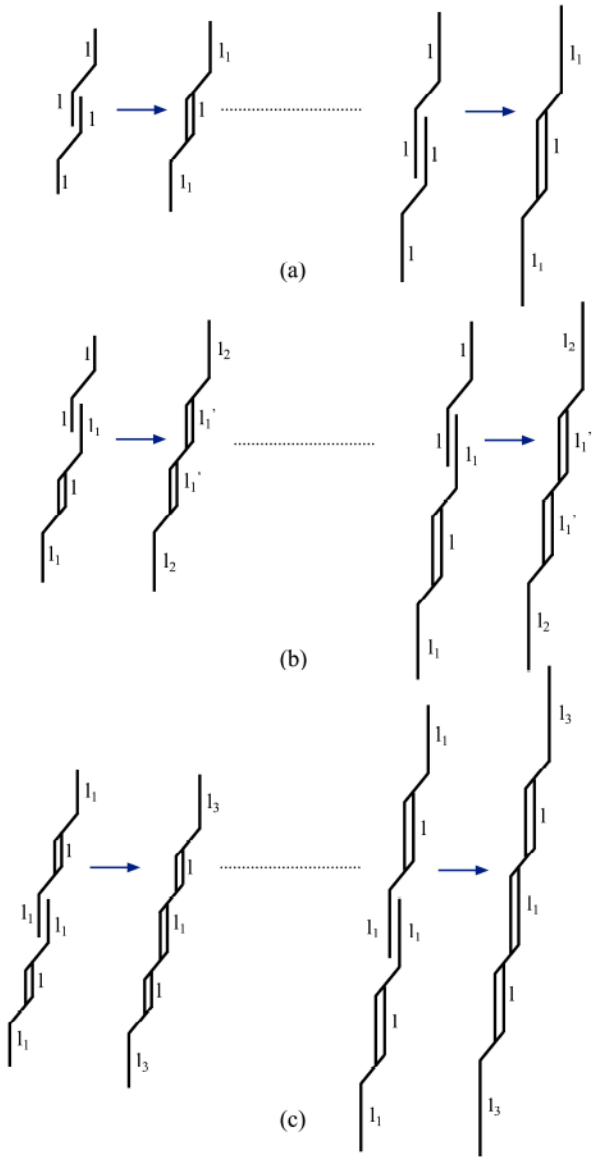

Figure 4.1: Illustration of pattern-1, pattern-2 and pattern-3 coalesced cracks: (a) Two single cracks merge to form a pattern-1 crack. A new coalesced crack family is formed at each load step. The length l_1 is the wing crack length associated with each pattern-1 coalesced crack family. The distance l between the flaw surfaces is different for the newly formed pattern-1 crack at each load step. (b) A single pattern-1 crack is merged with a single crack to form a pattern-2 crack. The length l_2 is the wing crack length associated with this pattern-2 coalesced crack family. The distance l_1' is different for each newly coalesced pattern-2 crack family. (c) Two pattern-1 cracks merge to form a pattern-3 crack, where l_3 is the wing crack length and l and l_1 represents the spacings between the flaw surfaces.

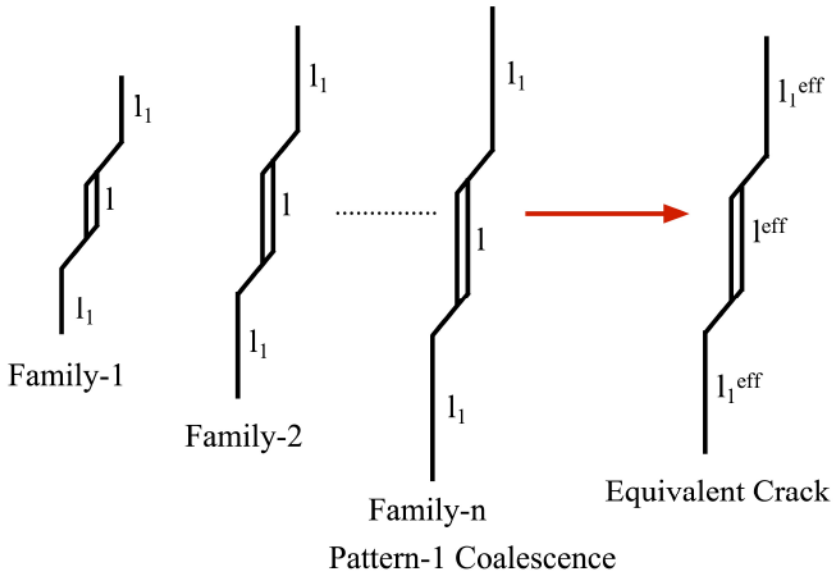

Figure 4.2: An illustration of equivalent crack model. Pattern-1 coalescence is shown in the figure as an example. A new pattern-1 crack family is forming at each load step. All pattern-1 cracks are replaced by an equivalent crack.

4.2 Equivalent Coalescence Model

A new model (referred as the equivalent coalescence model hereafter) has been developed to address the computational issues associated with the original coalescence model. The new model aims to represent all the cracks belong to a particular pattern of coalescence by a single equivalent crack. The family of cracks created at each load step for a particular pattern of coalescence will be lumped into this equivalent crack. Only the equivalent crack representing each coalescence pattern will be tracked at every load step. The global damage and stress-strain response are determined solely based on the lengths of these equivalent cracks. The idea is outlined in figure 4.2, which shows the equivalent coalescence model approach for pattern-1 coalescence.

The dimensions of each crack family shown in figure 4.2 differ in part due to the varying distance between the pair of splitting forces acting on the crack. The equivalent crack model replaces these multiple crack families by a single equivalent crack family, containing information about different crack families within pattern-1 coalescence. For the equivalent crack model, the distance between the pair of splitting forces as well as the length of the wing crack is updated at each load step to reflect the addition of a new pattern-1 crack family. An analogous approach is used for pattern-2 coalesced crack families, in which the average distance l_1' is updated along with the wing crack length l_2 (see figure 3.5).

4.3 Formation of Equivalent Crack Families

Since the growth of the individual crack families are not tracked explicitly, care must be taken to ensure that the global stress-strain response using the equivalent crack method will not be significantly different. The attributes of the equivalent cracks representing each pattern of coalescence are updated at every load step, with an effort to minimize the error in the global stress-strain response.

The relevant microstructural feature for this model is the wing crack length, which is upscaled to the macro-scale effective properties by means of the scalar damage parameter. To retain accuracy in the global stress-strain response, the equivalent

crack for a particular pattern should produce the same of damage as that produced by all the crack families that are replaced. In other words, the attributes of the equivalent crack should be updated based on an equal damage criterion, which requires that the damage contribution of the equivalent crack is consistent with the total damage contribution of all the individual crack families in that particular coalescence pattern.

The scalar damage parameter associated with the pattern-1 coalesced crack family is:

$$\Omega_{1\text{ac}} = \sum_{i=1}^{N_{1\text{family}}} N_{1i}\left(\frac{l_i}{2} + l_{1i}\right)^2, \tag{4.1}$$

where $\Omega_{1\text{ac}}$ represents the total damage associated with all the pattern-1 crack families, N_{1i} is the crack density for each family, l_{1i} is the wing crack length for each family and l_i is the distance between the splitting forces. The damage associated with the pattern-1 equivalent crack family is:

$$\Omega_{1\text{eff}} = N_{1\text{eff}}\left(\frac{l^{\text{eff}}}{2} + l_1^{\text{eff}}\right)^2, \tag{4.2}$$

where $N_{1\text{eff}}$ is the crack density for the effective crack family which is computed as $N_{1\text{eff}} = \sum_{i=1}^{N_{1\text{family}}} N_{1i}$, l^{eff} is the distance between the pair of forces and l_1^{eff} is the wing crack length. Since the fraction of cracks that belong to each family of pattern-1 coalescence is represented by a single equivalent crack family, the crack density of the equivalent crack family is set equal to the summation of crack densities associated with the pattern-1 coalesced crack families. Setting actual damage $\Omega_{1\text{ac}}$ equal to the

effective damage $\Omega_{1\text{eff}}$, an approximate expression for l^{eff} is found:

$$l^{\text{eff}} \approx \sqrt{\frac{\sum_{i=1}^{N_{1\text{family}}} N_{1i} l_i^2}{N_{1\text{eff}}}} \tag{4.3}$$

Since l_i and l_{1i} are not saved for every crack family that arose in previous time steps, the only information available at a given load step is the equivalent crack length at the previous load step and the crack length of the new crack family introduced in that load step. Therefore, the damage due to the growth of pattern-1 equivalent crack at load step n is written as:

$$\Omega_{1\text{eff}}^{(n)} \approx \Omega_{1\text{eff}}^{(n-1)} + \Delta\Omega_{1\text{ac}}^{(n)}, \tag{4.4}$$

where $\Omega_{1\text{eff}}^{(n-1)}$ is the damage based on the pattern-1 equivalent crack at time step $(n-1)$ and $\Delta\Omega_{1\text{ac}}^{(n)}$ is the damage associated with the newly formed pattern-1 coalesced crack at the current load step n. The damage at the time step $(n-1)$ is:

$$\Omega_{1\text{eff}}^{(n-1)} \approx N_{1\text{eff}}^{(n-1)} \left[\frac{l^{\text{eff(n-1)}}}{2} + {l_1}^{*\text{eff(n)}} \right]^2, \tag{4.5}$$

where $N_{1\text{eff}}^{(n-1)}$ is the crack density for the pattern-1 equivalent crack family at time step $(n-1)$, $l^{\text{eff(n-1)}}$ is the distance between the pair of splitting forces at load step $(n-1)$ and ${l_1}^{*\text{eff(n)}}$ is the wing crack length at load step n. The current wing crack length ${l_1}^{*\text{eff(n)}}$ is used in the expression in equation (4.5) instead of the wing crack length of the equivalent crack at time step $(n-1)$, since this updated crack length is

calculated calculated using the micromechanics model.

The damage associated with the newly formed coalesced crack family at load step n is:

$$\Delta\Omega_{1ac}^{(n)} = N_1^{(n)}\left(\frac{3l^{(n)}}{2}\right)^2, \tag{4.6}$$

where $N_1^{(n)}$ is the crack density of the newly formed pattern-1 coalesced crack at load step n and l is the wing crack length of the family which is also the distance between the pair of splitting forces at that initial time of coalescence. Combining equations (4.5)-(4.6) the updated wing crack length for the pattern-1 equivalent crack is:

$$l_1^{\text{eff(n)}} = \sqrt{\frac{N_{1\text{eff}}^{(n-1)}}{N_{1\text{eff}}^{(n)}}\left[\frac{l^{\text{eff(n-1)}}}{2} + l_1{}^{*\text{eff(n)}}\right]^2 + \frac{N_1^{(n)}}{N_{1\text{eff}}^{(n)}}\left(\frac{3l^{(n)}}{2}\right)^2} - \frac{l^{\text{eff(n)}}}{2} \tag{4.7}$$

An analogous approach is used for pattern-2 coalescence. The updated wing crack length for the pattern-2 equivalent coalesced crack is written as:

$$l_2^{\text{eff(n)}} = \sqrt{\frac{N_{2\text{eff}}^{(n-1)}}{N_{2\text{eff}}^{(n)}}\left[l_1{}'^{\text{eff(n-1)}} + l_2{}^{*\text{eff(n)}}\right]^2 + \frac{N_2^{(n)}}{N_{2\text{eff}}^{(n)}}\left(l_1'^{(n)} + l_2^{(n)}\right)^2} - l_1'^{\text{eff(n)}}, \tag{4.8}$$

where $N_{2\text{eff}}^{(n-1)}$ is the crack density of pattern-2 equivalent crack family at load step $(n-1)$, $N_{2\text{eff}}^{(n)}$ is the crack density at load step n, $l_1'^{\text{eff(n-1)}}$ is the equal distance between the pair of splitting forces acting on the effective crack (see figure 4.1), $l_2{}^{*\text{eff(n)}}$ is the wing crack length at load step n, $N_2^{(n)}$ is crack density of the newly formed pattern-2 coalesced crack at load step n, $(l_1'^{(n)} + l_2^{(n)})$ is the wing crack length of the newly

formed pattern-2 coalesced crack, and $l_1'^{\text{eff(n)}}$ (see figure 4.1) is the distance between splitting forces at load step n.

The process followed in the micromechanics model with the equivalent crack coalescence model is outlined as:

- Use the global stress at the previous load step to calculate the local stress at the current load step using the effective medium approach in [23]
- Update the distance between the splitting forces of the pattern-1 and pattern-2 equivalent cracks using equation (4.3)
- Calculate the crack growth rate for non-coalesced and coalesced cracks using equation (3.1)
- Calculate the wing crack length for each equivalent crack family as $l(t_{\text{i+1}}) = l(t_{\text{i}}) + \dot{l}\Delta t$
- Calculate the probability of coalescence of pattern-1 equivalent crack using equation (3.5) and for pattern-2 equivalent crack using equation (3.7a).
- Update the crack population of pattern-1 equivalent crack family as $N_{\text{1eff}} = \sum_{i=1}^{N_{\text{1family}}} N_{1i}$ and pattern-2 equivalent crack family as $N_{\text{2eff}} = \sum_{i=1}^{N_{\text{2family}}} N_{2i}$
- Update crack length for pattern-1 and pattern-2 equivalent crack family using equation (4.7) and equation (4.8) respectively

- Calculate the global damage $\Omega_{\text{eff}} = \Omega_{1\text{eff}} + \Omega_{2\text{eff}}$, where $\Omega_{1\text{eff}} = N_{1\text{eff}}\left(\frac{l^{\text{eff}}}{2} + l_1^{\text{eff}}\right)^2$ and $\Omega_{2\text{eff}} = N_{2\text{eff}}\left(l_1{}'^{\text{eff}} + l_2^{\text{eff}}\right)^2$

- Update the stress rate using equation (1.10) and update the global stress

- Return to the first step unless $\Omega \geq \Omega_{\text{max}}$. Following the PR model [23] the maximum damage level Ω_{max} that the material can sustain is assumed equal to 0.5.

4.4 Numerical Results Using the Equivalent Coalescence Model

Using the equivalent coalescence model, the stress-strain response has been predicted for a set of input flaw density and strain rate. The results are compared with the original coalescence model to check the accuracy and computational efficiency. Results are also generated for a lower flaw density and strain rate than those used for the original coalescence model and compared to the stress-strain response without coalescence.

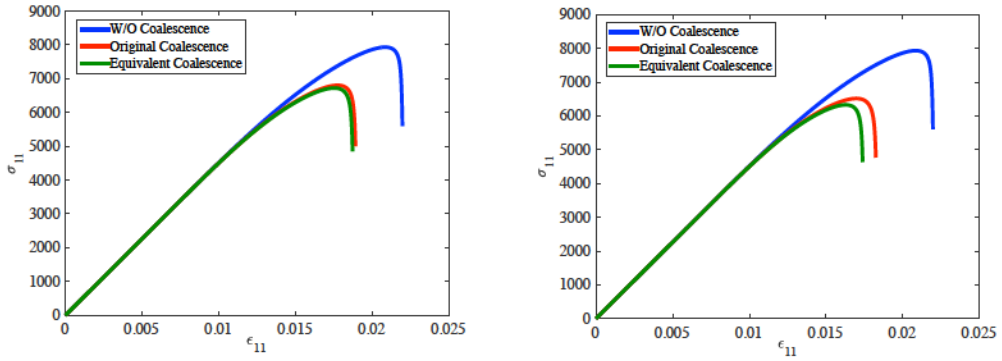

Figure 4.3: Comparison of stress-strain response from the original coalescence model, the equivalent coalescence model and the PR model (without coalescence). The plot on the left shows the response considering only pattern-1 coalescence both in original and equivalent coalescence model. The plot on the right shows the response when both pattern-1 and pattern-2 coalescence is considered. The flaw density used to generate this plot is $10^9\, m^{-2}$ and the strain rate is $10^5\, s^{-1}$.

Figure 4.3 compares the response using the original coalescence model, the equivalent coalescence model, and the PR model. The response using the equivalent coalescence model is close to the original coalescence model, both predicting a significant

reduction in peak stress. The response using the equivalent coalescence model based on only pattern-1 coalescence matches the response predicted by the original coalescence model very well, with an error in peak stress of 1.1%. The small amount of error can be explained as follows. Since initially the crack growth increment is relatively low for the single crack family, the pattern-1 coalesced crack families created at each load step have similar crack growth rate. Therefore, the equivalent crack replacing these crack families produces similar damage. The crack growth rate for the pattern-1 coalesced crack family increases at higher strain rates; however the higher equivalent wing crack length ${l_1}^{*\text{eff}}$ in equation (4.5) compensates somewhat for this wing crack growth.

A higher error of 2.89% in the peak stress is reported when both pattern-1 and pattern-2 coalescence are considered in the original and effective coalescence model (see the right column of figure 4.3). The reduction in peak stress increases after the addition of pattern-2 equivalent crack family. The pattern-2 crack families introduce larger cracks into the domain. Since the pattern-2 coalesced crack families arise from pattern-1 coalesced crack families, additional error is introduced due to the representation of the pattern-1 crack family by a single equivalent crack. In addition, the higher equivalent wing crack length ${l_2}^{*\text{eff}}$ increases the softening in the material.

The comparison of the results can be clarified by considering the relative contribution of damage arising from different original and equivalent crack families. Referring to the figure 4.4, the first row show the relative damage contribution by the original

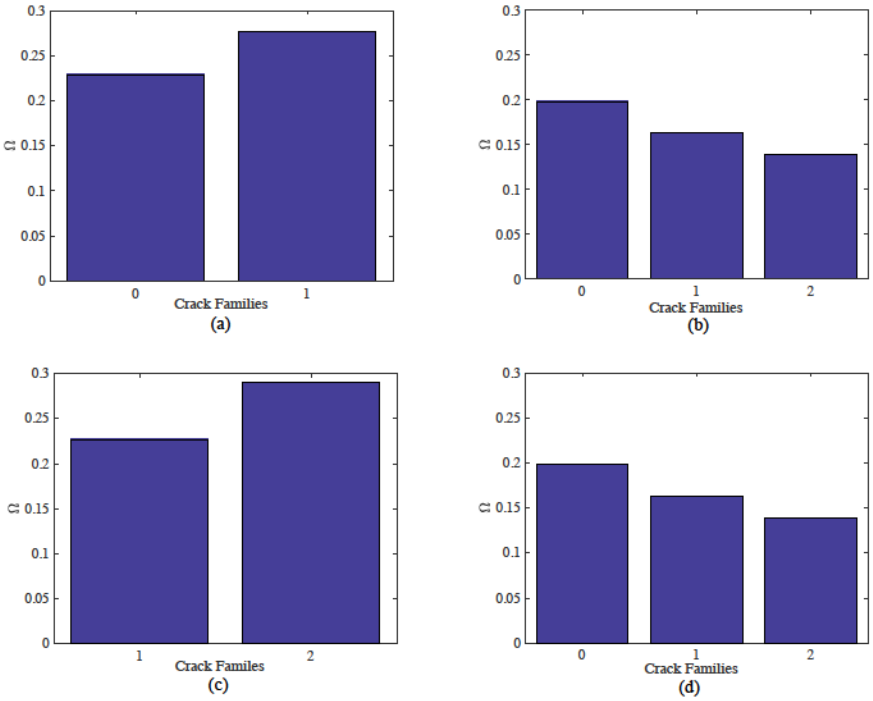

Figure 4.4: (a) Bar plot showing damage contribution by single and original pattern-1 family. (b) bar plot showing damage contribution by single, original pattern-1 and original pattern-2 crack family. (c) bar plot showing damage contribution by single and equivalent pattern-1 family. (d) bar plot showing damage contribution by single, equivalent pattern-1 and equivalent pattern-2 crack family. The flaw density used to generate this plot is $10^9\, m^{-2}$ and the strain rate is $10^5\, s^{-1}$.

crack families, and the second row shows the relative damage contribution by equivalent crack families. The second plot in upper and lower rows include both pattern-1 and pattern-2 coalesced crack families. The family-0 is the single crack family for all the plots. The original coalescence model predicts that family-0 contributes the most damage and that pattern-1 contributes significantly to damage when pattern-1 and pattern-2 crack families are included. Using the equivalent crack model, the damage contribution from pattern-2 coalesced crack family is slightly higher due to the higher equivalent wing crack growth.

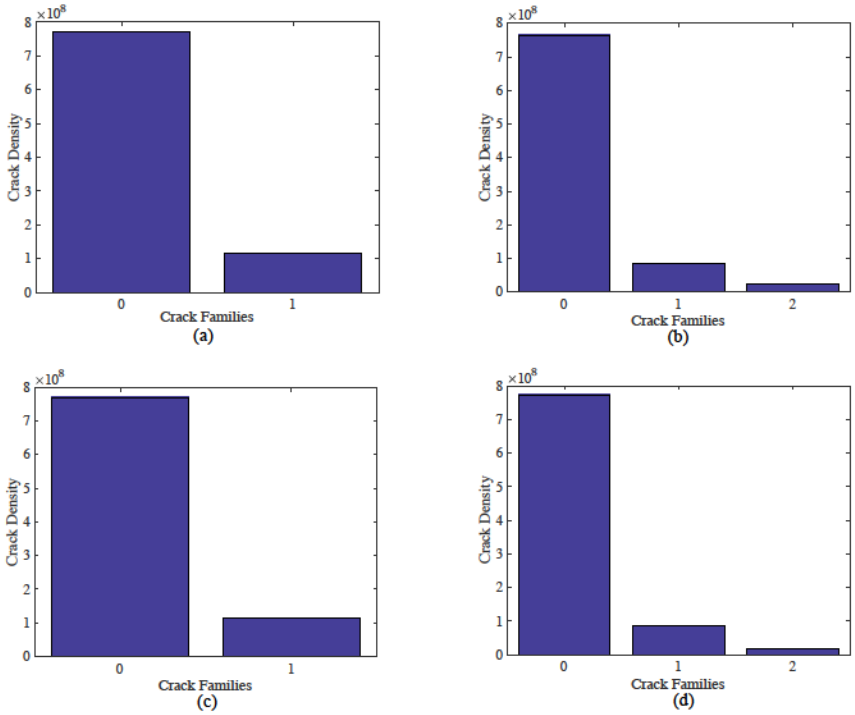

Figure 4.5: a) Bar plot showing crack density of single and original pattern-1 family. (b) bar plot showing crack density of single, original pattern-1 and original pattern-2 crack family. (c) bar plot showing crack density of single and equivalent pattern-1 family. (d) bar plot showing crack density of single, equivalent pattern-1 and equivalent pattern-2 crack family. The flaw density used to generate this plot is $10^9\, m^{-2}$ and the strain rate is $10^5\, s^{-1}$.

Figure 4.5 shows bar plots of crack densities associated with different crack patterns. The density of the single crack (non-coalesced) is the highest, followed by the pattern-1 coalesced cracks. The total density of pattern-2 coalesced cracks in the original and equivalent coalescence model is small, but sufficient to produce significant damage in the material.

With low flaw densities, the original coalescence model becomes very slow, but using the equivalent coalescence model these analyses become feasible. Figure 4.6 shows the stress-strain response using the equivalent coalescence model for a flaw

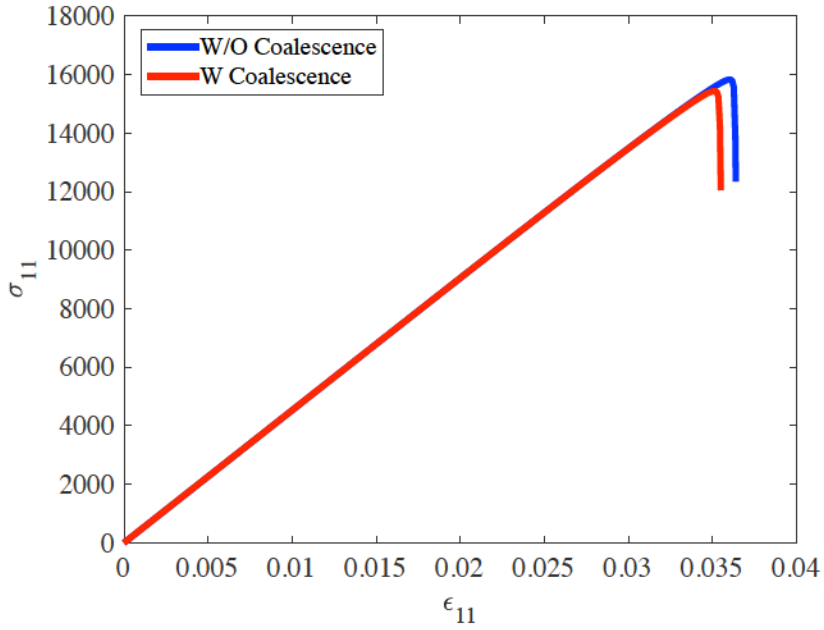

Figure 4.6: Stress-strain response at a low flaw density of $10^7 m^{-2}$ and the associated strain rate is $5 * 10^3 s^{-1}$. The blue line is the response without coalescence (using the PR model) and the red line is the response with equivalent coalescence.

density of $10^7 m^{-2}$ and strain rate of $5 * 10^3 s^{-1}$. As expected, the effect of coalescence at this lower flaw density is small given the larger crack spacings. The equivalent coalescence model enables a coalescence based model for materials with much lower flaw density, which is not nearly as efficient using the original coalescence model.

The computation time required for the original micromechanics model including all the crack families belonging to pattern-1 and pattern-2 coalescence is approximately 97 *sec* while the equivalent coalescence model with pattern-1 and pattern-2 coalesced crack families only require approximately 2.5 *sec*. The equivalent coalescence approach is almost 40 times faster than the original coalescence approach with 2.89% error level in response. The computation time for the original coalescence

model only considering the pattern-1 coalescence is 1 *sec* while the computational time for the equivalent coalescence model is 0.52 *sec*. In this case, the equivalent coalescence model is 2 times faster than the original coalescence model with 1.1% error.

4.5 Integration of Crack Coalescence Model into Tonge-Ramesh Model

A brief description of mechanism-based TR model is provided in chapter 1. Input for the TR model includes the flaw size distribution and the average flaw density. The 3D scalar damage parameter is estimated as the local flaw density multiplied by the crack length cubed.

$$\Omega = \sum_{k=1}^{N_{\text{bins}}} \omega_k l_k^3 \tag{4.9}$$

where ω_k is the crack density for each bin (with a total number of N_{bins}) and l_k is the wing crack length associated with each bin. The selection methodology of random flaw sizes and the local flaw density associated with each bin is explained in details in chapter 2. The TR model incorporates a flaw population sampled from the local flaw size distribution as an initial local description of the random microstructure associated with a discretized material domain of interest or a material point. The TR model does not capture the effect of explicit crack coalescence which has been shown in chapter 3 and chapter 4 to be significant for dynamic strength in the case of a 2D micromechanics model. The effect of coalescence addressed in chapter 3 is relevant for a single material point in the context of a 2D micromechanics model with microcracking as the sole physical mechanism. The TR model incorporates multiple macro-scale mechanisms including micro-scale cracking. The model transitions from

micro-scale cracking to macro-scale granular plasticity at a highly damaged state of the material. The effect of crack coalescence is yet unknown for a scenario where various macro and micro-scale mechanisms are activated under impact loading. This section describes implementation of explicit crack coalescence TR model to predict the effect on dynamic strength.

Because the TR model uses a distribution of initial flaw sizes, the coalescence model is extended to address multiple flaw sizes. For simplicity, only pattern-1 coalescence is implemented for each of these multiple flaw sizes. Furthermore, the coalescence process is considered independently for each individual crack family represented by a distinct flaw size. The coalescence between crack families with different flaw sizes are not considered, both for simplicity and also to reduce computational burden when solving the actual boundary value problem of interest. The approach could be extended to consider cross-coalescence of multiple crack families, but for now we focus on capturing the basic effects of coalescence. A schematic diagram is given in figure 4.7 showing an outline of the coalescence process implemented in TR model.

For each flaw family, the damage associated with the equivalent crack family is:

$$\Omega_{\text{eff}} = \omega^{\text{eff}}(\frac{l^{\text{eff}}}{2} + l_1^{\text{eff}})^3 \tag{4.10}$$

where ω^{eff} is the density of the equivalent crack family and estimated as $\omega_{\text{eff}} =$

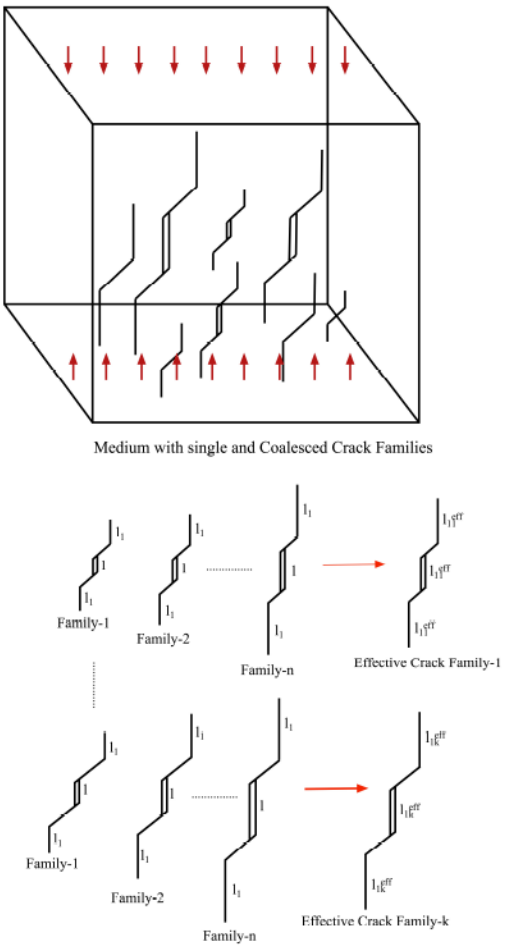

Figure 4.7: An illustration of crack coalescence implemented into TR model. The figure in the first row shows a block of materials containing coalesced and non-coalesced crack families undergoing uniaxial dynamic compression. The second row shows the equivalent crack approach for a crack family with a particular flaw size. The third row represents that an equivalent crack family is created for each bin.

$\sum_k \omega_k^{\text{coales}}$, l^{eff} is the distance between the pair of splitting forces and l_1^{eff} is the wing crack length. The distance l^{eff} for a 3D model is estimated using the same analogy of equal damage as in the 2D case described earlier in the chapter:

$$l^{\text{eff}} = \left(\frac{\sum_k \omega_k l_k^3}{\omega^{\text{eff}}} \right)^{\frac{1}{3}} \tag{4.11}$$

The wing crack length using the 3D damage formulation for the equivalent crack family is estimated as:

$$l_1^{\text{eff}(n)} = \left[\frac{\omega^{\text{eff}(n-1)}}{\omega^{\text{eff}(n)}} \left(\frac{l^{\text{eff}(n-1)}}{2} + l_1^{*(n)\text{eff}} \right)^3 + \frac{\omega_k^{(n)}}{\omega^{\text{eff}(n)}} \left(\frac{3l}{2} \right)^3 \right]^{\frac{1}{3}} - \frac{l^{\text{eff}(n)}}{2} \tag{4.12}$$

where $\omega^{\text{eff}(n-1)}$ is the density of the equivalent crack family at a load step $(n-1)$, $\omega^{\text{eff}(n)}$ is the density of the same crack family at a load step (n), $l^{\text{eff}(n-1)}$ is the distance between the splitting forces of the equivalent crack at a load step $(n-1)$, $l_1^{*(n)\text{eff}}$ is the wing length for equivalent crack family at load step (n), $\omega_k^{(n)}$ is the density of the pattern-1 coalesced crack family at load step (n) , l is the wing crack length of original pattern-1 coalesced crack family at the load step (n) and $l^{\text{eff}(n)}$ is the distance between the pair of splitting forces for the equivalent crack family at load step (n).

The crack density for the single and equivalent coalesced crack for each family is updated using a similar probability of coalescence to that shown in chapter 3 for a 2D crack. The formulation is extended to the 3D case by estimating the probability of intersecting another crack in the volume shown in figure 4.8. The probability of

coalescence is estimated using two similar approaches. Assuming that coalescence occurs in the increment of wing crack growth on one side of the crack, the probability of coalescence is estimated as:

$$P_{\text{coales}} = 1 - e[-\omega^{\text{eff}} \dot{l} dt \cos\phi 2\pi s^2] \tag{4.13a}$$

$$\omega^{\text{eff}} = \omega^{\text{eff}} + 0.5 P_{\text{coales}} \omega^{\text{eff}} \tag{4.13b}$$

$$\omega^{\text{eff}} = (1 - P_{\text{coales}}) \omega^{\text{eff}} \tag{4.13c}$$

where ω^{eff} is the density of the effective coalesced crack family. When coalescence is assumed to occur in the increment of the wing-crack growth on both sides of the crack, the probability of coalescence is estimated as:

$$P_{\text{coales}} = 1 - e[-\omega^{\text{eff}} \dot{l} dt \cos\phi \pi s^2] \tag{4.14a}$$

$$\omega^{\text{eff}} = \omega^{\text{eff}} + P_{\text{coales}} \omega^{\text{eff}} \tag{4.14b}$$

$$\omega^{\text{eff}} = \omega^{\text{eff}} - 2 P_{\text{coales}} \omega^{\text{eff}} \tag{4.14c}$$

The basic idea using both these approaches is very similar, but the results are slightly more stable since the total probability of coalescence is 1. This approach is used in the TR model implementation.

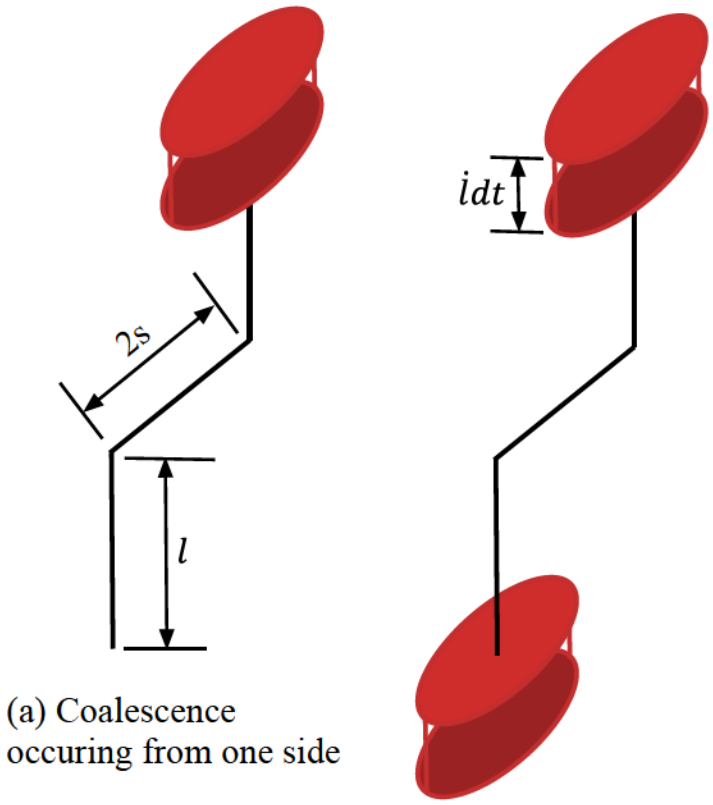

Figure 4.8: (a) The figure shows the volume (marked in red) used for estimating the probability of coalescence. (b) The figure shows the regions (marked in red) on both sides of wing crack used in estimating the probability of coalescence.

4.6 Numerical Result for Single Element

Numerical simulations are performed at a single material point in order to predict the effect of crack coalescence in the TR model. The coalescence mechanism leads to a significant reduction in peak stress under uniaxial compression in the simple micromechanics model (chapter 3). This effect of coalescence is verified under multiple strain rates for uniaxial compression using the TR constitutive model. Material properties used in the simulations are given in table 4.1.

Density (kg/m^3)	2520
Bulk Sound Speed (ms^{-1})	9600
Linear Term in Shock Speed Relation	914
Grüneisen Constant	1.28
Bulk Modulus (GPa)	233
Shear Modulus (GPa)	197
Minimum Flaw Size ($\mu\, m$)	1
Maximum Flaw Size ($\mu\, m$)	25
Flaw Distribution Exponent	2.6
Flaw Density (m^{-3})	$2.2 * 10^{13}$
Relaxation Time (sec)	$5 * 10^{-9}$
Damage to Initiate Granular Flow	0.125
Maximum Damage	0.126

Table 4.1: Material properties used in simulations using TR constitutive model. The model material is boron carbide. The material properties are obtained from [1].

The stress-strain response shows a significant decrease in peak stress when crack coalescence is considered (see figure 4.9). Multiple crack families are activated under the strain rate of $500\, s^{-1}$ to generate wing cracks. A fraction of the cracks belonging to each family merge to produce pattern-1 coalesced cracks. The respective flaw densities and crack growth rates for the coalesced crack families are sufficient to

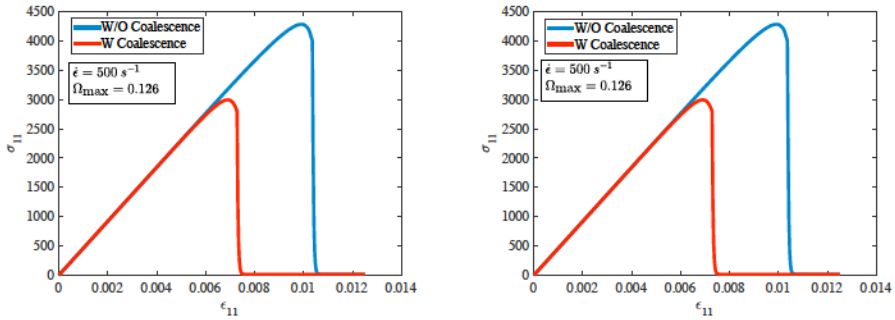

Figure 4.9: Stress-strain response under a strain rate of $500\,s^{-1}$ is shown. The left figure shows the response using the first approach for probability of coalescence. The right figure shows the response using the second approach for probability of coalescence. The maximum damage level that the material can sustain is set as 0.126. 10 bins are used for this simulation. There is no significant difference in stress-strain response for two approaches of probability of coalescence.

have a significant effect on damage, which results in a lower the peak stress. The onset of granular plasticity occurs at a lower strain, due to the fact that predefined damage threshold is reached much faster when considering coalesced crack families (see figure 4.10).

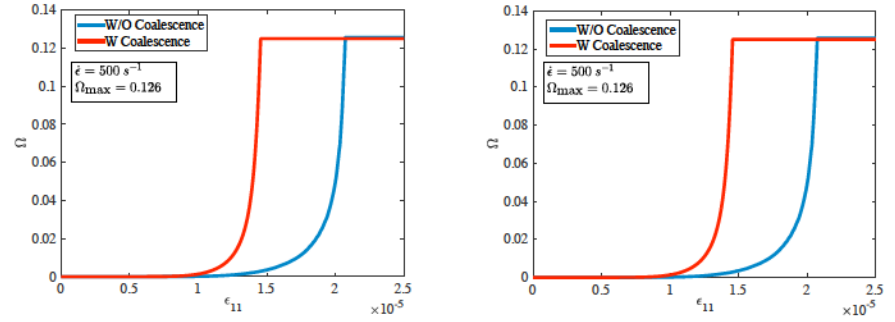

Figure 4.10: The damage vs. strain under a strain rate of $500\,s^{-1}$ is shown. The left and right figure corresponds to the two cases of coalescence respectively. The damage evolution under this strain rate is also similar for two cases of coalescence.

Figure 4.11 highlights the evolution of coalesced cracks from the single cracks at the last load step. Wing cracks are introduced only from a few families that have larger

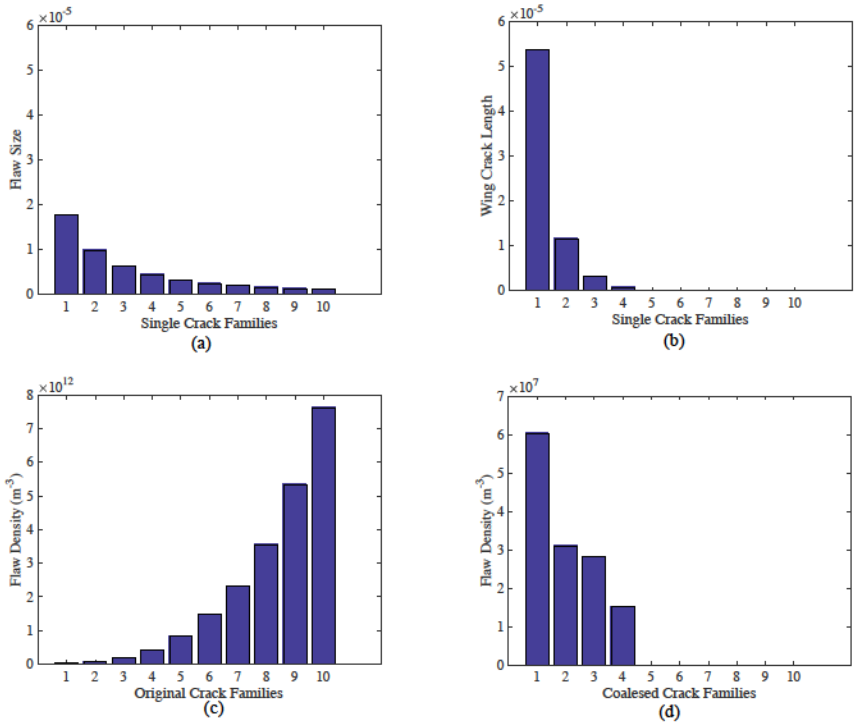

Figure 4.11: (a) Bar plot showing flaw sizes for the single crack families. Largest flaw has the lowest density and smallest flaw has the highest density. (b) bar plot showing wing crack lengths (calculated at last load step) associated with the single crack families. The wing cracks are growing from four single crack families. (c) bar plot showing crack (same as flaw density) density associated with single crack families at the last load step. (d) bar plot showing crack density of coalesced crack families. There are four coalesced crack families associated with four single crack families that are activated to produce wing cracks. The strain rate is 500 s^{-1}.

flaw sizes (see figure 4.11 (a) and figure 4.11 (b)). Therefore, coalescence occurs only in those families (see figure 4.11(d)). The crack densities (see figure 4.11(d)) (same as flaw density) associated with coalesced cracks at the last load step is relatively low compared to the crack densities (see figure 4.11(c)) associated with single cracks. The damage contribution by coalesced cracks is still significant due to much higher crack growth rate.

Results for strain rates of $10^3\ s^{-1}$ and $10^4\ s^{-1}$ are also analyzed to predict the rate effect for a given distribution of input flaw sizes and an average flaw density (see figure 4.12). The peak stress under $10^3\,s^{-1}$ for both non-coalesced and coalesced cases have increased slightly to the peak stress at a strain rate of $500\,s^{-1}$, which is expected with increase in strain rate. The reduction in peak stress due to coalescence is significant under $10^3 s^{-1}$. The increase in peak stress for non-coalesced and coalesced cases have increased significantly under a strain rate of $10^4\ s^{-1}$. The effect of coalescence is much smaller under this strain rate due to the inertial effect associated with dynamic crack propagation.

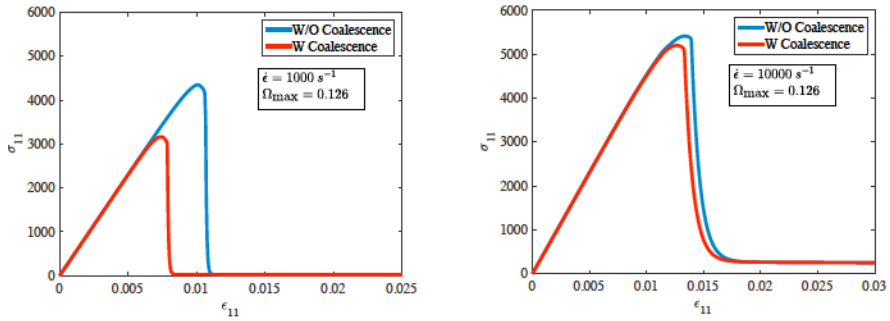

Figure 4.12: The left plot shows the stress-strain response under a strain rate of $10^3\ s^{-1}$ and the right plot shows the stress-strain response under a strain rate of $10^4\ s^{-1}$. The blue lines in both plots show the response without coalescence and the red lines in both plots show the response considering coalescence

Figure 4.13 shows the comparison of damage evolution considering coalescence under the strain rates of $10^3 s^{-1}$ and $10^4 s^{-1}$. The softening and transitioning to granular flow occurs at a lower strain level under $10^3 s^{-1}$, since the coalescence accelerates damage through higher crack growth rate associated with coalesced crack families. At a higher strain rate of $10^4 s^{-1}$, the damage growth associated with coalescence is

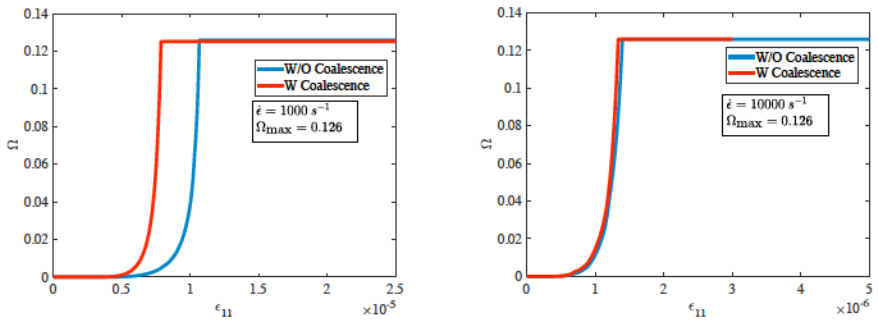

Figure 4.13: The left column shows the damage vs. strain plot under a strain rate of $10^3 s^{-1}$ and the right column shows the damage vs. strain plot under a strain rate of $10^4 s^{-1}$. The blue lines indicate response without coalescence and the red lines indicate response considering coalescence.

much smaller.

The effect of higher strain rate on coalescence can be clearly visualized from a crack density plot for both the strain rates. Figure 4.14 shows the crack densities (lower row) associated with single and coalesced crack families at a strain rate of $10^3\ s^{-1}$. The wing cracks are growing from five flaw families $(1-5)$ (see figure 4.14(b)). The fraction of crack associated with each coalesced crack family (see figure 4.14(d)) has increased from the case shown in figure 4.11(d). The density of the newly added coalesced crack family (5 in figure 4.14(d) associated with single crack family 5 in figure 4.14(c)) is much lower. However, the peak stress shown in the left plot of figure 4.12 is not significantly different from the peak stress predicted under $500\ s^{-1}$. More flaws are activated to produce wing cracks at the higher strain rate, so they introduce more coalesced crack families. However, if the crack growth rate associated with coalesced crack families are not significant their relative contribution to global damage is relatively less in further reduction in peak stress.

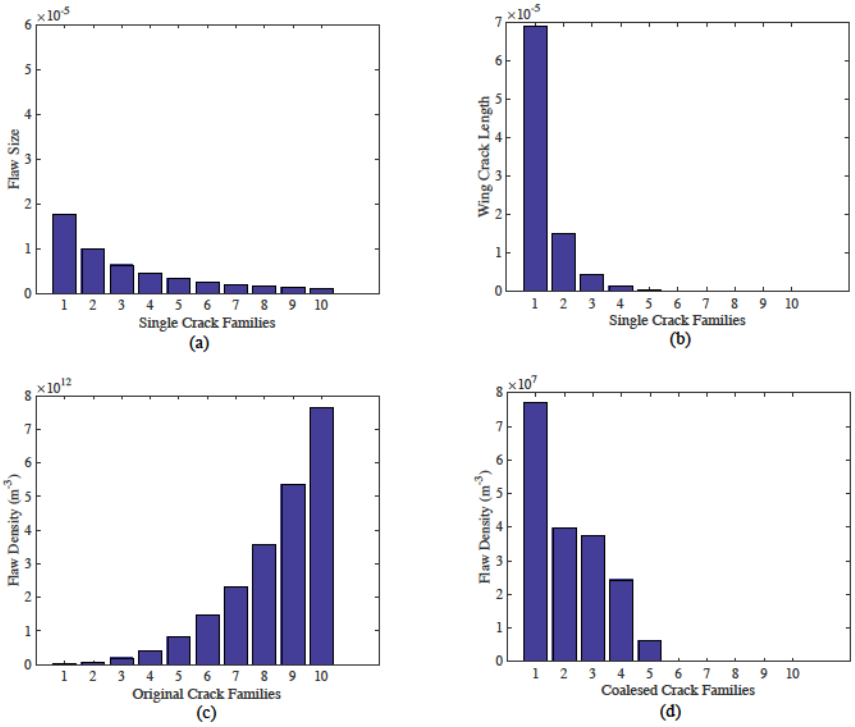

Figure 4.14: (a) Bar plot showing flaw sizes for the single crack families. Largest flaw has the lowest density and smallest flaw has the highest density. (b) bar plot showing wing crack lengths (calculated at last load step) associated with the single crack families. (c) bar plot showing crack (same as flaw density) densities associated with single crack families at the last load step. (d) bar plot showing crack densities of coalesced crack families. The strain rate is $10^3\ s^{-1}$.

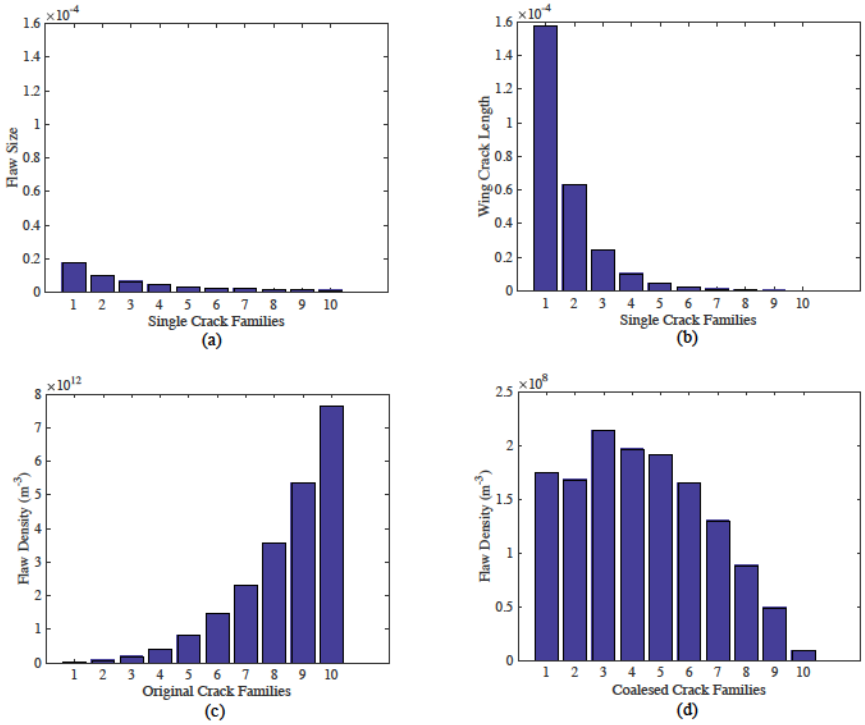

Figure 4.15: (a) Bar plot showing flaw sizes for the single crack families. Largest flaw has the lowest density and smallest flaw has the highest density. (b) bar plot showing wing crack lengths (calculated at last load step) associated with the single crack families. (c) bar plot showing crack (same as flaw density) density associated with single crack families at the last load step. (d) bar plot showing crack density of coalesced crack families. The strain rate is $10^4\ s^{-1}$.

Figure 4.15 shows the crack densities (lower row) associated with single and coalesced crack families at a strain rate of $10^4\ s^{-1}$. At this strain rate, all the single crack families are activated (see figure 4.15(b)). The coalesced crack families are also growing from all the single crack families (see figure 4.15(d)). At this high strain rate, single crack families with smaller flaw sizes can exhibit significant wing crack growth, therefore increasing the probability of coalescence for pattern-1 coalesced crack families. Therefore, at high strain rates coalescence occurs in a broader range of underlying flaw families. The crack growth speed is rate-limited, so these coalesced

cracks have little effect on the stress-strain response.

4.7 Summary

An alternative approach has been developed to address the computational efficiency associated with original coalescence model discussed in chapter 3. The original coalescence model aims at capturing the crack merging process during post peak softening by incorporating a number of different pattern of coalesced crack families. Tracking the growth and associated damage of those crack families is computationally very expensive. In the alternative approach, all the crack families within a pattern is replaced by an equivalent crack. The properties of the equivalent cracks are updated based on the properties of original coalesced cracks at each load step. The numerical results compare very well using original and equivalent coalescence approach. Due to computational speed up the equivalent coalescence model is very suitable for large-scale simulations with a computationally demanding mechanism-based constitutive model. To verify the effect of coalescence the equivalent model is implemented in mechanism-based TR constitutive model. The results obtained from the equivalent coalescence model can be summarized as:

- The equivalent coalescence model predicts a reduced peak stress similar to the original coalescence model compared to the solution without coalescence.
- Stress-strain response predicted by the equivalent coalescence model using only

pattern-1 coalescence tracks the response of the original coalescence model with an error of 1.1% .

- Stress-strain response predicted by the equivalent coalescence model including both pattern-1 and pattern-2 coalescence tracks the response predicted by the original coalescence model with an error level of 2.89%. The equivalent coalescence model slightly over predicts the damage.

- The computational speed up is approximately 40 times higher using the equivalent coalescence model using pattern-1 and pattern-2 coalescence.

- Stress-strain response with equivalent coalescence in TR constitutive model also predicts a significant reduction in peak stress under lower strain rates.

The equivalent coalescence approach predicts similar results as the original coalescence model with a relatively low error and high computational efficiency. The same trend is observed when implemented in the mechanism-based TR constitutive model. This approach is very useful for a computational solution of boundary value problem using a multi-scale model capturing different length and time scale mechanisms.

Chapter 5

Summary and Future Work

5.1 Summary

In this work we have developed two models to address dynamic brittle failure of armor ceramic. The constitutive response of these materials is highly influenced by the statistical distribution of preexisting microstructural defects. To predict the failure behavior under dynamic loading, the natural choice is to incorporate the initial flaw statistics into the constitutive model. In a multi-scale framework, the distinct statistical sampling of the defect population at each material point or integration point represent the realistic point-to-point variability in the micromorphology. Optimal selection of the realization of input flaw statistics is necessary to ensure maximum computational efficiency at given level of accuracy. The current work proposed a model that reduces the computational effort further by incorporating a damaged-based cri-

terion into the flaw population sampling approach. The mathematical framework for the numerical technique is discussed in detail in chapter 2. The advantage of this numerical technique is summarized as:

- The technique provides a formal framework for sampling by using the probability space ($0-1$ space). Each direction of the probability space is assigned to a random variable such as flaw size or orientation. The finite space is divided into either uniform or non-uniform intervals. The grid morphology of the space is altered to sample a range of variables of interest.

- The method is not limited to applications of dynamic brittle failure. It aims to reduce generic function evaluations by optimally selecting representative input random variables of the function.

- The method is applied to two constitutive models related to dynamic brittle failure. First, it is applied in the context of a simple 2D micromechanics model to verify the accuracy. A skewed grid morphology is used to capture the larger flaw sizes, since they play a major role in dynamic brittle failure. The skewed grid morphology is obtained by developing a zooming function based on the distribution of the variable. The response using the optimal sample has less than 0.1% error with two orders of magnitude speed up in computational efficiency.

- The method is also applied to a computationally demanding mechanism-based constitutive model (TR model). As with the 2D micromechanics model, the

stress-strain response under uniaxial compression shows increased efficiency and same level of accuracy

The second model proposed in the current work is developed to capture crack coalescence under dynamic uniaxial compression. A combined probabilistic micromechanics-based approach is proposed for capturing the crack coalescence in brittle materials. The details description of the model is provided in chapter 3. The crack coalescence model predicts:

- There is a significant reduction in peak strength considering crack coalescence.
- The effect of coalescence is more significant at lower strain rates and higher flaw densities

An alternative approach for crack coalescence is proposed in chapter 4 to address efficiency issues associated with tracking a large number of crack families in the crack coalescence model. In this approach, multiple crack families within a pattern of coalescence are replaced by a single equivalent crack. This efficient approach is implemented in the mechanism-based TR model. The details of this approach and implementation in TR model is discussed in chapter 4. The results from this model shows:

- As with the original crack coalescence model, the efficient crack coalescence approach predicts a significant reduction in dynamic compressive strength.

- The error associated with the efficient approach relative to the original coalescence model is 2.89% with 40 times increased computational speed.
- There is a significant reduction in peak stress predicted by the TR model when using the equivalent coalescence model.

In summary, this dissertation work develops two models addressing two important aspect of dynamic brittle failure of armor ceramics. The optimal input flaw statistics aids in computational efficiency. The crack coalescence model predicts a significant reduction in peak stress which is closer to experimental observation [7]. The equivalent coalescence also predicts significant reduction in peak stress with much greater efficiency when implemented into the TR model.

5.2 Future Work

Dynamic brittle fracture in general remains a very rich topic for future research. There are many interesting problems that have been attempted to solve yet many are still in progress. We have addressed some issues of dynamic brittle fracture in order to provide simple solutions to rather complicated problems. However, the capability of the existing multi-mechanism models can be enhanced. The other mechanisms represented in the model need continuous improvement. Furthermore, the transition from one mechanism to another is often not well understood. In this section, we provide some thoughts on the future directions for enhancing the capability of the

existing models and also on possible new model development.

5.2.1 Improvement in Binning Scheme

The binning scheme developed in chapter 2 assumes that the cracks remains in a fixed set of bins. This approach is limited to sample only the initial random input for any function evaluations. However, this approach is not suitable for capturing an evolving sample population like a growing crack population or problems like crack coalescence. There several improvement that can be implemented into the existing binning framework.

- In the existing framework, the fraction or the weight remains constant throughout the simulation The binning framework can be extended to capture the evolving sample population by updating the fraction of population associated with each Gauss point or bin. The weight associated with each Gauss point can be altered based on the change in the attribute of the variable that is binned. One good example is rebinning the crack population when there is coalescence of cracks. This can be achieved by lumping newly coalesced cracks into the nearest available bins. The crack length associated with the bin can be updated, as can the weights associated with that bin.

- The formulation assumes that random input parameters (e.g., crack length and orientation) are uncorrelated. The formulation can be easily extended to in-

corporate correlated random variables. The new formulation with correlated random variables can be utilized for many classes of problems.

- The zooming functions to alter the grid morphologies are developed only for a few specific distributions. A complete set of zooming functions using different input distributions can be built to capture different random variables relevant to dynamic brittle failure problems.

5.2.2 Enhancing the Crack Coalescence Model

Some simplifying assumptions have been made for crack coalescence model. There are possible future directions that could improve the crack coalescence model.

- The crack coalescence model only considers coalescence between cracks with same flaw size. Multiple flaw size crack families will introduce cross coalescence. Conceptually, this is straightforward to introduce into the model; however, the problem could be computationally intensive. A coalesced crack from different crack families will introduce yet another pattern into the problem. However, with careful consideration of equivalent cracks, this cross-coalescence could be introduced to make the model more realistic.

- The crack coalescence model uses the simple damage compliance relationship proposed by [27], which does not necessarily include a realistic change in compliance due to single wing cracks or coalesced cracks. An improved change in

compliance due to single wing cracks is proposed [4]. However, the approach proposed by [4] involves numerical fitting. Analytical expressions for compliance for coalesced cracks can be obtained by developing crack compliance tensor [88].

- The coalescence model does not explicitly account for the bulking or dilatancy associated with coalesced cracks, which affects the constitutive response significantly. Simple approaches described by [24] can be adopted to estimate the overall dilatancy when coalescence is considered.

- The effect of coalescence is verified only for simple uniaxial compression. The effect of coalescence should be verified for a more complex loading scenario.

- The coalescence model is also implemented in the TR constitutive model to represent the initiation of comminution. In the context of TR model, adding coalescence ensures early onset of granular flow due to increased damage. The transition from microcracking to macroscale granular plasticity is based on a damage threshold, but not on a well defined mechanics-based criterion in the TR model. The TR model would benefit from a more rigorous understanding of this transition.

5.2.3 Implementation of Crack Coalescence into a Multi-Scale Model

The crack coalescence model is only implemented into the different constitutive models at a single integration point. The implementation in the simple micromechanics model and mechanism-based TR constitutive model predicts significant reduction is peak stress. However, the effect of coalescence is not verified for a realistic multi-scale model, which can simulate a real impact event. Further validation of the crack coalescence model can be done by implementing the model into a larger scale model, for example using the Material Point method implemented in Uintah [89]. The results can then be compared with experimental results. Some of the relative experiments for validation are:

- A Kolsky bar test evaluates dynamic uniaxial compression by applying a uniform increasing traction at the ends of the sample. A uniform stress state is observed with homogeneous deformation, but the deformation no longer remains homogeneous once the damage initiates. The boundary traction and displacement no longer represent the local stress state in the material. However, heterogeneous damage pattern can be observed in those experiments. Applying the coalescence model into a model of a Kolsky bar test would provide an idea of how well the model performs under a local multi-axial stress state.

- A relevant experiment representing impact can be spherical impact on cylnders.

Some of the robust features expected in this kind of experiment include formation of radial or cone cracks. A comparison between the model and the experiment can be done in terms of damage zone formation [90].

Appendix A

Appendix from Chapter 2

In order to highlight the significance of random fluctuations in the summation described in equation (2.1), we derive the coefficient of variation of this quantity, assuming that both the function $h(g(\hat{r}_p, t))$ and the number of points $p_{\max}$ are independent random variables. The values $h(g(\hat{r}_p, t))$ are also assumed to be independent identically distributed random variables. Using the law of total expectations [91], the expected value of the summation in equation (2.1) is derived using

$$E[\overline{h}(t)] = E[E[\overline{h}(t)|p_{\max}]] = E\left[\frac{1}{p_{\max}}\sum_{p=1}^{p_{\max}} E[h[\hat{x}_p(t)]\right] = E[h[\hat{x}_p(t)]]. \tag{A.1}$$

Not surprisingly, the mean of the average value of $h[\hat{x}_p(t)]$ represented by $\overline{h}(t)$ is simply equal to the mean value of $h[\hat{x}_p(t)]$. Similarly the variance of this summation

is found by using the Theorem of Total Variance [91]:

$$\begin{aligned} \mathrm{Var}[\overline{h}(t)] &= \mathrm{Var}[E[h(t)|p_{\max}]] + E[\mathrm{Var}[h(t)|p_{\max}]] \\ &= \mathrm{Var}[E[h[\hat{x}_p(t)]] + E\left[\frac{1}{{p_{\max}}^2}\sum_{p=1}^{p_{\max}}\mathrm{Var}[h[\hat{x}_p(t)]\right]. \end{aligned} \tag{A.2}$$

The second term on the right-hand side uses the fact that the variance of a sum of random variables is equal to the sum of the variances of the random variables. Because the expected value $E[h[\hat{x}_p(t)]$ is a fixed value, the variance of the expected value is zero and the first term on the right-hand side can be neglected. Therefore, the above expression simplifies to

$$\mathrm{Var}[\overline{h}(t)] = E\left[\frac{1}{p_{\max}}\mathrm{Var}[h(\hat{x}_p(t))]\right] = E\left[\frac{1}{p_{\max}}\right]\mathrm{Var}[h(\hat{x}_p(t))]\,. \tag{A.3}$$

Combining equation (A.1) and equation (A.3) the coefficient of variation of equation (2.1) is:

$$\mathrm{C.O.V.}[\overline{h}(t)] = \mathrm{C.O.V.}[h(\hat{x}_p(t))]\sqrt{E\left[\frac{1}{p_{\max}}\right]}. \tag{A.4}$$

If we assume that crack occurrences are statistically independent (in other words there is no clustering or anti-clustering of the cracks in space), then the total number of cracks $p_{\max}$ in a given finite element follows a Poisson distribution with parameter $\lambda = \eta A_e$, where η is the average number of cracks per unit area, and A_e is the area

of finite element e. The expected value of one over this Poisson random variable is given as

$$E\left[\frac{1}{p_{\max}}\right] = \sum_{k=1}^{\infty} \frac{1}{k} \frac{\lambda^k e^{-\lambda}}{k!} \,. \tag{A.5}$$

As λ increases, the quantity in equation (A.5) decreases. For numerical applications that incorporate the random variability in equation (2.1), it is worthwhile to identify the value of λ for which this variability is negligible and the medium can be treated as spatially homogeneous. This question is answered by setting the coefficient of variation in equation (A.4) to the order of double precision accuracy, or 10^{-16}, and solving for λ. Recognizing that the value of λ corresponding to this very small expected value must be very large ($\lambda > 1000$), the discrete Poisson probability mass function in equation (A.5) can be approximated as a continuous Gaussian probability density function with mean $\mu = \lambda$ and variance $\sigma^2 = \lambda$ [92]:

$$E\left[\frac{1}{p_{\max}}\right] = \int_{-\infty}^{\infty} \frac{1}{n\sqrt{2\pi\lambda}} e^{-\frac{(n-\lambda)^2}{2\lambda}} dn \rightarrow \int_{-\infty}^{\infty} \frac{1}{n} \delta[n-\lambda] dn = \frac{1}{\lambda} \,. \tag{A.6}$$

The last step recognizes that, as λ becomes very large, the Gaussian probability density function begins to approximate a Dirac delta function at λ.

As an example, let us consider the simple 2D damage measure in equation (2.3). In this case $h(\hat{x}_p(t))$ is an individual realization of the crack length to the second power, and $p_{\max}$ is the number of cracks associated with a particular finite element. If we assume that crack length is an exponentially distributed random variable, then

the coefficient of variation C.O.V.$[h(\hat{x}_p(t))]=\sqrt{5}$. Combining this result with equation (A.6), the expression in equation (A.4) is approximated as

$$\text{C.O.V.}[\overline{h}(t)] = \sqrt{\frac{5}{\lambda}}\,. \tag{A.7}$$

In order for the variability of the summation in equation (2.1) to be less than roundoff error (10^{-16}), this suggests that λ must be on the order of 5×10^{32}. A typical very high estimate of the area crack density η in brittle media is on the order of $10^{12}/\text{m}^2$. This would suggest that the finite element must be larger than 10^{20}m^2, or on the order of millions of kilometers squared. In other words, variability is not negligible for any realistic engineering damage model. Using a three-dimensional measure of damage, in which $h(\hat{x}_p(t))$ is an individual realization of the crack length to the third power, the coefficient of variation of the summation in equation (2.1) is equal to $\sqrt{29/\lambda}$. A typical flaw density of $5 \times 10^{12}/\text{m}^3$ [93] and a finite-element volume of 1 mm^3 corresponds to C.O.V. $\sim \sqrt{29/\lambda} = 7.6\%$. Perturbations of this magnitude significantly affect localized damage [56] .

Bibliography

[1] A. L. Tonge, "Enhancements to the tonge-ramesh ceramic failure model for use in eulerian simulations," US Army Research Laboratory, Tech. Rep., 2016.

[2] R. H. Wong and K. Chau, "Crack coalescence in a rock-like material containing two cracks," *International Journal of Rock Mechanics and Mining Sciences*, vol. 35, no. 2, pp. 147 – 164, 1998.

[3] B. Paliwal, K. Ramesh, and J. McCauley, "Direct observation of the dynamic compressive failure of a transparent polycrystalline ceramic (alon)," *Journal of the American Ceramic Society*, vol. 89, no. 7, pp. 2128–2133, 2006.

[4] J. Liu and L. Graham-Brady, "Effective anisotropic compliance relationships for wing-cracked brittle materials under compression," *International Journal of Solids and Structures*, vol. 100101, pp. 151 – 168, 2016.

[5] H. Deng and S. Nemat-Nasser, "Microcrack interaction and shear fault failure," *International Journal of Damage Mechanics*, vol. 3, no. 1, pp. 3–37, 1994.

BIBLIOGRAPHY

[6] K. Ramesh, J. D. Hogan, J. Kimberley, and A. Stickle, "A review of mechanisms and models for dynamic failure, strength, and fragmentation," *Planetary and Space Science*, vol. 107, pp. 10 – 23, 2015, {VIII} Workshop on Catastrophic Disruption in the Solar System.

[7] J. D. Hogan, L. Farbaniec, T. Sano, M. Shaeffer, and K. Ramesh, "The effects of microstructure on the uniaxial compressive strength and failure of boron carbide," *Journal of American Ceramics*, 2014.

[8] M. Bakas, J. W. McCauley, V. Greenhut, D. Niesz, R. Haber, and B. West, "Quantitative analysis of inclusion distributions in hot pressed silicon carbide," *International Journal of Impact Engineering*, vol. 50, pp. 40 – 48, 2012.

[9] N. P. Daphalapurkar, K. Ramesh, L. Graham-Brady, and J.-F. Molinari, "Predicting variability in the dynamic failure strength of brittle materials considering pre-existing flaws," *Journal of the Mechanics and Physics of Solids*, vol. 59, no. 2, pp. 297 – 319, 2011.

[10] W. F. Brace and E. G. Bombolakis, "A note on brittle crack growth in compression," *Journal of Geophysical Research J. Geophys. Res.*, vol. 68, pp. 2156–2202, 1963.

[11] E. Schulson, "The brittle compressive fracture of ice," *Acta Metallurgica et Materialia*, vol. 38, no. 10, pp. 1963–1976, 1990.

[12] E. Schulson, G. Kuehn, D. Jones, and D. Fifolt, "The growth of wing cracks and the brittle compressive failure of ice," *Acta metallurgica et materialia*, vol. 39, no. 11, pp. 2651–2655, 1991.

[13] G. Vekinis, M. Ashby, and P. Beaumont, "The compressive failure of alumina containing controlled distributions of flaws," *Acta Metallurgica et Materialia*, vol. 39, no. 11, pp. 2583 – 2588, 1991.

[14] S. Nemat-Nasser and H. Horii, "Compression-induced nonplanar crack extension with application to splitting, exfoliation, and rockburst," *Journal of Geophysical Research*, vol. 87, no. NB8, pp. 6805–6821, 1982.

[15] H. Horii and S. Nemat-Nasser, "Brittle failure in compression – splitting, faulting and brittle-ductile transition," *Philosophical Transactions of the Royal Society of London*, vol. 319, no. 1549, pp. pp. 337–374, 1986.

[16] M. F. Ashby and S. D. Hallam, "The failure of brittle solids containing small cracks under compressive stress states," *Acta Metallurgica*, vol. 34, no. 3, pp. 497 – 510, 1986.

[17] H. Horii and S. Nemat-Nasser, "Elastic fields of interacting inhomogeneities," *International Journal of Solids and Structures*, vol. 21, no. 7, pp. 731 – 745, 1985.

[18] M. Kachanov, "Elastic solids with many cracks: A simple method of analysis," *International Journal of Solids and Structures*, vol. 23, no. 1, pp. 23 – 43, 1987.

[19] M. Basista and D. Gross, "A note on crack interactions under compression," *International Journal of Fracture*, vol. 102, no. 3, pp. 67–72, 2000.

[20] D. F. Li, C. F. Li, S. Q. Shu, Z. X. Wang, and J. Lu, "A fast and accurate analysis of the interacting cracks in linear elastic solids," *International Journal of Fracture*, vol. 151, no. 2, p. 169, 2008.

[21] L. Ma, X. Wang, X.-Q. Feng, and S.-W. Yu, "Numerical analysis of interaction and coalescence of numerous microcracks," *Engineering Fracture Mechanics*, vol. 72, no. 12, pp. 1841 – 1865, 2005, international Conference of Heterogeous Material Mechanics, Chongqing University and Yangtze River/Three Gorges, China, June 21-26, 2004.

[22] H. Deng and S. Nemat-Nasser, "Dynamic damage evolution in brittle solids," *Mechanics of Materials*, vol. 14, no. 2, pp. 83 – 103, 1992.

[23] B. Paliwal and K. Ramesh, "An interacting micro-crack damage model for failure of brittle materials under compression," *Journal of the Mechanics and Physics of Solids*, vol. 56, no. 3, pp. 896 – 923, 2008.

[24] S. Nemat-Nasser and M. Obata, "A microcrack model of dilatancy in brittle materials," *Journal of Applied Mechanics*, vol. 55, no. 1, pp. 24–35, MAR 1988.

[25] G. Ravichandran and G. Subhash, "A micromechanical model for high strain rate behavior of ceramics," *International Journal of Solids and Structures*, vol. 32, no. 17, pp. 2627 – 2646, 1995.

[26] C. Huang, G. Subhash, and S. J. Vitton, "A dynamic damage growth model for uniaxial compressive response of rock aggregates," *Mechanics of Materials*, vol. 34, no. 5, pp. 267 – 277, 2002.

[27] B. Budiansky and R. J. O'connell, "Elastic moduli of a cracked solid," *International Journal of Solids and Structures*, vol. 12, no. 2, pp. 81 – 97, 1976.

[28] H. Horii and S. Nemat-Nasser, "Overall moduli of solids with microcracks: Load-induced anisotropy," *Journal of the Mechanics and Physics of Solids*, vol. 31, no. 2, pp. 155 – 171, 1983.

[29] V. Grechka and M. Kachanov, "Effective elasticity of fractured rocks: A snapshot of the work in progress," *Geophysics*, vol. 71, no. 6, pp. W45–W58, NOV-DEC 2006.

[30] V. S. Deshpande, E. Gamble, B. G. Compton, R. M. McMeeking, A. G. Evans, and F. W. Zok, "A constitutive description of the inelastic response of ceramics," *Journal of the American Ceramic Society*, vol. 94, no. s1, pp. s204–s214, 2011.

[31] M. Sagong and A. Bobet, "Coalescence of multiple flaws in a rock-model material

in uniaxial compression," *International Journal of Rock Mechanics and Mining Sciences*, vol. 39, no. 2, pp. 229 – 241, 2002.

[32] C. Park and A. Bobet, "Crack initiation, propagation and coalescence from frictional flaws in uniaxial compression," *Engineering Fracture Mechanics*, vol. 77, no. 14, pp. 2727 – 2748, 2010.

[33] R. Wong, K. Chau, C. Tang, and P. Lin, "Analysis of crack coalescence in rock-like materials containing three flawspart i: experimental approach," *International Journal of Rock Mechanics and Mining Sciences*, vol. 38, no. 7, pp. 909 – 924, 2001.

[34] A. Bobet and H. H. Einstein, "Numerical modeling of fracture coalescence in a model rock material," *Int. J. of Fract.*, vol. 92, pp. 221–252, 1998.

[35] C. Tang, P. Lin, R. Wong, and K. Chau, "Analysis of crack coalescence in rock-like materials containing three flawspart ii: numerical approach," *International Journal of Rock Mechanics and Mining Sciences*, vol. 38, no. 7, pp. 925 – 939, 2001.

[36] A. L. Tonge and K. Ramesh, "Multi-scale defect interactions in high-rate brittle material failure. part i: Model formulation and application to {ALON}," *Journal of the Mechanics and Physics of Solids*, vol. 86, pp. 117 – 149, 2016.

[37] M. Bakas, V. A. Greenhut, D. E. Niesz, J. Adams, and J. Mccauley, *Relationship*

Between Defects and Dynamic Failure in Silicon Carbide. John Wiley & Sons, Inc., 2008, pp. 351–358.

[38] M. Bakas, V. Greenhut, D. Niesz, G. D. Quinn, J. W. McCauley, A. A. Wereszczak, and J. J. Swab, "Anomalous defects and dynamic failure of armor ceramics," *International Journal of Applied Ceramic Technology*, vol. 1, no. 3, pp. 211–218, 2004.

[39] F. Huq, R. Brannon, and L. Graham-Brady, "An efficient binning scheme with application to statistical crack mechanics," *International Journal for Numerical Methods in Engineering*, vol. 105, no. 1, pp. 33–62, 2016, nme.4959.

[40] S. Nemat-Nasser and H. Horii, "Compression-induced nonplanar crack extension with application to splitting, exfoliation, and rockburst," *Journal of Geophysical Research: Solid Earth*, vol. 87, no. B8, pp. 6805–6821, 1982.

[41] A. E. Green and W. Zerna, *Theoretical Elasticity.* Dover Publications, 1968.

[42] W. T. Chen, "On an ellitic elastic inclusion in an ansiotropic medium," *Quart. J. Mech. Appl. Math.*, vol. 20, pp. 307–313, 1967.

[43] G. Hu, J. Liu, L. Graham-Brady, and K. Ramesh, "A 3d mechanistic model for brittle materials containing evolving flaw distributions under dynamic multiaxial loading," *Journal of the Mechanics and Physics of Solids*, vol. 78, pp. 269 – 297, 2015.

BIBLIOGRAPHY

[44] L. B. Freund, *Dynamic fracture mechanics*. Cambridge university press, 1998.

[45] S. Suresh, T. Nakamura, Y. Yeshurun, K.-H. Yang, and J. Duffy, "Tensile fracture toughness of ceramic materials: Effects of dynamic loading and elevated temperatures," *Journal of the American Ceramic Society*, vol. 73, no. 8, pp. 2457–2466, 1990.

[46] M. F. Ashby and C. G. Sammis, "The damage mechanics of brittle solids in compression," *pure and applied geophysics*, vol. 133, no. 3, pp. 489–521, 1990.

[47] V. S. Deshpande and A. G. Evans, "Inelastic deformation and energy dissipation in ceramics: A mechanism-based constitutive model," *Journal of the Mechanics and Physics of Solids*, vol. 56, no. 10, pp. 3077–3100, 2008.

[48] A. J. R. Harsha S. Bhat and C. G. Sammis, "A micromechanics based constitutive model for brittle failure at high strain rates," *Journal of Applied Mechanics*, vol. 79, no. 3, 2012.

[49] A. L. Tonge, "A unified framework which uses multi-scale microstructural information for modeling dynamic failure in brittle materials," Ph.D. dissertation, Johns Hopkins University, 2014.

[50] G. Hu, K. Ramesh, B. Cao, and J. McCauley, "The compressive failure of aluminum nitride considered as a model advanced ceramic," *Journal of the Mechanics and Physics of Solids*, vol. 59, no. 5, pp. 1076–1093, 2011.

[51] D. J. Macon, "Plastic cap evolution law derived from induced transverse isotropy in dilatational triaxial compression," Master's thesis, University of Utah, 2013.

[52] A. F. Fossum, R. M. Brannon, and O. E. Strack, "Kayenta: Theory and user's guide," Sandia National Laboratories, Albuquerque, NM, Tech. Rep. SAND2009-2282, 2009.

[53] T. J. Holmquist and G. R. Johnson, "computational constitutive model for glass subjected to large strains, high strain rates and high pressures," *Journal of Applied Mechanics*, vol. 78(5), p. 051003, 2011.

[54] B. Martin, M. E. Kabir, and W. Chen, "Undrained high-pressure and high strain-rate response of dry sand under triaxial loading," *International Journal of Impact Engineering*, vol. 54, pp. 51 – 63, 2013.

[55] J. Simo and M. Ortiz, "A unified approach to finite deformation elastoplastic analysis based on the use of hyperelastic constitutive equations," *Computer Methods in Applied Mechanics and Engineering*, vol. 49, no. 2, pp. 221 – 245, 1985.

[56] A. Caiulo and M. Kachanov, "On absence of quantitative correlations between strength and stiffness in microcracking materials," *Int. J. of Fract.*, vol. 164, no. 1, pp. 155–158, 2010.

[57] O. E. Strack, R. B. Leavy, and R. M. Brannon, "Aleatory uncertainty and scale

effects in computational damage models for failure and fragmentation," *Int. J. Numer. Meth. Engng.*, vol. 102, pp. 468–495, 2014.

[58] L. Devroye, *Non-Uniform Random Variate Generation.* Springer-Verlag, New York, 1986.

[59] R. L. Iman and W. J. Conovar, "A distribution-free approach to inducing rank correlation among input variables." *Communications in Statistics: Simulation and Computation*, vol. 11, no. 3, pp. 311–334, 1982.

[60] C. T. Sun and Z.-H. Jin, *Fracture Mechanics.* Elsevier Inc., Waltham, 2011.

[61] R. G. Ghanem and P. D. Spanos, *Stochastic Finite Elements: A Spectral Approach.* Springer-Verlag New York, 1991.

[62] M. Grigoriu, "On the spectral representation method in simulation," *Probabilistic Engineering Mechanics*, vol. 8, no. 2, pp. 75–90, 1993.

[63] M. Shinozuka, "Monte Carlo solution of structural dynamics," *Computers & Structures*, vol. 2, pp. 855–874, 1972.

[64] F. Yamazaki and M. Shinozuka, "Simulation of stochastic fields by statistical preconditioning." *J. Eng. Mech.*, vol. 116, no. 2, pp. 268–287, 1990.

[65] S. Diehl and S. T. Statler, "Adaptive binning of X-ray data with weighted Voronoi tessellations," *Mon. Not. R. Astron. Soc.*, vol. 368, pp. 497–510, 2006.

[66] M. Cappellari and Y. Copin, "Adaptive spatial binning of integral-field spectroscopic data using Voronoi tessellations." *Mon. Not. R. Astron. Soc.*, vol. 342, pp. 345–354, 2003.

[67] M. Roederer, W. Moore, A. Triester, R. R. Hardyand, and L. A. Herzenberg, "Probability binning comparison: A metric for quatitaing multivariate distribution differences," *Cytometry*, vol. 45, pp. 47–55, 2001.

[68] M. Roederer, A. Treister, W. Moore, and L. A. Herzenberg, "Probability binning comparison: A metric for quantitating univariate distribution differences," *Cytometry*, vol. 45, no. 1, pp. 37–46, 2001.

[69] J. C. Helton and F. J. Davis, "Latin hypercube sampling and the propagation of uncertainty in analyses of complex systems," *Reliability Engineering and System Safety*, vol. 81, pp. 23–69, 2003.

[70] A. Florian, "An efficient sampling scheme: Updated Latin hypercube sampling," *Probilistic Engineering Mechanics*, vol. 7, pp. 123–130, 1992.

[71] D. E. Huntington and C. S. Lyrintzis, "Improvements to and limitations of Latin hypercube sampling," *Probabilistic Engineering Mechanics*, vol. 13, no. 4, pp. 245–253, 1998.

[72] M. Danny, "Introduction to importance sampling in rare-event simulations." *Eur. J. Phys.*, vol. 22, pp. 403–311, 2001.

[73] M. Evans and T. Swartz, "Baysian integration using multivariate student importance sampling." *Computing Science and Statistics*, vol. 27, pp. 456–461, 1996.

[74] M. S. Oh and J. O. Berger, "Integration of multimodal functions by Monte Carlo importance sampling." *Journal of the American Statistical Association*, vol. 88, no. 422, pp. 132–141, 1993.

[75] J.-F. Richard and W. Zhang, "Efficient high-dimensional importance sampling," *Journal of Econometrics*, vol. 141, no. 2, pp. 1385–1411, 2007.

[76] P. Zhang, "Nonparametric importance sampling." *Journal of the American Statistical Association*, vol. 91, no. 435, pp. 1245–1253, 1996.

[77] S. K. Au and J. L. Beck, "First excursion probabilities for linear systems by very efficient importance sampling," *Probabilistic Engineering Mechanics*, vol. 16, pp. 193–207, 2001.

[78] F. Grooteman, "An adaptive directional importance sampling method for structural reliability," *Probabilistic Engineering Mechanics*, vol. 26, pp. 134–141, 2011.

[79] D. Sulsky, "A particle method for history-dependent materials," *Comput. Methods Appl. Mech. Engrg.*, vol. 118, no. 1-2, p. 179, 1994.

[80] A. Sadeghirad, R. Brannon, and J. Guilkey, "Second-order convected particle domain interpolation (CPDI2) with enrichment for weak discontinuities at material interfaces," *Int. J. Numer. Meth. Engng.*, vol. 95, pp. 928–952, 2013.

[81] I. Sevostianov and M. Kachanov, "Local minima and gradients of stiffness and conductivity as indicators of strength reduction of brittle materials," *Int. J. of Fract.*, vol. 164, pp. 147–154, 2010.

[82] R. Snieder, *A Guided Tour of Mathematical Methods for the Physical Sciences*, 2nd ed. Cambridge University Press, Newyork, 2004.

[83] J.-D. Boissonnat, K.-L. Shi, J. Tournois, and M. Yvinec, "Anisotropic Delaunay meshes of surfaces," *ACM Trans. Graph.*, vol. 34, no. 2, pp. 14:1–14:11, Mar. 2015.

[84] D. P. Dandekar, "Shock response of boron carbide," Army Research Laboratory, Aberdeen Proving Ground, Tech. Rep., 2001.

[85] B. Paliwal and K. Ramesh, "Effect of crack growth dynamics on the rate-sensitive behavior of hot-pressed boron carbide," *Scripta materialia*, vol. 57, no. 6, pp. 481–484, 2007.

[86] F. Thvenot, "Boron carbidea comprehensive review," *Journal of the European Ceramic Society*, vol. 6, no. 4, pp. 205 – 225, 1990.

[87] S. Chocron, C. E. Anderson, K. A. Dannemann, A. E. Nicholls, and N. L. King, "Intact and predamaged boron carbide strength under moderate confinement pressures," *Journal of the American Ceramic Society*, vol. 95, no. 1, pp. 350–357, 2012.

[88] M. Kachanov, "Effective elastic properties of cracked solids: Critical review of some basic concepts," *Applied Mechanics Reviews*, vol. 45, p. 304, 1992.

[89] J. de St. Germain, J. McCorquodale, S. Parker, and C. Johnson, "Uintah: A massively parallel problem solving environment," in *Ninth IEEE International Symposium on High Performance and Distributed Computing*. IEEE, Piscataway, NJ, Nov 2000, pp. 33–41.

[90] A. L. Tonge and K. Ramesh, "Multi-scale defect interactions in high-rate failure of brittle materials, part ii: Application to design of protection materials," *Journal of the Mechanics and Physics of Solids*, vol. 86, pp. 237 – 258, 2016.

[91] S. M. Ross, *A First Course in Probability*, 5th ed. Prentice Hall, Upper Saddle River, 1998.

[92] S. Ross, *Introduction to Probability Models*. Academic Press, 2014.

[93] A. L. Tonge, J. Kimberley, and K. T. Ramesh, "A consistent scaling framework for simulating high rate brittle failure problems," *Procedia Engineering*, vol. 58, pp. 692–701, 2013.

BIBLIOGRAPHY

Farah Huq was born on November 24, 1985 in Dhaka, Bangladesh. She obtained her Bachelor's of Science in Civil Engineering from Khulna University of Engineering and Technology in 2007. After grduating she worked as structural engineering at Design, Planning and Management Consultants Ltd. in Dhaka, Bangladesh. She finished her masters from University of Memphis in 2011. She worked in developing optimization algorithm to aid in structural design as part of her Masters research. Farah joined department of Civil Engineering in Fall 2011 as a Ph.D. student. She received Carl E. Heath fellowship in 2011 to pursue her Ph.D. education. She worked with Hopkins Extreme Materials Institute from 2013 under the ceramic modeling task. She will continue her research career at Intel.